Multistability due to Delayed Feedback and Synchronization of Quasiperiodic Oscillations Studied With Semiconductor Lasers

D I S S E R T A T I O N

zur Erlangung des akademischen Grades

Dr. rer. nat.
im Fach Physik

eingereicht an der
Mathematisch-Naturwissenschaftlichen Fakultät I
Humboldt-Universität zu Berlin

von
Dipl.-Phys. André Loose

Präsident der Humboldt-Universität zu Berlin:
Prof. Dr. Jan-Hendrik Olbertz

Dekan der Mathematisch-Naturwissenschaftlichen Fakultät I:
Prof. Dr. Andreas Herrmann

Gutachter:
1. Prof. Dr. Fritz Henneberger
2. Prof. Dr. Ingo Fischer
3. Prof. Dr. Jürgen Kurths

eingereicht am: 10.03.2011
Tag der mündlichen Prüfung: 16.09.2011

To Susanne Loose.

Abstract

In this work two nonlinear phenomena are investigated, multistability due to delayed feedback and synchronization of quasiperiodic oscillations. The experimental devices are semiconductor lasers with ultra-short optical feedback, which is integrated on the same chip as the laser. By adding sections with different functionality, which can be individually biased with a direct current, all feedback parameters can be adjusted. A wide variety of dynamical scenarios can be prepared with such a multisection laser. When the devices are operated near bifurcations, the dynamics can be reduced to the same mathematical models valid for the description of many seemingly distinct physical systems. They are therefore an excellent tool to investigate nonlinear dynamics, and findings may prove to be very generally applicable. On the other hand, the specifics of the realization of a physical mechanism in a laser system are equally interesting. E.g., the ultrafast intrinsic timescales of the laser can be employed in telecommunication applications.

Delayed feedback causes the folding of lasing modes, leading to hysteresis effects and even the coexistence of several laser states for the same parameters. Here, I present an experimental and theoretical study of multistability closely above the lasing threshold. A regime of tristability of continuous-wave (cw) states is found for multiple ranges of applied currents. Very close to threshold, a lasing state may be replaced by the stable "off"-state. The separation between the tristable wavelengths agrees with the channel spacing of dense wavelength multiplexing of optical communication, making the device interesting for e.g. switching applications. Complementary theoretical investigations in the framework of the paradigmatic Lang-Kobayashi model provide a consistent understanding of the experimental findings. Additionally, they yield an analytic formula expressing the maximum number of coexisting stable cw states by the linewidth-enhancement factor α. Tristability belongs to the α range from 5 to 8, in good agreement with experiment.

Besides modifying the stationary behavior of a semiconductor laser, delayed feedback can cause instabilities of the laser output. Depending on strength and phase of the feedback, two types of self-sustaining pulsations of the emitted light intensity are found in our devices. Synchronization processes of such pulsations are studied in a system of two coupled multisection lasers. Periodic self-pulsations of laser 1 are injected into laser 2, which is operating in a regime with two-frequency quasiperiodic self-pulsations. The experimental system demonstrates the new type of transitions to synchrony between three frequencies which has been recently revealed using generic coupled phase and van der Pol oscillator models. This is despite the significant increase of system complexity and therefore a strong indication for universality of these phenomena. In particular, resonances of quasiperiodic oscillations at integer winding numbers three and five are shown to break up before locking to the injected periodic signal. Moreover, carefully determining the coherence of the noisy oscillations, so far unexplored processes of coherence transfer to nonsynchronized oscillations are revealed.

Keywords: nonlinear dynamics, multistability, delayed feedback, synchronization, quasiperiodic

Zusammenfassung

In dieser Arbeit werden zwei nichtlineare Phänomene untersucht, Multistabilität durch verzögerte Rückkopplung und Synchronisation von quasiperiodischen Oszillationen. Dies geschieht mit Hilfe von Halbleiterlasern und auf dem selben Chip wie der Laser integrierter ultrakurzer optischer Rückkopplung. Durch das Hinzufügen von Sektionen mit unterschiedlicher Funktionalität, welche individuell mit Gleichströmen angesteuert werden können, sind alle Rückkoppelparamter beeinflussbar. Eine Vielzahl von Dynamiken ist mit einem solchen Multisektionslaser einstellbar. Wenn die Bauteile in der Nähe von Bifurkationen betrieben werden, kann die Dynamik oft auf die gleichen mathematischen Modelle wie für scheinbar völlig andersartige physikalische Systeme reduziert werden. Sie sind daher ein sehr gutes Werkzeug zur Untersuchung nichtlinearer Dynamik, hierbei erzielte Ergebnisse sind potentiell sehr universell anwendbar. Andererseits sind die spezifischen Eigenschaften der Realisierung in einem Laser für sich selbst genommen ebenfalls von Interesse. In unserem Falle können die ultraschnellen internen Zeitskalen der Laser beispielsweise für Zwecke der Nachrichtenübertragung genutzt werden.

Verzögerte Rückkopplung ist unter anderem die Ursache für das Phänomen der Faltung von Lasermoden, und damit für das Auftreten von mehreren möglichen Laserzuständen für die selben Parameter. In dieser Arbeit stelle ich eine experimentelle und theoretische Studie solcher Multistabilität nahe der Laserschwelle vor. Ein tristabiles Regime von Dauerstrichzuständen kann im Experiment für mehrere breite Parameterbereiche der Rückkopplung beobachtet werden. Sehr nahe der Laserschwelle wird einer der Laserzustände durch den stabilen “aus”-Zustand ersetzt. Der Abstand zwischen den Emissionswellenlängen der koexistierenden Zustände entspricht der Übertragungskanalseparation des Wellenlängen-Multiplex-Verfahrens im C-Band der optischen Kommunikation. Dies macht die verwendeten Laserstrukturen z.B. interessant für Routing-Anwendungen. Ergänzende theoretische Betrachtungen im Rahmen des paradigmatischen Lang-Kobayashi Models verzögerter Rückkopplung ermöglichen eine in sich konsistente Interpretation der experimentellen Ergebnisse. Zusätzlich führen sie zu einer analytischen Formel, welche die maximale Anzahl der koexistierenden Dauerstrichzustände als Funktion des Linienverbreiterungsfaktors α ausdrückt. Tristabilität gehört zum Parameterbereich $\alpha = 5 - 8$, in guter Übereinstimmung mit dem Experiment.

Neben der Beeinflussung des stationären Verhaltens eines Halbleiterlasers kann verzögerte Rückkopplung Instabilitäten in der Laseremission hervorrufen. Abhängig von Rückkoppelstärke und -phase werden zwei verschiedene Intensitätspulsationen des emittierten Lichtes beobachtet. Synchronisationsprozesse solcher Pulsationen wurden von mir in einem System von zwei verschiedenen gekoppelten Multisektionslasern untersucht. Periodische Selbstpulsationen von Laser 1 werden hierfür in Laser 2 injiziert, welcher sich in einem Regime quasiperiodischer Intentensitätspulsationen mit zwei fundamentalen Frequenzen befindet. Das Experiment zeigt eine neue Art von Übergang zu synchronem Verhalten, welche kürzlich mit Hilfe von gekoppelten generischen Phasen- und van der Pol Oszillatormodellen aufgedeckt wurde. Auf Grund des weit komplexeren experimentellen Systems ist dies ein Hinweis auf mögliche Universalität der beobachteten Phänomene. Im Speziellen brechen Resonanzen quasiperiodischer Oszillationen mit den ganzzahligen Windungsnummern 3 und 5 auf, bevor sie auf das externe periodische Signal synchronisieren. Desweiteren

konnten bislang unerforschte Prozesse des Kohärenzübertrags auch zu nichtsynchronisierten Oszillationen beobachtet werden.

Schlagwörter: nichtlineare Dynamik, Multistabilität, verzögerte Rückkopplung, Synchronisation, quasiperiodisch

Contents

1 Introduction

Very few phenomena have a linear relationship between cause and effect. Although some important examples can be approximated well to behave in such a way, fundamentally nonlinear processes govern nature, as for example the neural system of animals and therefore human vision and hearing [1]. Rhythms in biological systems may mutually adjust by a weak coupling [2], like the flashing of fireflies or breathing to heartbeat [3]. The state of a physical system may depend not only on its current parameters, but also on what happened in the past - magnetism with its hysteresis effects has been known for thousands of years. Furthermore, in magnetic materials the formation and movement of localized structures, magnetic domain walls, can be observed. Non-decaying waves, called solitons in the mathematical literature, can be seen in the wake of ships traveling trough a channel. Sometimes nonlinear phenomena are very counterintuitive. For example, additional white noise of just the right magnitude may lead to a significant *improvement* of the quality of oscillations [4]. Sometimes nonlinearities can be dangerous, like clear air turbulence in aviation or the formation of freak waves in seafaring, see Fig. 1.1. There are many other phenomena for which the principle of superposition, i.e. linear addition of magnitudes and separability of causing effects, is not applicable.

The investigation of nonlinear devices was motivated at least in part by the needs of radar technology [7, 8] in the beginning and middle of the last century. It eventually resulted in the development of transistors, which are used in modern integrated circuits. In optics, e.g. the use of nonlinear crystals for the up- and downconversion of light is common. Experiments investigating complex dynamics aid e.g. in the understanding of corrosion in steel reinforced concrete, which is used as material for most of the structures built today. To introduce the challenges nonlinear systems pose and give examples for their relevance in e.g. technology and medicine, I will expand on a few selected concepts in the next paragraphs. Subsequently, I summarize mathematical concepts which have been developed to handle computational complications of nonlinear equations. In this context, we will see why the results of experiments with semiconductor lasers may lead to findings which are not only specific to laser devices, but applicable to a large class of dynamical systems. Finally, I will give an outline for this thesis.

1.1 Nonlinearity and Collective Behavior

Thresholding effects. When an electrical impulse is applied to an isolated nerve cell and does not exceed a certain strength, nothing happens. If the magnitude of this perturbation however exceeds a threshold value, the following reaction of the cell is drastic, manifests itself after a characteristic timespan, and is combined with a refractory time in which no further stimulation is possible. This phenomenon, excitability, is not special

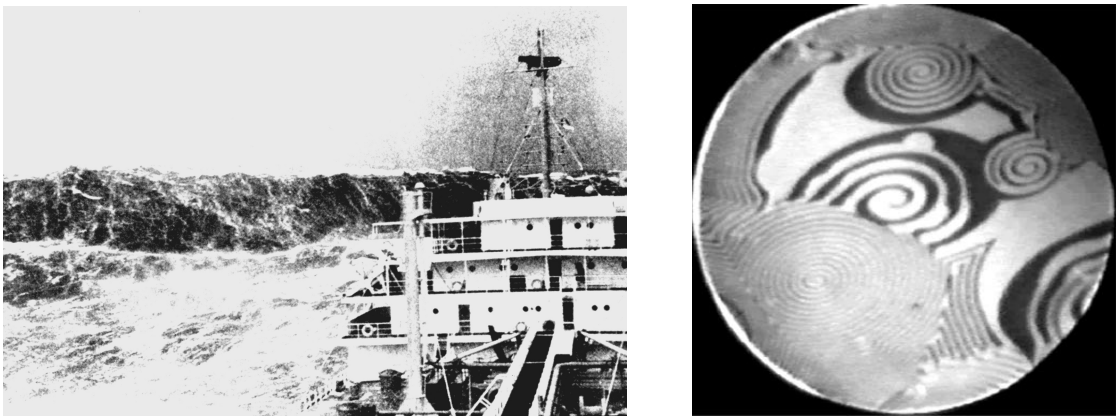

Figure 1.1: (left panel) Rogue wave in the Bay of Biscay, France, as seen from a merchant ship. Image taken from [5]. (right panel) Photoemission Electron Microscope (PEEM) image of the catalytic CO oxidation on a Pt(110) surface, showing the formation of spiral wave reaction fronts. Bright areas, CO-covered. Dark areas, O-covered. Observed diameter 0.5 mm. Image taken from [6].

to nerve cells, while it is of fundamental importance for their function in the brain. It has been shown to also exist e.g. in carefully prepared semiconductor lasers [9, 10, 11] when an optical pulse is injected. The very existence of a threshold, which separates qualitatively different reactions to a perturbation, is important. It has substantial influence e.g. on how dangerous substances are for the human body. In everyday life, we are confronted with an overwhelming variety of both natural and artificial chemical compounds, whose effects on the human body are essentially unknown. Yet most are clearly not problematic, as long as a certain dose is not exceeded within some time interval. They are not stored in the body and eventual damage done by them can be fully repaired. In contrast, even minimal exposure to substances like lead should be avoided, as they accumulate over time and eventually reach critical amounts. When evaluating potential risks of chemicals and medication for humans, determining whether such a threshold exists is crucial.

Sensitivity towards small perturbations. In the middle of last century, computers became available for the numerical study of nonlinear equations which often can neither be solved exactly, nor with perturbative methods. It became apparent that even very simple systems like the "logistic" map $x_{n+1} = rx_n(1 - x_n)$, setting e.g. $r \approx 3.5$, exhibit complex dynamics. Numerical studies of atmospheric models demonstrated clearly that sensitivity to initial conditions may have drastic effects, leading to radically different forecasts for essentially equal starting conditions [12]. It follows, that in some cases one is unable to predict the development of a dynamical system on long timescales in principle. This holds even when the full equations are known and deterministic. It is a defining property of aperiodic and bounded, "chaotic", dynamics. A striking aspect of such behavior is that deterministic physical systems exist, for which reproducible experiments cannot be realized in the lab in principle. Such systems have "riddled

basins of attraction". Arbitrarily small measurement errors result in slightly different initial conditions, eventually leading to a totally distinct evolution in time [13]. Despite these difficulties, the computer as a tool considerably enhanced the understanding of nonlinear systems. Numerical studies show that complex behavior often emerges in a qualitatively similar manner. Sometimes, even quantitative predictions and subsequent strict proofs of universality are possible [14].

Collective behavior. Even when a single entity can be modeled with excellent accuracy when alone, fundamentally non-predictable complex behavior may arise when a sufficient number of such elements interact. This means on the other hand that the description of some complex systems may not be reducible to a few fundamental laws [15]. The transition to collective behavior is an example of a phase transition which can be described by an order parameter. In the case of superconductivity this is the macroscopic pair function, or it is the non-vanishing mean field when oscillating units exhibit phase synchronization [16, 17]. Cooperative and even non-cooperative interaction can lead to the emergence of collective phenomena. E.g., ultrafast intensity oscillations develop when a direct current is applied to a laser diode [18], and fish demonstrate complex patterns of collective motion in swarms [19]. The growth of rust on surfaces can be understood as cooperative critical phenomenon [20]. Nonlinear systems with several spatial coordinates often show the formation of patterns: Chemical reactions out of equilibrium may form spiral wave reaction fronts on the surface of catalytic converters, see Fig. 1.1, and can be controlled by appropriate means [21]. The Belousov-Zhabotinsky (BZ) reaction [22] is a prominent example for complex dynamics of chemical systems far from equilibrium. It exhibits up to several thousand oscillatory cycles when running in a closed system; and enables one to experimentally investigate nonlinear phenomena. Nonlinear mechanisms have also been proposed to govern the pattern formation on the coat of animals [23].

From the examples given is clear that a nonlinear model system might be difficult to solve, and even if this can be done, the solutions obtained might be hard to interpret. Even for deterministic systems the long term behavior may be fundamentally non-predictable, because they are sensitive to small changes in the initial conditions. The question then is whether one can extract any useful information at all, or not.

1.2 A Geometric View of Dynamics

The answer is in the affirmative - even if no closed solution exists, usually a lot can be said about the *qualitative* behavior of the dynamical system. Often not only the existence of solutions, but even how their type, number and stability changes as parameters are varied can be established. To this purpose, one plots the dynamical variables in an abstract *phase space*, which is the collection of all possible states of a dynamical system. The state of the system at any time instant corresponds to exactly one point in phase space. As time progresses, trajectories often fall into the following four categories: *Fixed points* correspond to stationary solutions, *limit cycles* forming a closed loop to periodic solutions with a characteristic fundamental frequency, *quasiperiodic orbits* on a torus to periodic solutions with at least two fundamental frequencies, and finally bounded non-

periodic (*chaotic*) solutions. The idea now is to look at the geometry of trajectories in phase space instead of the exact solutions, e.g., by representing the differential equation as a vector field. This way, we may be able to determine graphically that, e.g., some fixed point exists, even if we don't know the exact location. We might even be able to infer the stability of this fixed point. Without actually solving the underlying equations, the qualitative behavior of the dynamical system can be characterized. It is already very valuable to know that a dynamical system, however complex the transient behavior may be, eventually settles to an unique equilibrium.

Already in the 19th century, Poincaré showed in his studies of the stability of the three-body system how one may obtain such qualitative results. He introduced a technique to visualize the flow in phase space of more than two dimensions, turning the original continuous dynamical system into a discrete one by choosing an intersecting plane in phase space. The dimension is reduced by one, but if the reduction is done correctly the map defined on this "Poincaré-section" still has the dynamical features of the full system and can be analyzed. *Center manifold reduction* is another mathematical tool to reduce the dimensionality of a dynamical system. The basic idea behind it is simple. Many physical systems which are described by complex nonlinear models actually spend a lot of time in or near some equilibrium state, e.g., on a limit cycle. Near equilibria, some dynamical variables may be *enslaved*, they just instantly follow the dynamics determined by some other variable. Because of this property the dynamical equations can be successfully simplified near the equilibrium.

The starting point of the analysis of nonlinear equation systems therefore is the search for equilibria and the determination of their stability. Trajectories representing such an equilibrium can be *asymptotically stable*, *marginally stable* or *unstable*. Asymptotical stability implies that as long one starts close enough and waits for a sufficiently long time, the trajectory in phase space eventually converges towards this equilibrium and follows it from there on. Marginal stability is a weaker condition, just requiring that one remains "close enough" to the equilibrium forever, without actually having to reach it. An equilibrium is defined as unstable if it is not stable. Given a generic dynamical system $\dot{x} = f(x, p)$ for the n-dimensional state vector x, depending on m parameters p, we first look whether some equilibrium state $\dot{\bar{x}} = 0$ can be found. If this is the case, we have to determine the dynamics near $\bar{x}$, i.e. for $x = \bar{x} + \epsilon$ with the small deviation ϵ.

We first approximate the nonlinear system for small displacements ϵ from the equilibrium $\bar{x}$ by the Taylor expansion

$$f(\bar{x} + \epsilon) = e^{\epsilon \cdot \nabla} f(\bar{x}) \approx f(\bar{x}) + \epsilon \cdot \nabla f(\bar{x}),$$

and analyze the stability of this linearized system. The roots of the characteristic polynomial $\det(\nabla f(\bar{x}) - \lambda I) = 0$ are the eigenvalues λ_i. $\nabla f(\bar{x})$ is the real $n \times n$ Jacobian matrix with the elements $\nabla f(\bar{x})_{ij} = \frac{\partial x_i}{\partial x_j}|_{x=\bar{x}}$, I the $n \times n$ unit matrix $I_{ij} = \delta_{ij}$. The eigenvalue spectrum $\{\lambda_i\}$ for $i = 1 \ldots n$ determines the asymptotic stability *of the linearized system*.

If none of the λ_i have a vanishing real part, the system is called hyperbolic. In this case, the determination of its stability straightforward. Each $\lambda_i > 0$ belongs to an unstable

direction, together forming the unstable eigenspace E^u. Each $\lambda_i < 0$ signifies a stable direction, which define the stable eigenspace E^s. A change in stability is therefore always connected with the real part of some eigenvalue λ_i changing from negative to positive, or conversely. We will use a fixed point as equilibrium in the following example. If all $\lambda_i < 0$, all trajectories starting nearby will exponentially decay towards it and the stable fixed point is called a sink. If now at least one λ_i has a positive real part, it is a saddle point. Some directions are still attracting, but others repelling. In the case that all λ_i have positive real parts, the fixed point is unstable and called a source or repeller. All trajectories starting nearby move away exponentially fast.

Whenever the spectrum of the eigenvalues includes at least one λ_i with zero real part, the determination of stability is nontrivial. The center eigenspace E^c is spanned by the unit vectors belonging to these $\lambda_i = 0$. E^c determines the stability of the linearized system near the fixed point: All trajectories starting in E^s converge exponentially towards the fixed point and therefore end up on E^c, while all trajectories in E^u leave the neighborhood of the fixed point exponentially fast. Variables that are determined by the fast motion towards $\bar{x}$ in E^s are the formerly mentioned enslaved variables. They almost instantly follow the dynamics of all other system variables.

Even when the stability of the linearized system can be determined, it may not apply to the original nonlinear system. For a hyperbolic system, topological equivalence to the linearized case near a fixed point has been established by the Grobman-Hartman theorem [24]. In this case, the linearization above correctly predicts the stability of the nonlinear system. If $\lambda_i = 0$ exist, the stability of linearized system and nonlinear system may differ. The nonlinear system has invariant manifolds analogous to the linear stable, unstable and center eigenspaces of the linearization. Similarly, the center manifold determines the local stability. It is tangent to the center eigenspace of the linearized system at the origin, but in general neither a linear space, nor unique. An approach different from linearization must be used to determine the stability of the system near an equilibrium; the center manifold of the nonlinear system is approximated by a power series. As can be shown, the stability of this approximation is equivalent to the stability of the full nonlinear system.

After we characterized a nonlinear dynamical system by looking for its equilibria and their stability, we may be able to apply bifurcation theory to a suitable approximation of the full nonlinear system.

1.3 Universality near Bifurcations

The appearance and disappearance of different types of trajectories by a change of their stability is called a bifurcation. A change of stability and a bifurcation are therefore two aspects of the same phenomenon. Bifurcations may be generic, in the sense that many phenomena can be described by the same reduced mathematical models in their vicinity. This allows the study of nonlinear effects with experimental systems that are easily controllable and well understood - for example semiconductor lasers. On the other hand, each specific realization of such a generic mechanism may be very different. As e.g. many

physical mechanisms are responsible for oscillatory behaviour, the intrinsic timescales and other parameters may be vastly different, to the point that underlying commonalities are hardly recognizable. For the semiconductor lasers used in our experiments, many bifurcation types are known to occur. They can be accessed in a very controlled way by tuning the direct current applied to e.g. the laser section [25] and the physical mechanisms related to them are well understood. This already allowed for the targeted investigation of a wide variety of phenomena, like the influence of noise on oscillations [4], excitability [9, 10, 11] and synchronization with a finite propagation delay between the oscillators [26].

Two examples for bifurcations which can be studied in our devices, and will be important for the following chapters, are saddle-node and Hopf bifurcations. The generic scenario for both is explained in Fig. 1.2 (a-c). In a saddle-node bifurcation, an additional pair of a stable and an unstable equilibrium is created or annihilated when changing the control parameter[1]. This bifurcation will be discussed e.g. in the context of the folding of stationary laser modes in Fig. 3.5 on page 31. At a supercritical Hopf bifurcation, a stable equilibrium is replaced by a stable limit cycle and an unstable equilibrium. In our lasers, the amplitude of the oscillation connected to the stable limit cycle grows or vanishes smoothly when changing the control parameter, see e.g. Fig. 2.8 on page 22. In contrast, at a subcritical Hopf bifurcation a stable steady state and an unstable limit cycle are replaced by an unstable equilibrium. In our devices, the laser jumps from the vanishing stable steady state with strongly damped and low-amplitude relaxation oscillations into a large amplitude self-pulsation, connected to a different stable limit cycle in phase space. The amplitude variation observed in experiments is discontinuous when changing the control parameter, see e.g. Fig. 2.7 on page 20. The *codimension* of a bifurcation denotes the number of parameters p that have to be varied to observe the bifurcation, e.g., both the saddle-node and Hopf bifurcation have codimension one. All bifurcations mentioned so far are local. There are also global bifurcations, which cannot be found by local stability analysis. In their case, the topology change in phase space cannot be confined to a small neighborhood. An example is the homoclinic bifurcation, where a limit cycle collides with a saddle point, see Fig. 1.2 (d).

Bifurcation theory allows us to characterize the changes of the dynamics of a system near to the equilibrium which we can expect when changing parameters. Often, this step is complemented by the use of numerical continuation methods. An illustrative example not related to lasers, discussing the generation of action spikes by neurons due to different types of bifurcations, can be found in Ref. [28].

1.4 Outline of This Thesis

In the preceding pages, I laid out some fundamental properties of nonlinear systems and gave an outline how they are investigated. In the framework of this thesis, I explored fundamentally nonlinear effects with the help of integrated laser devices, which were

[1] Without non-invasive control schemes as the one presented in Ref. [27], unstable trajectories are not observed in experiment.

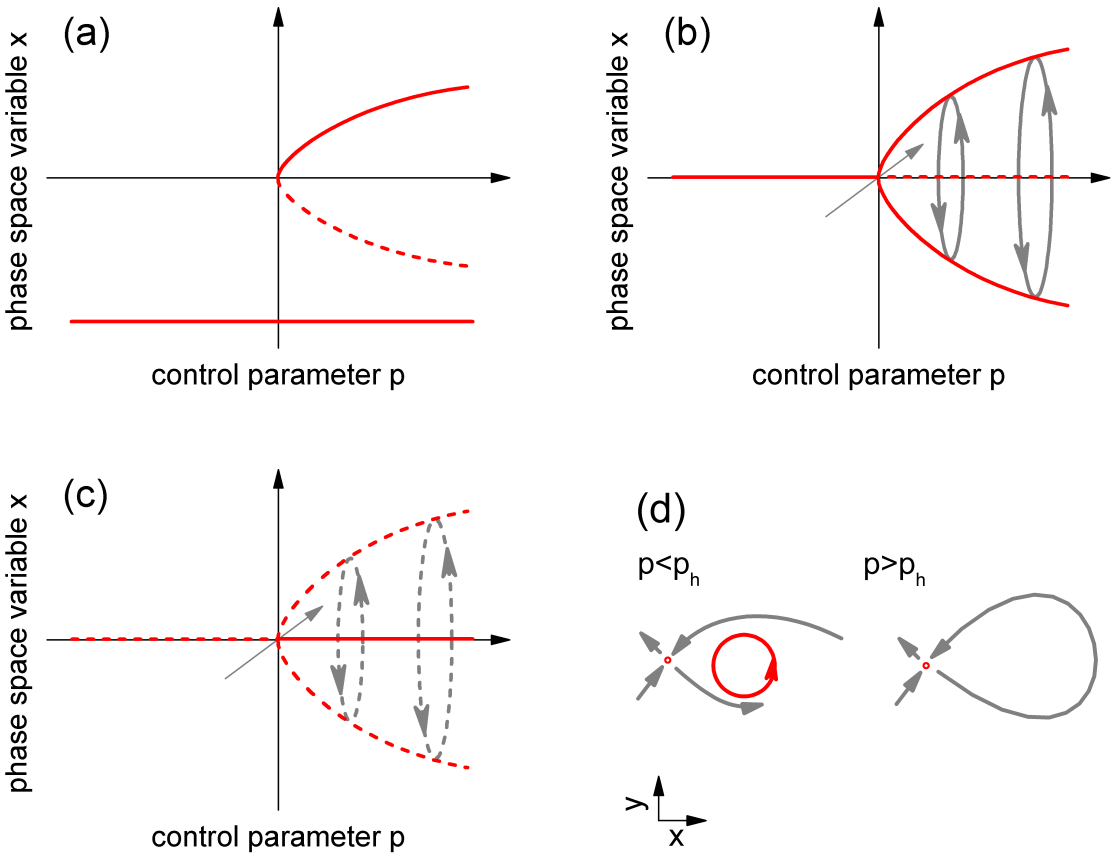

Figure 1.2: Examples for local and global bifurcations. Full lines, stable trajectory. Dashed lines, unstable trajectory. (a-c), local bifurcations. (a), saddle-node (fold) bifurcation. A stable and an unstable steady state branch meet and annihilate each other, the system jumps to another stable state. (b), supercritical Hopf bifurcation. A stable equilibrium is replaced by a stable limit cycle and an unstable equilibrium. (c), subcritical Hopf bifurcation. An unstable steady state is stabilized and an unstable limit cycle emerges. (d), nonlocal homoclinic bifurcation. A limit cycle grows until it collides with a saddle point. After the bifurcation, for parameter values $p > p_h$, only a homoclinic orbit connecting the saddle point with itself remains.

originally developed for applications in communication networks [29, 30, 31]. These devices can be modeled well [32, 33] and allow for the targeted and reproducible realization of complex dynamical scenarios [25]. Their physical properties and dynamics relevant for our experiments will be detailed in the next chapter. In the experiments the devices were used to investigate two nonlinear effects. In the third chapter, I will describe how multistability occurs due to delayed optical feedback when the laser is biased near threshold. The fourth chapter deals with the synchronization of quasiperiodic oscillations to a periodic forcing, using a master-slave configuration. In the last chapter, I will give a short summary and outlook.

2 Multisection Semiconductor Lasers and Delayed Optical Feedback

Semiconductor lasers are excellent devices to investigate nonlinear dynamics. In the following, I summarize the physical principles and properties they are governed by, and introduce the coupled rate equations commonly used to model their dynamics. Later, these rate equations will be extended and employed to theoretically describe multistability near the lasing threshold. The mechanism behind the multistable behavior is delayed optical feedback. Here, I give a short overview of the effects such feedback may have. Furthermore I will introduce the experimental devices used, multisection lasers. Two types of oscillatory instabilities of the light intensity emitted by these lasers, relaxation oscillations and mode-beating oscillations, will be discussed. In the context of multistability, mode-beating pulsations impose a limit on the maximum number of coexisting states. In the fourth chapter, I will investigate complex synchronization processes involving both intensity pulsation types.

2.1 A Strongly Nonlinear System - the Semiconductor Laser

2.1.1 Basic Principles and Applications

After first experimental realizations in 1962 [36, 37, 38, 39], semiconductor laser technology was mature enough to be routinely used in consumer products from the 1980s on. Today, even some computer mice use these small devices. They are widely employed for measurement, sensing, manufacturing purposes in industry and research, and medical surgery. Major advantages of this laser type are that it can be manufactured by standard semiconductor growth and processing techniques, and that it is driven by electrical currents. The requirements for lasing wavelength, output power and other characteristics lead to different materials and structures used. Prominent material examples in the infrared are GaAlAs for 700-900 nm and InGaAsP for 1000-1600 nm emission wavelengths. Despite the differences, only a few key mechanisms and properties of the semiconductor material are sufficient to capture the essential dynamics of these lasers.

As for any laser, gain and feedback are needed for the stimulated emission of light[1]. The feedback can be generated by the mirrors in a Fabry-Perot cavity [41, 42, 43], spread out like in the case of distributed feedback (DFB) lasers [44, 45] or even stem from randomly distributed scatterers[2] [47, 48]. An optical cavity is either formed by

[1] Not necessarily inversion, see e.g. Ref. [40].

[2] Water vapor masers are known to exist within the nuclei of some galaxies [46]. They are very likely the largest examples for coherent emission of radiation in the universe.

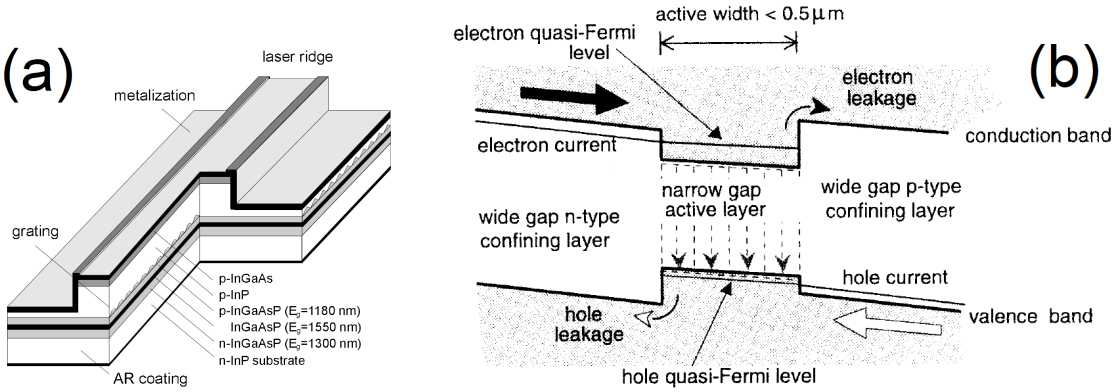

Figure 2.1: (a) The schematic of a heterostructure semiconductor laser diode, as used in the experiments. The facets of the device are anti-reflection (AR) coated, a Bragg grating in the upper p-InGaAsP waveguide layer provides the (distributed) feedback. The active layer has a band gap corresponding to an emission wavelength of around 1540 nm. Figure taken from Ref. [34]. (b) Simplified scheme of the band structure of such a heterostructure junction laser. The confining layers provide waveguiding for the modes in the active layer. Figure taken from Ref. [35].

cleaved facets of semiconductor material, or by a periodic modulation of the refractive index or gain profile. The high gain provided by the material results in very short cavity lengths below one millimeter. The amplification of the light is due to stimulated recombination of electron-hole pairs. To this purpose, a direct current is injected into a p-n heterojunction. In Fig. 2.1 (b) a schematic of the band structure across the vertical direction of the device sketched in Fig. 2.1 (a) is given. Within the active layer, the electrons in the conduction band recombine with the holes in the valence band and emit photons. The band gap of the semiconductor gain material determines the lasing wavelength. In our case a InGaAsP heterostructure structure with a DFB grating is used, see Fig. 2.1. The cleaved facets are anti-reflection coated, the center wavelength is around 1550 nm. This intentionally coincides with a wavelength region used in optical communication, where light experiences a minimum in losses when guided through silica glass fibers [49].

Both spontaneous and stimulated recombination lead to the emission of light [50]. Below the threshold current of the laser, photons with random directions and random optical phases are generated. This is the principle of light emitting diodes. When surpassing the laser threshold stimulated emission sets in, see Fig. 2.2. It dominates the emission characteristics above threshold, resulting in a high coherence of the emitted light. The carrier density in the active zone remains at the threshold value when the laser emits at a single wavelength with constant intensity (continuous wave, cw)[3]. Addi-

[3]The timescale of carrier density variations in the non-constant case is usually much slower than the round trip time of the light in the cavity, so that optical modes can adapt quasi-instantly to a change

tional injected charge carriers are used to generate additional photons with a very high efficiency. This results in a linear increase of the emitted light intensity with a linear increase of the applied direct current. The photons in the emitted coherent beam are statistically independent, whereas the photons from an extremely monochromatic classical light source show a temporal correlation [51][4]. The statistical relation between the times when individual photons are emitted changes from Bose-Einstein type to Poissonian when lasing starts.

2.1.2 A Simplified Description by Rate Equations

To illustrate the main principles governing the dynamics of a semiconductor laser, I will use a strongly simplified description by rate equations. Although the laser devices used in experiments and technological applications are very complex, they can be understood to a very good degree with this idealized model.

Because of the large intensities involved, the optical field is treated classically. Polarization dynamics happen on the femtosecond scale in semiconductor lasers, therefore the polarization can be adiabatically eliminated if we consider dynamics slower than a picosecond. Two coupled first-order differential equations describe the dynamics of the carrier density $\tilde{N}(t)$ and the optical field amplitude $\tilde{E}(t)$:

$$\frac{d}{dt}\tilde{E}(t) = \left\{\frac{1}{2}\Big(G(\tilde{N}(t)) - \frac{1}{\tau_p}\Big) - i\big(\omega_0 + \Delta\omega(\tilde{N}(t))\big)\right\}\tilde{E}(t) \tag{2.1a}$$

$$\frac{d}{dt}\tilde{N}(t) = \frac{I}{eV} - \frac{\tilde{N}(t)}{\tau_*} - G\big(\tilde{N}(t)\big)|\tilde{E}(t)|^2 \tag{2.1b}$$

The first equation is homogenous and therefore invariant with respect to multiplication by a constant factor, and in the second equation only $|\tilde{E}(t)|^2$ appears. Therefore, whenever $\{\tilde{N}(t), \tilde{E}(t)\}$ is a solution, so is $\{\tilde{N}(t), \tilde{E}(t)e^{-i\Phi_0}\}$ for all real Φ_0. The absolute optical frequency ω_0 of the optical field $\mathcal{E}(t) = \tilde{E}(t)e^{-i\omega_0 t}$ plays no role. Further inspection shows that the optical phase Φ is an enslaved variable which just follows the motion determined by $\tilde{N}(t)$ and $\tilde{E}(t)$. In this model effects like noise, longitudinal spatial hole burning, nonlinear gain, and that the carrier lifetime τ_p is dependent on various effects like non-radiative recombination, are neglected.

In equations (2.1), the optical gain $G\big(\tilde{N}(t)\big)$ of the material determines the stimulated recombination. The simplest model is a linear relation between carrier density and gain of the form $G\big(\tilde{N}(t)\big) = G' \cdot (\tilde{N}(t) - N_t)$, where N_t is the carrier concentration at transparency. If the laser is not operating in a regime where it emits ultrashort pulses, this linearisation usually is sufficient. The optical amplitude $\tilde{E}(t)$ in equation (2.1a) decays because of the finite photon lifetime τ_p. $\Delta\omega$ in equation (2.1a) is the optical frequency shift induced by the injected carriers, as the refractive index n and therefore the optical cavity length is dependent on the carrier concentration. A simple ansatz

in the carrier concentration $N = N(t)$.

[4] The proof of single photon emission by e.g. quantum dots is given by the observation of anti-correlation in a Hanbury Brown-Twiss type correlation experiment, see e.g. [52].

for $\Delta\omega(\tilde{N}(t))$ is $\Delta\omega(\tilde{N}(t)) = \frac{1}{2}\alpha G\big(\tilde{N}(t)\big)$, where α is the linewidth enhancement factor defined as

$$\alpha = -\frac{2\omega}{c}\frac{\partial n/\partial\tilde{N}}{\partial G/\partial\tilde{N}}. \tag{2.2}$$

It describes the amplitude-phase coupling of the optical field due to the dependence of both the refractive index n and gain G on the carrier density $\tilde{N}$ [53]. This nonlinearity is the reason for the enormous feedback sensitivity of semiconductor lasers. If one wants to model nanostructures as e.g. quantum dot devices, one has careful whether this simple definition for α is still valid. α typically has values in the range from 2 to 10. For the devices used in experiment later, α was determined to lie between 5 and 6 [34].

In equation (2.1b) for the carrier density $\tilde{N}(t)$, $\frac{I(t)}{eV}$ describes the number of injected electron-hole pairs, with $I(t)$ as the current density, e as the elementary charge and the active Volume V. The second term accounts for the spontaneous recombination of electron-hole pairs with a mean life time of τ_*, the term $G\left(\tilde{N}(t)\right)|\tilde{E}(t)|^2$ models the stimulated recombination.

We now switch to dimensionless variables. To achieve this, we first replace the slow optical amplitude $\tilde{E}(t)$ in equation (2.1a) by $E(t)e^{-i\omega_{\mathrm{th}}t}$. ω_{th} is the laser frequency at threshold in a stationary regime, which can be expressed as $\omega_{\mathrm{th}} = \omega_0 + \Delta\omega G(N_{\mathrm{th}}) = \omega_0 + \frac{1}{2}\alpha G' \cdot (N_{\mathrm{th}} - N_t)$. Then, $\tilde{N}(t)$ is replaced by $N_{\mathrm{th}} + \frac{2N(t)}{G'\tau_p}$. Finally, we once again rescale $E(t) \mapsto \sqrt{\frac{2}{G'\tau}}E(t)$ and $t \mapsto \tau_p t$. During the transformations, we make repeated use of the relation $G(N_{\mathrm{th}}) = G' \cdot (N_{\mathrm{th}} - N_t) = \frac{1}{\tau_p}$ between threshold gain and photon lifetime τ_p. Using the relation $I_{\mathrm{th}} = eN_{\mathrm{th}}/\tau$ and the shorthand $P := (IV - I_{\mathrm{th}})G'\tau_p/(2e)$, we arrive at the following system of equations:

$$\frac{d}{dt}E(t) = (1 + i\alpha)N(t)E(t) \tag{2.3a}$$

$$\frac{d}{dt}N(t) = \frac{1}{T}\Big(P - N(t) - (1 + 2N(t))|E(t)|^2\Big). \tag{2.3b}$$

$1/T$ is a very small quantity, as it is equal to the ratio of photon lifetime and carrier lifetime in the laser cavity $\tau_p/\tau_* \approx 10^{-3}$. Three parameters determine the dynamics of the dimensionless equations of $E(t)$ and $N(t)$. These are the aforementioned ratio of the timescales T, the pump P and the linewidth-enhancement factor α. In the next chapter, these equations will be extended to include optical feedback and discussed in the context of optical multistability.

Doing a linear stability analysis as outlined in the introduction, one finds two equilibria. The first equilibrium is the "off"-state. It is stable below and unstable above the lasing threshold. The second equilibrium, "on", is unstable below and stable above threshold. There is a bounded range of the applied current above threshold, where the eigenvalues of the characteristic polynomial become imaginary and relaxation oscillations may occur. Combining both equilibria and their stability, we arrive at a picture like Fig. 2.2 (a). The control parameter p is in our case the applied current I, the phase space variable x the photon number S. At threshold current $I_{th} = p^*$, the "off" and

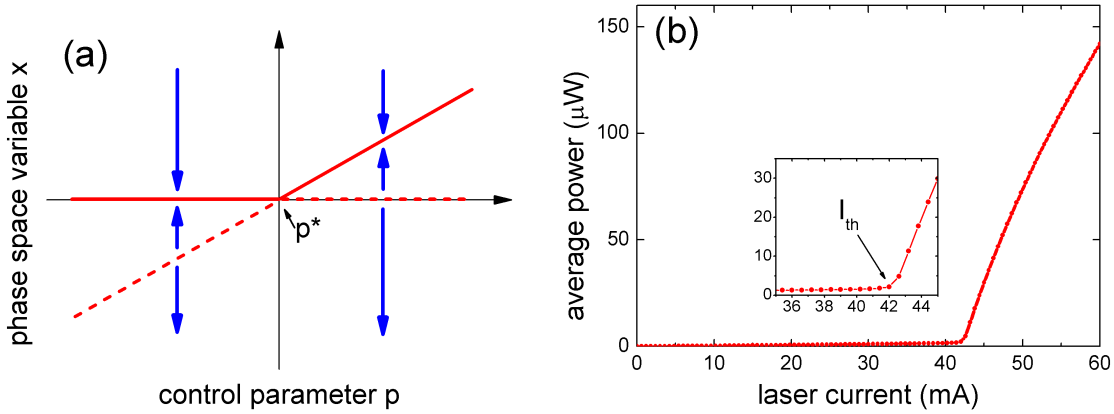

Figure 2.2: The semiconductor laser lasing threshold. (a) Transcritical bifurcation. Full lines, stable fixed points. Only stable fixed points would be observed in experiment. Dashed, unstable fixed points. Arrows, flow. Two different manifolds of fixed points exchange stability at p^*. (b) Emitted average power as function of the laser current for a semiconductor structure used in this thesis. At the threshold current I_{th} the "off" and "on" state of the laser exchange stability, see text. Inset: below threshold the emitted power is not zero because of spontaneous emission.

"on" state of the laser exchange stability, typical for a transcritical bifurcation. Fig. 2.2 (b) shows a measurement of the dependence of emitted light intensity from the applied current for one of the laser structures used in the experiments. Only the stable branches of Fig. 2.2 (a) are accessible in experiment. Although there are small differences of the real device data to the strongly simplified model, the general features are captured very well. In our experiment a non-vanishing intensity is detected already below the lasing threshold. There, the laser acts a light emitting diode. Only a small deviation from linearity is visible in the measured output power with increasing driving current.

A few nanoseconds after a direct current is applied, the output of a typical semiconductor laser diode is stable. The photon and electron densities in the cavity will have settled to some equilibrium value and the laser emission is continuous wave. Besides initial relaxation oscillations, usually no interesting dynamics is observed. This is reflected in the fact that the device can be described very well by the rate equation model (2.3), consisting of two coupled equations for two variables. In such nonlinear equations with two dynamical variables e.g. oscillatory phenomena and related bifurcations can be studied, but no chaotic or other complex behavior is possible [54]. However, the high nonlinearity of the electron-photon coupling makes the laser extremely sensitive to perturbations. Even minimal optical feedback or the injection of an optical signal [55] may drastically alter the laser output[5]. In the following, I will show how complex dynamical behavior may be induced in these devices using delayed optical feedback. At the same

[5]For an overview including a variety of possible mechanisms leading to laser instabilities see e.g. [56] and the references therein.

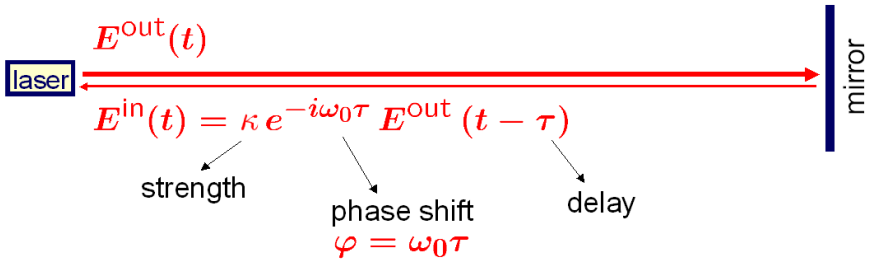

Figure 2.3: Simplified scheme of delayed optical feedback, see text for details. $E(t)$, optical field. ω_0, optical frequency of the solitary laser. τ, round trip time. $\varphi = \omega_0\tau$, feedback phase. κ, feedback strength.

time, all operating parameters can be controlled reliably.

2.2 Coherent Optical Feedback

In technical applications, optical feedback is often avoided by the use of optical isolators, in order to prevent an unexpected deviation from the known operating characteristics. Well-known feedback effects include hysteresis when changing the operating parameters, as well as various types of oscillatory instabilities, see e.g. the seminal paper by Lang and Kobayashi [57]. Furthermore, constructive interference leads to a lowering of the lasing threshold. This threshold lowering is often used to experimentally quantify the feedback strength. Destructive interference can prevent lasing action even above the threshold current of the solitary laser. Feedback may also be introduced deliberately, e.g., to reduce the linewidth of the laser, or to induce a certain desired dynamical behavior like chaotic emission [31]. In our experiments not only hysteresis, but multistability can be observed in broad parameter ranges due to feedback. Two different kinds of oscillatory instabilities of the laser intensity induced by optical feedback are used to investigate the synchronization of quasiperiodic intensity pulsations.

The simplest setup using delayed feedback lets the emitted light be reflected back into the laser by a mirror, Fig. 2.3 show a schematic. In applications a similar situation is encountered often, for example when light is reflected back into the laser by the surface of an optical disc or a fiber end. Such optical feedback may influence e.g. the laser frequency spectrum and threshold gain significantly. It is well known that a laser can operate in different external-cavity modes (ECMs), adjusting to the resonance conditions imposed by the combined external and laser cavities [58]. A few common simplifications are implicit in Fig. 2.3: We assume the solitary laser emits one longitudinal mode only, and that the light is coupled back into the laser after one round trip in the external cavity. The latter approximation is valid as long as the feedback strength, described by the parameter κ, is low. The returning optical field E^{in} is delayed by the round trip time τ. After traversing the external cavity, its phase is shifted with respect to E^{out} by an amount equal to $\varphi = \omega_0\tau$, where ω_0 is the optical frequency of the solitary laser. The same simplifications as in Fig. 2.3 are used in the Lang-Kobayashi (L-K) model of

delayed feedback [57]. The L-K equations add a term corresponding to E^{in} to the rate equation (2.3a) for $E(t)$ given in the introduction, and will be discussed in the next chapter. For now, we will only note that the key parameters determining the dynamics are feedback strength κ and feedback phase φ, and that φ is 2π-periodic.

In experiments, depending on the length of the external cavity very different dynamical regimes have been observed. The cavity length is usually characterized by comparing the delay τ to the timescale defined by the relaxation oscillations (RO). For long cavities $\tau > t_{\text{RO}}$, corresponding to lengths of meters and above[6], holds. The laser switches fast, in an essentially random way, between the densely spaced external cavity modes. As the feedback phase φ is defined with respect to a certain mode, it is not a sensible choice of parameter anymore. When the semiconductor laser is biased near threshold and subject to moderate feedback, power dropouts in the laser intensity [59, 60] are detectable. Increasing the pump current, a drastic increase of the linewidth of the emitted light termed "coherence collapse", has been observed [61]. For the short cavity regime, $\tau << t_{\text{RO}}$ holds. The number of external cavity modes is far lower, as the feedback cavity is a few cm long. The phase shift φ of the optical field now is a well-defined parameter which crucially determines the dynamics [62, 57]. Hysteresis effects [57] and oscillatory instabilities of the laser intensity like regular pulse packages [7] can be observed [62]. The limit $\tau/\tau_{\text{RO}} \to 0$ is the *ultrashort feedback* regime and was first investigated in [64], using our experimental devices. Only a very small number of external cavity modes is involved in the dynamics of the laser. Nevertheless, a huge variety of dynamical regimes can be observed when changing the feedback parameters [25]. Typical relaxation oscillation frequencies are around 10 GHz, resulting in $\tau/\tau_{\text{RO}} \approx 0.01$. At a high feedback strength, the feedback phase can be adjusted for simultaneous lasing of two longitudinal modes [65].

2.3 Multisection Lasers

As introduced in the last chapter, our semiconductor lasers are InGaAsP-InP heterostructures with a center wavelength between of 1535 and 1550 nm. The broad gain profile of the semiconductor material far exceeds the spacing between the longitudinal Fabry-Perot modes of the laser cavity. To achieve lasing of only one longitudinal mode, a periodic index variation is introduced into the upper waveguide by selective etching and overgrowth. This distributed feedback (DFB) grating, see Fig. 2.1 of the last chapter, corresponds to a wavelength selective first-order Bragg grating[8] and leads to a coupling between the forward and backwards propagating optical field. The resulting mode spectrum of the laser is symmetrical with respect to a stop band. Within this wavelength region, reflection at the introduced grating is highly efficient, up to the point that it

[6] Of course, the coherence length of the laser output imposes an upper limit.

[7] Using filtered feedback, the long cavity regime may exhibit similar dynamics [63].

[8] For lasers with feedback along the waveguide, the grating order equals the diffraction order. A first order Bragg grating with a periodicity of one half of the guided wavelength gives feedback in the first diffraction order, the phase shift between diffracted waves from adjacent grating elements is equal to one wavelength.

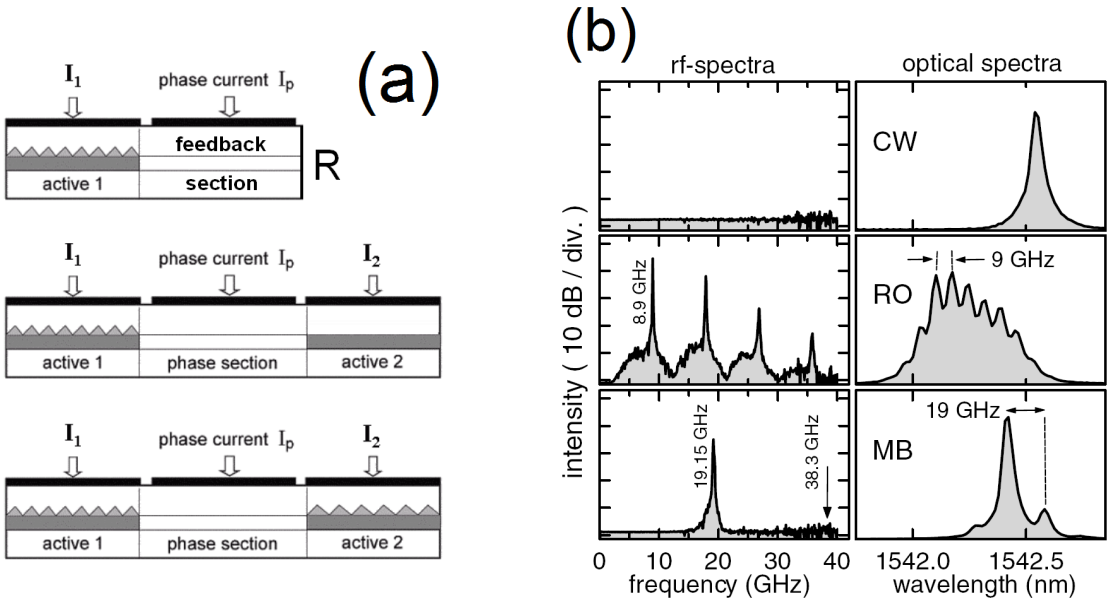

Figure 2.4: (a) Three different types of multisection devices. From top to bottom: passive feedback laser (PFL), active feedback laser (AFL) and integrated tandem laser (ITL). See text for details. (b) Examples of dynamical regimes of an AFL, taken from Ref. [64]. Left, intensity power spectrum. Right, optical spectrum. From top to bottom: continuous wave (cw) emission, relaxation oscillations (RO) and mode-beating oscillations (MB) of the emitted light intensity.

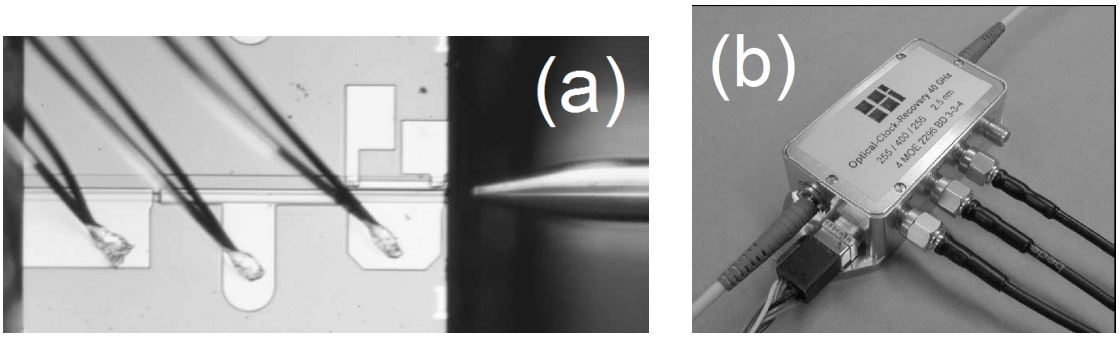

Figure 2.5: (a) An active feedback laser (AFL) as seen under a microscope, image taken from Ref. [66]. From left to right: amplifier section, phase section and DFB laser section with current leads, as well as an optical fiber. Device length is below one millimeter. (b) Packaged AFL, image taken from Ref. [34]. Bottom left: optical fiber connected to DFB section, temperature controller connector. Bottom right: cables to individually apply currents to the three sections. Top right: optical fiber connected to active section.

counteracts wave propagation. The two modes on both sides of the stop band have the lowest threshold gain. An inhomogeneous carrier density distribution in our devices, resulting from a nonuniform power distribution in the laser cavity, tends to stabilize the short wavelength stop-band mode [34]. Stable operation of this single mode is achieved. The optical field of the DFB laser is guided in longitudinal direction by a ridge. Such DFB lasers can be grown on the wafer as part of a more complex structure. Further sections with different functionality can be joined to the laser section. All internal borders between sections have reflectivities below 10^{-4} [66]. Three different types of integrated devices have been fabricated at the Fraunhofer Heinrich Hertz Institute in Berlin.

Passive feedback lasers. The first idea to realize on-chip feedback was to add a section consisting of semiconductor material with a higher band gap. Laser and passive section can be separately biased with a direct current and are mounted on a common diamond heat sink. In Fig. 2.4 (a) a simplified scheme of the device, called passive feedback laser (PFL), can be found. It is manufactured by removing the active layer and upper waveguide of the DFB laser structure in this part of the wafer, and successive overgrowth of 1.3 μm band gap material. The laser light propagates in this feedback cavity when the passive section is pumped above optical transparency. The cleaved facet of the passive section which is not adjoined to the laser section acts as a mirror. As the band gap of the passive section is larger, no amplification of the 1.5 μm laser emission is achieved. Intraband transitions lead to increasing losses with increasing section length. Changing the refractive index of the semiconductor material in the passive section by an applied current, the optical length of the cavity and therefore the delay time τ can be varied. Two distinct types of intensity self-pulsations born in super- and subcritical Hopf bifurcations could be observed [64].

Active feedback lasers. In order to be able to adjust both feedback phase φ and feedback strength κ independently, an additional amplifier section was added to the phase section[9]. Besides the missing wavelength-selective grating, this active section is identical to the laser section. The cleaved outer facet has a power reflectivity of $R \approx 0.3$. The optical losses in the external cavity formed by both passive and active sections now can be compensated and κ can be changed by applying a direct current. Extending the range of the control parameters, the frequency tuning ranges of the mode-beating self-pulsations were significantly enhanced [25]. For high feedback strengths both RO and MB self-pulsation types may coexist. A microscope image looking at the top of an active feedback laser (AFL) chip can be seen in Fig. 2.5 (a), a schematic side view in the middle panel of Fig. 2.4 (a).

Laser tandem devices. Instead of an active section a second, nearly identical DFB laser can be added. Coupling delay and waveguide losses between both DFB lasers are determined by the passive section, see Fig. 2.4 (a). As previously, the delay τ can be changed by a direct current. Both lasers can be spectrally detuned by adjusting their bias current. This integrated tandem device (ITL) allows to e.g. systematically study

[9] If just an active section were used instead of separate passive and active sections, the self adjustment of the feedback phase to the carrier density in the active section would prevent independent tuning of φ and κ.

the dynamical effects a finite coupling delay has on synchronization between the two lasers [67]. An integrated tandem laser (ITL) shows similar dynamical regimes when compared to an AFL. For two reasons we will use an ITL to generate the master frequency in the synchronization experiments detailed later on: First, by detuning the lasing wavelength of both lasers, mode-beating intensity pulsations involving two different longitudinal modes can be observed and changed in frequency very comfortably. Second, the center lasing wavelength of the DFB lasers is shifted by 15 nm compared to the lasers in the AFL by material design, ensuring optically nonresonant locking.

After initial selection and characterization, the multisection devices are mounted on a heat sink and packaged into a module, see Fig. 2.5 (b). They can be controlled by three (PFL) or four (AFL, ITL) external parameters. These are the temperature T measured at the heat sink, the laser current I_d and the currents applied to the passive (I_p) and active section (I_a), respectively. The experimental validation of the device design and a characterization of various dynamical scenarios can be found in Refs. [34, 66, 68]. For the dynamical regimes investigated in the next chapters, two phenomena are relevant. When tuning the feedback parameters, hysteresis effects can observed. I will delay their discussion until the next chapter. Intensity pulsations are the second phenomenon, which I will introduce in the following section.

2.4 Intensity Pulsations Due to Delayed Feedback

The emission of an multisection laser is within two separate frequency domains. The optical carrier with a center wavelength of around 1540 nm corresponds to a frequency of a few hundred THz. The intensity envelope of the fast carrier can also be periodically modulated. Undamped relaxation oscillations (RO) are found in the range from 2 to 20 GHz. Mode-beating phenomena (MB), corresponding to the beat frequency of two coexisting optical modes, typically start at 20 GHz and have been experimentally observed up to 50 GHz. In device-realistic simulations, they can be shown to span a range extending up to a few hundred GHz. These intensity pulsations are e.g. interesting for applications in telecommunication, where they can be used as information carrier and timebase.

In Fig. 2.4 (b) both optical spectrum and power spectrum of a cw state, an RO pulsation and an MB pulsation are shown. The cw emission is single mode, no peaks can be observed in the power spectrum. The intensity pulsation of RO type has a broad comb of modes in the optical spectrum. The separation of the optical modes corresponds to the RO frequency. The power spectrum shows the generation of multiple strong higher harmonics in addition to the RO frequency. For MB, only two modes are visible in the optical spectrum. The distance between the weak side mode to the dominant lasing mode corresponds to the MB frequency. In the power spectrum, only a weak second harmonic can be observed. I will now describe two typical ways these two oscillation types can develop when tuning the device parameters.

In the low feedback range, a single mode governs the dynamics of the laser. Initiated by noise in the laser, relaxation oscillations may occur. They can become undamped in

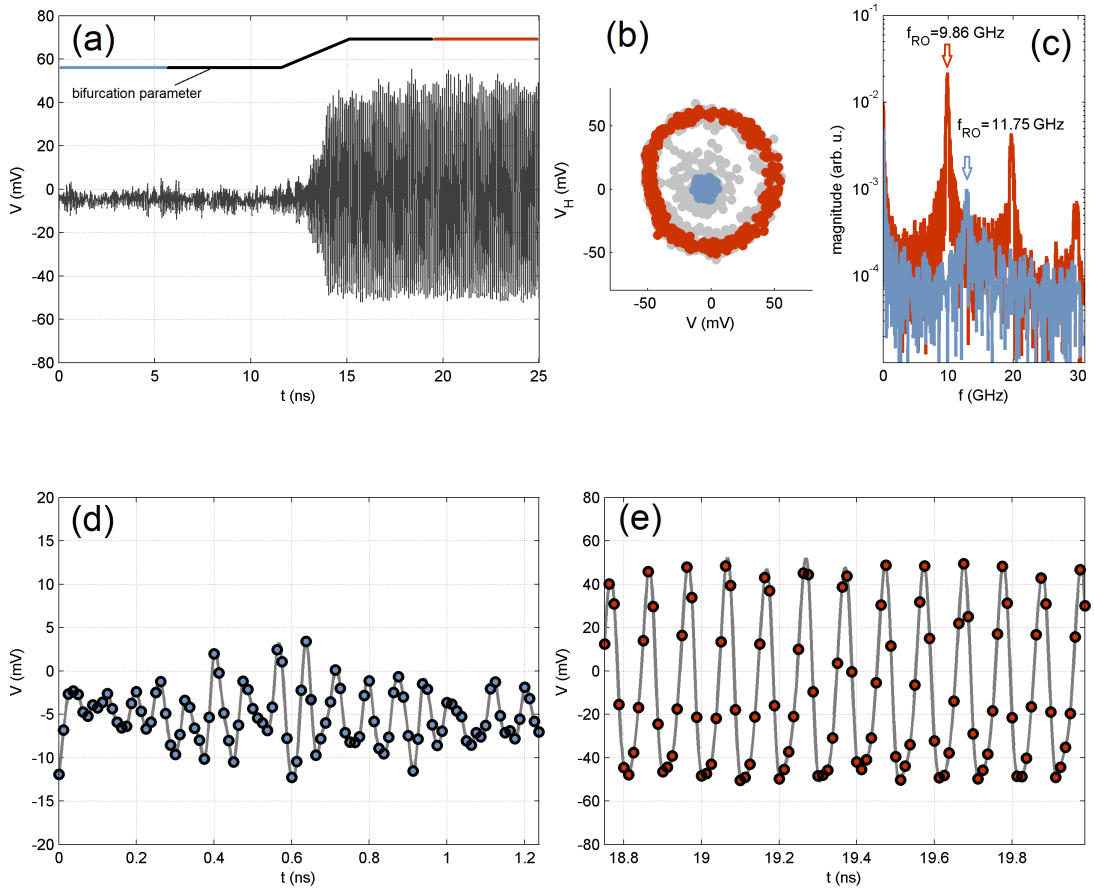

Figure 2.6: Time-resolved measurement of passing a supercritical Hopf bifurcation in an active feedback laser. $I_d = 90.01$ mA, $I_a = 11.52$ mA. (a) I_p is initially set to 11.52 mA and increased by a small modulation of the phase current, starting at $t = 12$ ns. The relaxation oscillations are undamped when passing the supercritical Hopf bifurcation. (b) Two-dimensional embedding of the time series in (a) using the Hilbert-transform [3]. Blue dots, cw state with damped RO from $t = 0$ ns to $t = 6.25$ ns. Red dots, limit cycle formed by the self-pulsation, $t = 18.75 - 25.00$ ns. (c) Power spectra of (a). Blue line, $t = 0$ to 6.25 ns. Red line, $t = 18.75 - 20$ ns. (d) Relaxation oscillations in (a). A low-amplitude peak at $f_{\mathrm{RO}} \approx 11.75$ GHz is visible in the power spectrum (c). (d) Fully developed self-pulsation of RO type in (a). The power spectrum in (c) shows higher harmonics at $2f_{\mathrm{RO}}$ and $3f_{\mathrm{RO}}$. See also Fig. 2.7.

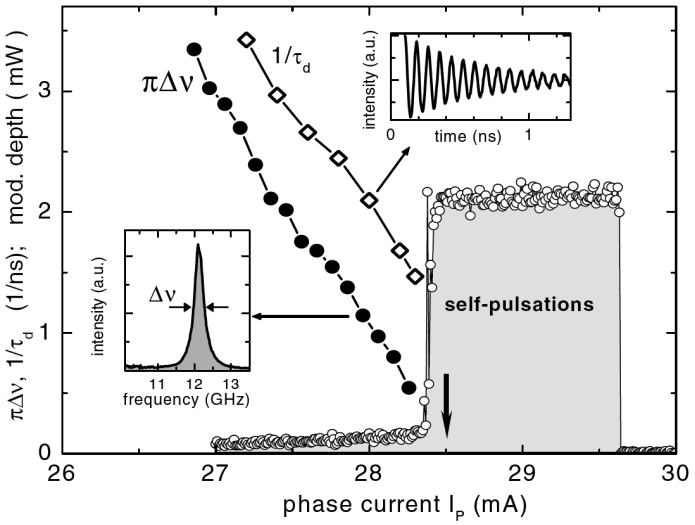

Figure 2.7: Relaxation oscillations in an active feedback laser. The RO are undamped in a subcritical Hopf bifurcation when increasing the phase current I_p. τ_d^{-1}, damping rate. $\pi\delta\nu$, resonance width. The insets show the measured power spectrum of the strongly damped low amplitude oscillation and a corresponding time trace, computed using a device-realistic simulation tool. The abrupt end is due to a jump to the next lasing mode. Figure taken from Ref. [18].

super- or subcritical Hopf bifurcations [18, 4]. In Fig. 2.6 (a), the laser intensity variation detected by a photodiode while passing a supercritical Hopf bifurcation is shown. To this purpose, the driving currents of the AFL used in the next chapter have been set to $I_d = 90.01$ mA, $I_a = 11.52$ mA and $I_p = 11.52$ mA. The phase current is the bifurcation parameter and was increased by the output of a function generator, which was coupled to the direct current with a high bandwidth bias tee. The time traces of the laser intensity have been recorded with an ultrafast u2t photodiode and an LeCroy Wavemaster 8 Zi oscilloscope with 30 GHz bandwidth and 80 Gs sample rate.

Panels (d) and (e) show the first and last 6.25 ns of Fig. 2.6 (a), note the different scale of the y-axis in (d). Within the first 12 nanoseconds, the laser is in a cw state with noise driven damped relaxation oscillations. While this low amplitude intensity variation is very irregular, a peak at 11.75 GHz can be seen in the power spectrum, see the blue curve in panel (c). If one slowly increases the phase current by hand, this peak will smoothly decrease in frequency and width, while increasing in magnitude. In panel (a) the Hopf bifurcation is passed within only 3 ns, but the laser follows the fast change almost instantly, adjusting to any change of the phase current within few oscillatory cycles. A high amplitude self-pulsation of RO type develops, see panel (e). The RO frequency has decreased to 9.85 GHz and the higher harmonics $2f_{\mathrm{RO}}$ and $3f_{\mathrm{RO}}$ appear in the red power spectrum of panel (c). In panel (b) the embedding of the signal in (a) in a two-dimensional phase space, constructed by a Hilbert transform[10] of the recorded voltage, can be seen. The first 6.25 ns of the cw state with RO have been plotted with blue dots. The red dots show the limit cycle formed by the fully developed self pulsation during the last 6.25 ns.

An example for the undamping of RO due to a subcritical Hopf bifurcation can be seen in Fig. 2.7. The phase current is increased again with all other parameters fixed, but at a different point of operation. Power spectra measured by an rf spectrum analyzer with 40 GHz bandwidth, recorded while slowly tuning the phase current, are used. The damping rate τ_d^{-1} and resonance width $\Delta\nu$ of a damped RO with a low amplitude decrease. The insets show the measured power spectrum of the damped low amplitude RO oscillation recorded and a corresponding exemplary time trace, computed using a device-realistic simulation tool. Tuning I_p, suddenly a stable undamped self-pulsation with a large amplitude sets in. The very different nature of noise driven RO and fully developed self-pulsations of RO type is clear from Fig. 2.6. The true location of the Hopf bifurcation can be extrapolated by the linearly decreasing damping rate and is marked by an arrow. The abrupt end of the RO pulsation is due to the laser jumping to a different external cavity mode when further increasing the phase current.

Increasing the feedback strength κ, the number of accessible modes is increased and beating phenomena of two simultaneously lasing longitudinal modes can be observed. The mode spacing in a short cavity is large. Corresponding very high frequency intensity pulsations, which can be significantly faster than RO, have been theoretically predicted early [29]. In contrast to Fig. 2.7, the damping rate in Fig. 2.8 does not decrease, while the pulsation amplitude increases smoothly from nearly zero when changing I_p.

[10] See e.g. the appendix of Ref. [3] for technical details.

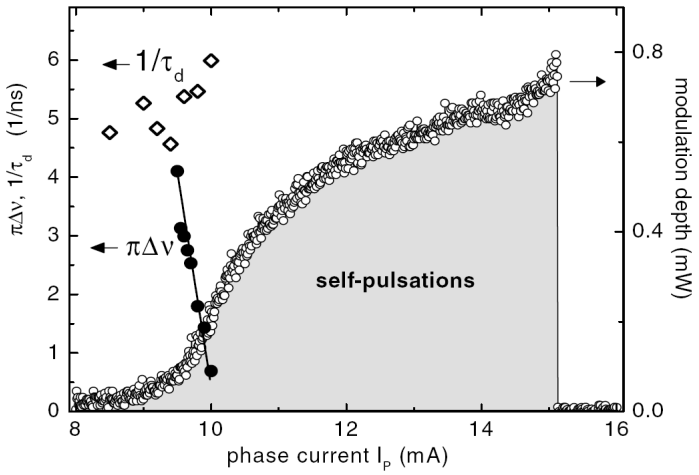

Figure 2.8: Mode-beating oscillations in an active feedback laser. The MB oscillations are undamped in a supercritical Hopf bifurcation when increasing the phase current I_p. τ_d^{-1}, damping rate. $\pi\delta\nu$, resonance width. The abrupt end is due to a jump to the next lasing mode. Figure taken from Ref. [18].

This smooth amplitude increase of the pulsation is again typical for a supercritical Hopf bifurcation, like already discussed in the context of Fig. 2.6. In the optical spectrum, a side mode starts to grow next to the lasing mode, see Fig. 2.4(b). The MB frequency visible in the power spectrum is equal to the difference between both optical frequencies. The abrupt end of the MB pulsation is, as for RO in Fig. 2.8, due to the laser jumping to a different external cavity mode.

At even higher feedback levels both RO and MB may coexist. The location of regions with such quasiperiodic pulsations in the plane of the feedback parameters I_p and I_a is shown in Fig. 2.9 (a) for one exemplary pair of lasing modes (shaded black). First, MB pulsations are undamped in areas shaded gray. Then, RO are undamped in a torus bifurcation, see also Fig. 4.3 on page 58. RO and MB interact and may synchronize to each other at resonant 1:n ratios. Exemplary power spectra when following along a line connecting the resonances in Fig. 2.9 (a) are shown in Fig. 2.9 (b). The mutual locking ranges of RO and MB decrease with increasing order n. These mutually coupled intensity pulsations generated by an active feedback laser will be used in chapter 4 to investigate synchronization processes of quasiperiodic oscillations.

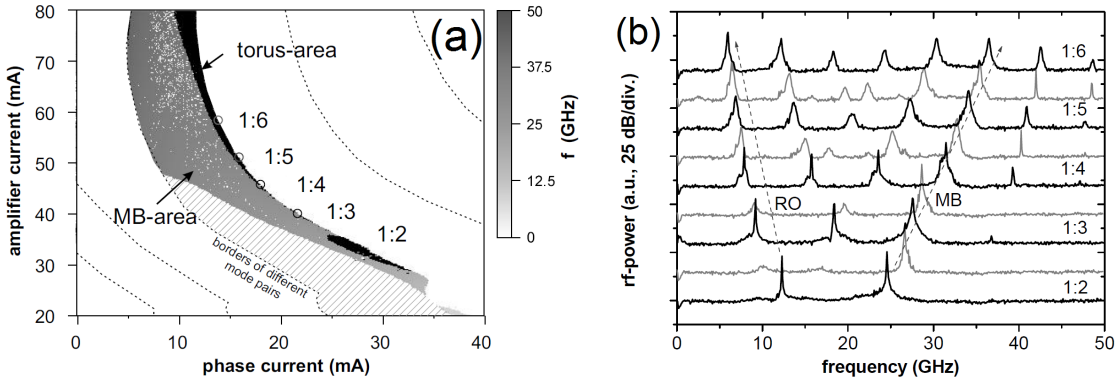

Figure 2.9: Quasiperiodic intensity pulsation regimes in a free running multisection laser. (a) (I_a,I_p) plane, $I_d = 70$ mA. Only power spectra of one period of the feedback phase φ are evaluated. Hatched, cw emission. Shaded gray, intensity pulsations where the rf-power of the main spectral peak exceeds the noise floor of the ESA by at least 10 dB. Peak frequency is encoded by gray scale. Black, regions of quasiperiodic pulsations. The locations of the resonances with integer frequency ratios are marked by circles. (b) Power spectra along the location of the resonances in (a). Black, quasiperiodic resonances with integer $\theta = f_{\mathrm{MB}}/f_{\mathrm{RO}}$. Gray, intermediate nonresonant cases. Dashed arrows, direction of the shift of RO and MB peaks. Figures taken from Ref. [34].

3 Multistability due to Ultrashort Delayed Optical Feedback

Bistable devices are key elements of modern computer and communication technology. In nonlinear optical systems hysteresis effects and therefore bistability are common. The simultaneous coexistence of two stable states with either steady, periodic or chaotic dynamics has been observed in a variety of experiments, see e.g. Ref. [69]. Whether the number of coexisting stable states can exceed two is a crucial question in the context of bistability. The existence of any extra state may create the possibility of sudden jump out of the binary states, even by a small intrinsic perturbation (noise). In the following, I will adopt the common convention of using the term *multistable* for systems with more than two coexisting stable states. Multistable devices can be used for a wide variety of purposes, such as higher-order logic gates or switching elements in optical communication circuits. Therefore, the investigation of multistability in physical systems is an active area of research. Prominent examples include semiconductor ring lasers [70], and especially the design of tristable devices like liquid crystals [71] and optical flip-flops [72].

In this chapter, I present an experimental and theoretical study of multistable emission of a semiconductor laser subject to delayed optical feedback. First, I will give a short introduction to optical multistability with a specific example. Following this, the experimental setup and data is presented. Our experimental device is an active feedback laser (AFL), as introduced in the previous chapter. The all-optical feedback is integrated on the same chip as the laser. Closely above the lasing threshold, a new regime of tristability is found. For the same operating parameters the laser emits continuous wave (cw) with one of three possible wavelengths. Very close to threshold it might even be switched off, with two further cw lasing states available. The emission wavelengths are in the infrared, within a range typically used in optical telecommunication. The spacing between the wavelengths is compatible with dense wavelength division multiplexing (WDM)[1]. Therefore, the findings presented here may have an immediate practical interest, as the device could potentially be used as an all-optical switching device. The experimental results are then compared to theoretical investigations in the framework of the Lang-Kobayashi model of delayed feedback [57]. The latter provide a consistent understanding of the experimental findings. Furthermore, a systematic way to increase the maximum number of coexisting states is revealed. The main results of this chapter were published in Ref. [73], and are extended by discussing the dependence of the multistability on the distance from the lasing threshold [74, 75].

[1] WDM is a scheme where multiple optical carrier signals are transmitted by a single optical fiber at the same time, using different wavelengths.

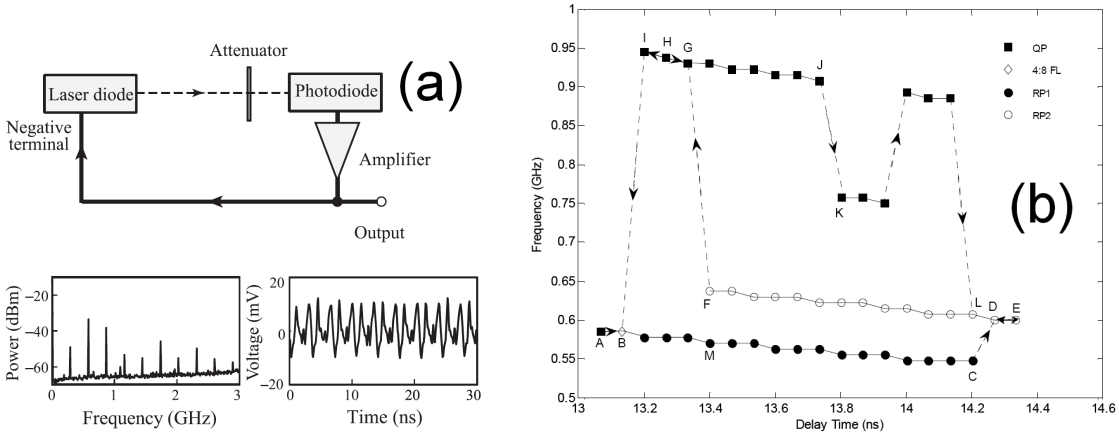

Figure 3.1: Multistability in a semiconductor laser due to optoelectronic feedback with a variable delay time, figures taken from Ref. [76]. (a) Experimental setup with feedback loop. Lower panels: power spectrum and time trace measured for a delay of 13.13 ns. (b) Depending on the delay time, the output intensity variation can be regular pulsing (RP1, RP2), 4:8 frequency locked (FL) or quasiperiodic (QP).

3.1 Multistable Optical Systems

Compared to bistability, only few experimental realizations of optical multistability have been reported, e.g., using atomic vapor in optical cavities [77]. CO_2 and doped fiber lasers under periodic parameter modulation have also shown more than two coexisting states, each either periodic or chaotic [78, 79, 80]. Without such periodic parameter modulation, multistability has been observed with semiconductor laser diodes either by complementing the optical devices with electronic circuits [81, 82, 76], absorptive-dispersive optical filters [83], or by splitting the resonator in two Fabry-Perot sections coupled via an air gap [84]. These examples illustrate in particular that multistability achieved by added feedback loops may be the result of a variety of different nonlinear mechanisms. Even if the solitary system is linear, nonlinearity within the feedback loop can lead to multistability.

An increase of the nonlinearity often has two competing effects. On one hand, it leads to an increase in the number of possible stable states. On the other hand, instabilities like self-pulsations may be introduced and hysteresis loops are becoming increasingly complicated. As a result the individual states might cease to be experimentally accessible or stable in a sufficiently large parameter range. Lasers with long external feedback cavities, the latter at least a few tens of centimeters long, serve as an illustrative example. Although they may have a huge number of coexisting modes, these are so densely spaced that minimal noise leads to random jumps between them. Multistability of high degree is present, but each individual state cannot be used selectively. The ability to control the system sufficiently well to access the different states often is the key experimental

difficulty. The configuration with an ultrashort cavity investigated in our experiment allows for very good control of the coexisting states, while keeping all advantages of all-optical feedback.

An experimental setup using feedback to achieve multistability is presented in Fig. 3.1 (a). We will discuss it here to point out some important and common issues which are resolved in our setup. As in our experiment, a semiconductor laser is combined with a single feedback loop. The output of a single-mode distributed feedback InGaAsP/InP laser diode passes an attenuator and is converted to an electrical current by a photodiode. The intensity of the emitted light after passing the attenuator is kept as a feedback parameter, but the optical phase and wavelength are lost. The electrical signal then passes a variable electrical delay line, after which it reaches the negative terminal of the laser diode. The laser bias current is lowered proportional to the photocurrent, delayed by the chosen delay time τ. Depending on τ and the history of the system, multiple dynamical states of the laser diode can be accessed for the same operating parameters. They are characterized by the variation of the laser output power detected by the photodiode, see the lower two panels of Fig. 3.1 (a) for an example of a recorded time trace and the power spectrum for $\tau = 13.13$ ns. Fig. 3.1 (b) shows that for a fixed value of the delay time τ, up to three different types of intensity pulsations can be observed, depending on how the delay time τ has been varied beforehand. While multistability is clearly present, important questions remain unresolved: The physical mechanisms leading to the pulsations are unknown, so no statement on the generality of the observed phenomena can be made. They might be specific to the laser structure and setup used. A very limited range of the control parameter is accessible, as the delay can be varied only in a small range. It is not known, whether the figure in Fig. 3.1 (b) gives a complete account of all possible states for variations of τ, or not. What happens when other parameters like the feedback strength or laser pump current are changed has not been investigated. In our experiment, all experimental aspects are accessible to a very good theoretical understanding, e.g., the physical mechanisms behind the different possible intensity pulsations are known. All parameters can be controlled in wide ranges. Furthermore, as the model used to describe our setup is very generic, the scenario does not depend on the specifics of our laser or experiment.

3.2 Experimental Verification of Multistability

3.2.1 Experimental Device and Measurement Setup

The experimental setup is shown in Fig. 3.2. The ultrashort device used in the experiments is an AFL fabricated by the Fraunhofer Heinrich-Hertz-Institut, see Ref. [34] for technical details. Its center wavelength is in the infrared at $\lambda \approx 1537$ nm. A Profile 8000 mainframe equipped with current sources (not pictured) provides three direct currents with an accuracy of ± 0.05 mA. These currents are used to individually bias the distributed feedback (DFB) laser section (I_d), and the passive (I_p) and active (I_a) sections forming the feedback cavity. The device is mounted on a heat sink, which allows the temperature to be stabilized at 20.01 ± 0.01 °C during the experiments. The light passes

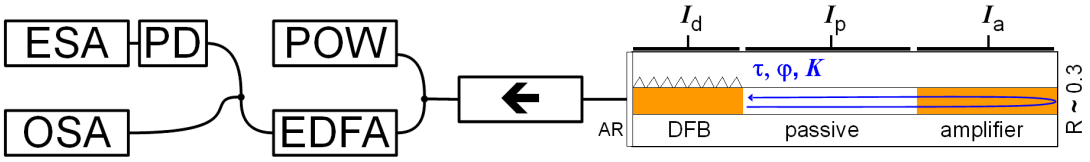

Figure 3.2: Schematic side view of the multisection device and sketch of experimental setup. DFB current I_d, phase current I_p, and amplifier current I_a are supplied with an accuracy of ±0.05 mA. The temperature is stabilized at 20.01±0.01 °C. Light emitted from the anti-reflection (AR) coated DFB facet is coupled into a single mode fiber and analyzed after passing an optical isolator (arrow). POW, optical power meter. EDFA, erbium doped fiber amplifier. OSA, optical spectrum analyzer (HP 71451-B). PD, u2t photo diode. ESA, electrical spectrum analyzer (Rohde & Schwarz FSP 9).

an optical isolator and is analyzed by a NOYES OPM4 optical power meter (POW). After amplification by an Alcatel erbium doped fiber amplifier (EDFA), a HP 71451-B optical spectrum analyzer (OSA) is used to measure the optical spectrum and an u2t ultrafast photo diode (PD) attached to a Rohde&Schwarz FSP 9 electrical spectrum analyzer (ESA) to analyze the power spectrum. The integrated laser device realizes the limit of an ultrashort feedback cavity, as the delay due to the round-trip time in the feedback sections is $\tau \approx 20$ ps. The length of the 800 μm feedback cavity[2] is of the same order of magnitude as the length of the laser (200 μm) itself. Further important parameters of the feedback loop are the optical phase shift along the round trip $\varphi = \omega_0 \tau$, taken at the frequency ω_0 of the feedback-free DFB laser, and the feedback strength K as the ratio of in- and outgoing field amplitudes at the interface between the DFB laser and the passive section.

Various features are markedly different from other approaches, e.g., the lasing states are long-time stable and single-mode continuous wave. Comparing Fig. 3.2 to the experimental setup using electro-optical feedback in Fig. 3.1, the number of components is significantly reduced by leaving out the electro-optical conversion, making our setup very robust against external perturbations and avoiding potential limitations of the switching speed introduced by a photodiode. Every device besides the AFL itself is only used to characterize the laser output. Furthermore, by using all-optical feedback the optical phase shift between emitted and re-injected light is kept as a key feedback parameter. In the following sections we will detail why this phase shift, combined with the strength of the feedback and the intrinsic nonlinearity of the semiconductor material, is a crucial parameter for multistable operation.

[2] 550 μm long passive section, 250 μm long active section.

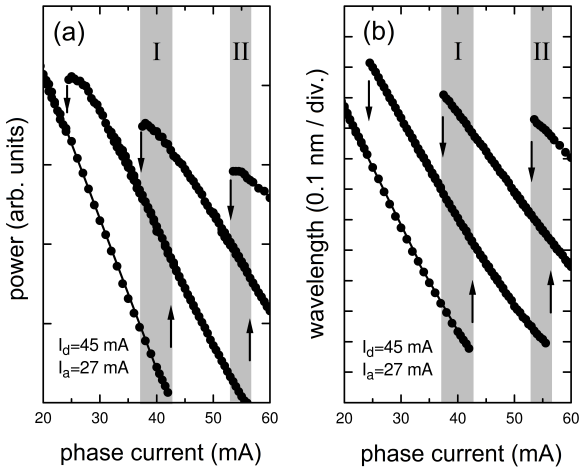

Figure 3.3: Power (a) and wavelength (b) of AFL emission versus phase current I_p at $I_d = 45$ mA and $I_a = 27$ mA. Vertical arrows: mode jumps at the end of stable branches. Regions of tristability (I and II) are shaded gray.

3.2.2 Tristability when Changing the Phase Current

It is well known that our device exhibits hysteresis effects [25]. For a given DFB laser current I_d, φ and K can be independently varied over wide ranges by properly choosing the driving currents I_p and I_a for the passive and the amplifier sections. In the context of traversing hysteresis loops by variation of parameters, the speed of the parameter variation itself is important. In some cases, sudden perturbations may lead to otherwise unaccessible states [85, 86]. Here, the corresponding parameter variations are slow compared to the typical timescales of the laser system. Exploiting the ability to vary all relevant feedback parameters without changing the device itself, different types of bifurcations, self-pulsations [87] and optical chaos have already been revealed, and even applied in optical data communication [88]. In all the investigated regimes, the DFB laser has been pumped well above the lasing threshold. Multistability appears in a different regime of operation, when the DFB section is biased only slightly above the lasing threshold.

We consider an example where the current applied to the DFB section is only 2.5 mA higher than the threshold current $I_d^{\mathrm{th}} = 42.5$ mA. The amplifier current I_a is kept at 27 mA, while the phase current I_p is both increased and decreased. Under these conditions, the laser emits continuous wave (cw), as confirmed by optical spectra (OSA) and power spectra (ESA). The emission wavelengths and powers plotted in Fig. 3.3 exhibit cyclic variations corresponding to roughly three 2π-cycles of φ. These variations are not continuous, but appear as sequences of finite branches with negative slope. Each branch belongs to a certain optical mode of the compound cavity. At the edge of a branch, the wavelength jumps to the next mode. The different branches exhibit a considerable overlap. In particular, two regions of tristability are visible, (I) ranging

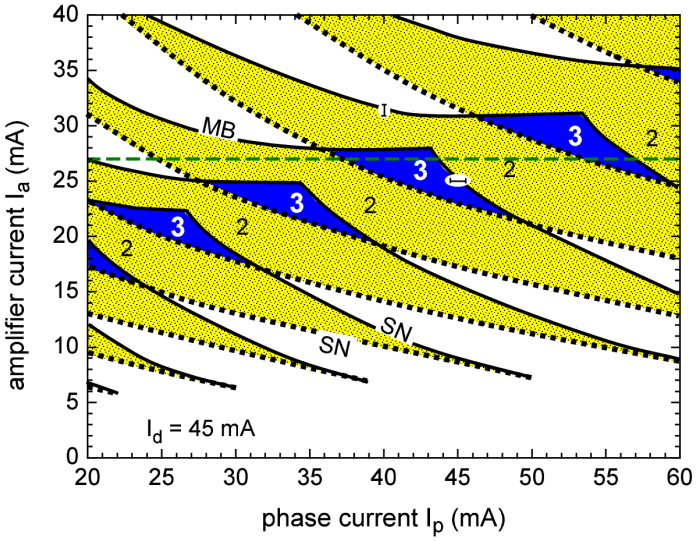

Figure 3.4: Domains of multistability in the (I_p,I_a) plane for I_d = 45 mA. Solid lines, mode jumps forward (increasing I_a or I_p). Dotted lines, mode jumps for backward tuning. MB, mode-beating instability. SN, saddle-node bifurcation. Digits, number of coexisting stable states. Domains of bistability and tristability are dotted (yellow) and dark grey (blue), respectively. Horizontal dashed line (green), cut expanded in Fig. 3.3 (a,b).

from around 37 to 43 mA and (II) from around 53 to 56 mA. All coexisting states are long-time stable; no spontaneous jumps are observed within hours.

No tristability is observed in other cycles at smaller or larger phase currents. Subsequent phase cycles differ slightly from each other, which can be understood as follows. The phase tuning section is passive because its band gap exceeds the photon energy of the laser. Interband transitions are prevented this way, but free-carrier intraband absorption takes place. The latter increases with the injection level and reduces the feedback amplitude. The maximum output power in a branch is reduced as the phase current is increased, see (a). Thus, the different feedback phase cycles shown in Fig.3.3 are not equivalent but belong to different feedback amplitudes. We can conclude that tristability appears not only in a limited range of feedback phase, but also requires a certain medium strength of feedback.

3.2.3 Experimental Phase Diagram

In order to explore the systematics of the observed tristability, scans of the (I_a,I_p) parameter plane were conducted for I_d = 45 mA. The phase and amplifier currents were tuned in steps of 0.05 mA upwards and downwards between zero and 100 mA. Measured positions of mode jumps and degrees of multistability are viewed in in the phase diagram of Fig. 3.4 in a representative 60 mA by 40 mA window. A green dashed line marks the line I_a = 27 mA, along which power and wavelength were measured for varying

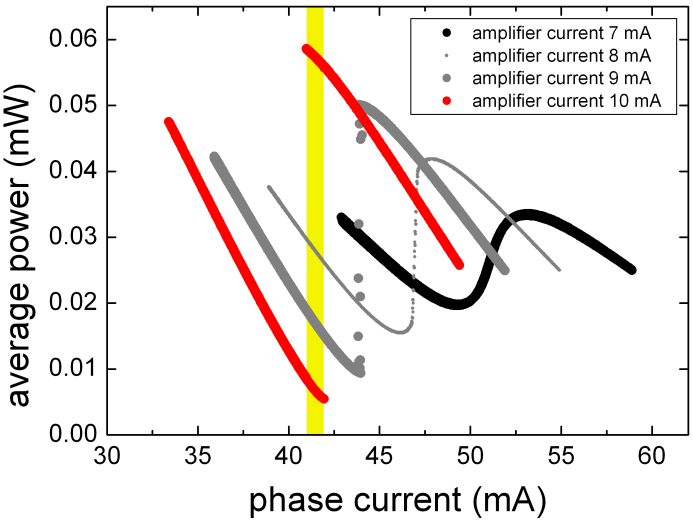

Figure 3.5: Formation of a fold, see also Fig. 3.4. I_d=45 mA and I_a=7-10 mA. For each value of I_a the phase current I_p is increased and decreased, and the variation of the average power corresponding to roughly one period of the feedback phase φ is plotted. The center and therefore the location of the fold changes to smaller phase currents, because a change of I_a also leads to a refractive index change in the amplifier section, in turn changing φ slightly. The bistable region for $I_a = 10$ mA is shaded yellow (gray).

I_p to obtain Fig. 3.3. Looking at Fig. 3.3 discussed above, it is clear that the phase diagram Fig. 3.4 is a projection of a very complex fold structure onto the plane spanned by the two control parameters. In the white regions of Fig. 3.4, only one stable state exists. Regions with multiple coexisting stable states are colored. Yellow regions indicate bistability, blue regions three coexisting stable states for the same feedback parameters. Several occurrences of blue tristable islands are observed. They are equivalent to each other, i.e., their feedback phases φ differ only by integer multiples of 2π and the estimated feedback is always around 3% of the intensity. The upshift of the tristable islands with increasing phase current I_p is a consequence of a larger free carrier absorption within the phase section, which must be compensated by a higher amplification. Solid and dotted lines in Fig. 3.4 represent wavelength jumps with a corresponding jump in optical power for forward and backward current tuning, respectively. They emerge from cusps at small amplifier currents, below which no hysteresis appears.

Formation of Folds

In Fig. 3.5, the transition from non-hysteretic behavior to the formation of a discrete mode jump is shown for one of the cusps in the phase diagram of Fig. 3.4. One full period of the feedback phase is shown. At $I_a = 7$ mA, a variation of the phase current and therefore φ leads to a cyclic variation of the output power of the lasing mode. No

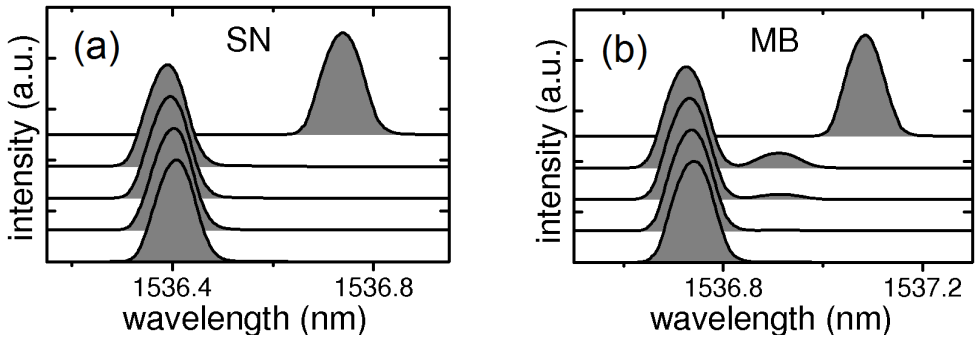

Figure 3.6: Evolution of the optical spectra when crossing the SN and the MB borders along 1 mA long intervals as indicated in Fig. 3.4. Peak heights are normalized. In (b), a second optical mode is observed immediately before the jump. In the power spectrum, a frequency matching the inverse of the center wavelength difference between both peaks can be detected.

hysteresis occurs when tuning I_p. The amplifier current was increased stepwise. The average slope of the power increases with increasing I_a. At the same time, the center of the chosen feedback phase period changes to lower values of I_p due to the change of the refractive index in the amplifier section. At $I_a = 8$ mA the slope is almost vertical, and a fold is formed for higher amplifier currents. Two discrete branches of optical power are visible at $I_a = 9$ mA. Minimal fluctuations of the driving currents lead to artifacts in the immediate vicinity of the mode jump, where then both high and low power state contribute to the averaged power. For $I_a = 10$ mA a small region with hysteresis, shaded yellow, is detected when the phase current is increased and decreased. The two branches of the output power belong to two distinct optical modes. The overlap of the two branches increases when increasing the amplifier current further, corresponding to a widening of the bistable yellow region in the phase diagram Fig. 3.4. Eventually, the width of the hysteresis region exceeds one feedback phase period and tristability appears.

According to the model outlined later, a fold is formed above the cusp in Fig. 3.4 and the bistable region is bordered by saddle-node (SN) bifurcations. With increasing feedback strength the fold widens and the range of bistability grows. The two overlapping red branches for $I_a = 10$ mA in Fig. 3.6 are actually connected by an unstable branch, which cannot be observed in our experiment[3]. The unstable branch originates and ends at the SN bifurcation points where the mode jumps occur.

Characterization of the Mode Jumps

The overlap of the fold is maximal at a kink of the upper border of a tristable region shown in the phase diagram in Fig. 3.4, beyond which it declines again. The kink in the solid line indicates the touching or crossing of two bifurcations. Indeed, optical spectra

[3]Non-invasive stabilization of such unstable steady states has been investigated theoretically in Ref. [89], and might be realized with the setup by Schikora *et al.* presented in Ref. [27].

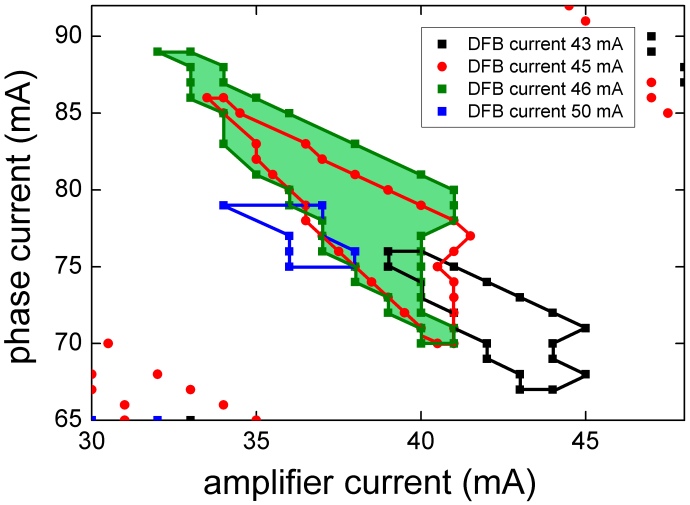

Figure 3.7: Area enclosed by a tristable region in the (I_a, I_p) parameter plane for varying the laser current I_d. Full symbols, jumps up (down) from the lowest (highest) branch with increasing (decreasing) amplifier current. The tristable region is maximal at $I_d \approx 46$ mA.

differ considerably before passing the lines left and right from the kink by increasing the driving currents. For two exemplary mode jumps marked by small bars in Fig. 3.4, the accompanying optical spectra are shown in Fig. 3.6. In Fig. 3.6 (a) the emission keeps single mode until SN, after which the laser jumps to a new emission wavelength. In contrast to this, a side mode starts to grow when approaching the line labeled MB, see Fig. 3.6 (b). A mode-beating (MB) peak with an increasing amplitude can be observed in the power spectrum. The peak frequency is equal to the beat frequency of both optical frequencies. Once the side mode in the optical spectrum reaches a critical amplitude, which is still small compared to the main mode, the emission jumps to the next branch of single-mode operation. Mode jumps when decreasing the driving currents, marked by the dashed lines, are of SN type everywhere.

3.2.4 Variation of the Laser Current

After discussing the features of the phase diagram in the (I_p, I_a) plane for $I_d = 45$ mA, Fig. 3.4, the laser current I_d was changed systematically. The first objective was to search for the value of I_d where multistability starts and vanishes, as it had not been observed in various previous experiments using higher laser currents. Second, the possible coexistence of four or more stable states was to be confirmed or excluded for our device. Exploratory scans using laser currents of $I_d = 70$ mA and $I_d = 90$ mA showed no tristability. To determine the upper and lower bound with respect to I_d, the borders of one selected tristable region in Fig. 3.4 have been tracked while changing I_d.

The results are shown in Fig. 3.7. I_d was systematically increased from 43 mA, just above the threshold value $I_d = 42.5$ mA, in one mA steps. The location of the island

changes slightly with increasing laser current, because the increasing intensity of the laser emission changes the carrier density in the feedback cavity. Starting at $I_d = 43$ mA, the tristable area in Fig. 3.7 first grows with increasing I_d. This initial growth of the mode overlap with an increase of I_d can be understood to result from the rising carrier density in the laser, it will be discussed in detail shortly. The tristable island reaches its maximum size at $I_d \approx 46$ mA, shaded green in Fig. 3.7. The corresponding overlap of the individual branches of output power is not yet sufficiently large to allow for the simultaneous coexistence of four states. A maximum of three coexisting cw states is achievable in the investigated regime.

Further increasing the laser current the size of the tristable region shrinks again, which can be understood as follows. In the phase diagram Fig. 3.4, the jump to the next mode at the MB line occurs well before the jump which would be expected from an extrapolation of the SN line. With increasing distance from threshold the MB instability occurs earlier within a feedback phase period. This can be seen clearly in Fig. 4.3 of the following chapter, on page 58. Therefore, the mode overlap is reduced and the tristable regions shrink. Of the two types of oscillatory instabilities that are observed for cw states in our device, only the mode-beating oscillations limit the multistability. Relaxation oscillations are strongly damped near threshold. For values above $I_d \approx 50$ mA, the tristable islands vanish completely. We therefore can conclude that the multistablity not only requires certain values of feedback phase and feedback strength, but also appears in a finite interval of I_d just above the lasing threshold.

3.3 Theoretical Interpretation

The dynamics of our experimental device are captured comprehensively by a traveling wave (T-W) model [32]. The corresponding numerical simulations spatially resolve the multisection device, allow for a very good qualitative agreement of simulation and experiment, and are accessible to numerical bifurcation analysis [90, 25]. While the T-W model is a valuable tool for the search for desired dynamical scenarios, the wealth of parameters may obscure the physical mechanisms behind the observed phenomena, making it hard to distinguish between generic and device-specific effects.

For long external feedback cavities and low feedback levels, experimental findings using delayed optical feedback are often successfully described in terms of the simpler Lang-Kobayashi (L-K) model [57]. Even for complex dynamics in the short cavity regime, the L-K equations are known to yield a good description [62], as long as the validity of the various approximations used is carefully considered. In our experiment we use a device with an ultrashort feedback cavity and potentially high feedback due to the amplifier section. The resulting device dynamics observed in experiments are usually far to complex to be captured by the L-K model. However, in the multistable regime seen in our experiments, far simpler continuous wave states are observed within the overwhelming majority of the phase diagram. A numerical comparison between the T-W and L-K models for such cw states has been conducted in Ref. [32]. It was found that for selected dynamical aspects and up to moderate levels of feedback, the descriptions

by both models agree qualitatively. For low feedback levels, the agreement even is quantitative. In the following we will see that the delay differential equations of the L-K model are sufficiently complex to explain the observations made in our experiments.

3.3.1 The Lang-Kobayashi Model

The Lang-Kobayashi equations [57] are an exceptionally thoroughly analyzed model system. In the following, I will summarize the relevant mathematical results from the viewpoint of mulstistability. The model consists of two coupled rate equations:

$$\frac{d}{dt}E(t) = (1+i\alpha)N(t)E(t) + \kappa E(t-\tau)e^{-i\varphi} \tag{3.1a}$$

$$\frac{d}{dt}N(t) = \frac{1}{T}\left(P - N(t) - (1+2N(t))|E(t)|^2\right) \tag{3.1b}$$

The first describes the time evolution of a slowly varying optical amplitude $E(t)$ in the laser, the second the change in the number of electron-hole pairs $N(t)$ with time. They are the rate equations (2.3) presented on page 12, save an addition to the equation for $E(t)$.

The new term proportional to $E(t-\tau)$ describes the optical feedback. It represents the re-injected optical field after one round trip in the external cavity, a simplification valid for low feedback strengths. All times are given in units of the photon lifetime τ_p. The time delay τ significantly complicates the equations. The space of solutions is now infinite-dimensional because initial conditions on the interval $t = [-\tau, 0]$ have to be provided. However, discrete solutions to the L-K equations still exist. In our experimental device, the time the optical field needs to traverse the feedback cavity of length L back and forth once is $\tau = 2Ln_\mathrm{g}(\omega_0)/c$. n_g represents the group refractive index of the material[4], $\omega_0 = 2\pi c/\lambda_0$ the frequency of the solitary laser and λ_0 the lasing wavelength. The phase of the delayed optical field $E(t-\tau)$ after this round trip is shifted by an amount equal to

$$\varphi = \omega_0\tau = 2\pi n_\mathrm{p}(\omega_0)\cdot\frac{2L}{\lambda_0} \tag{3.2}$$

with respect to $E(t)$, with the phase refractive index n_p. Fig. 2.3 of the previous chapter on page 14 shows a simplified sketch of such a delayed feedback setup. τ is adjusted by changing the injection level of the semiconductor material in the passive and amplifier sections, thereby altering $n_\mathrm{eff} = n_g := n_p$. Ln_eff is the optical path length of the feedback section, measured from the DFB section facet facing the feedback cavity to the external facet of the amplifier section. Changing τ, the solutions of the equations (3.1) change. When φ completes a full cycle from zero to 2π, the initial state is reached again. For a feedback cavity with $L \approx 800\ \mu$m, $\lambda_0 \approx 1.5\ \mu$m and $n_\mathrm{eff} \approx 3$, φ is in the order of 10^4. Tiny

[4]The group refractive index n_g of the slow optical amplitude $E(t)$ and the phase refractive index belonging to the fast optical oscillation with ω_0 generally differ in dispersive media. In the following, I will assume that the difference is negligible and do not distinguish between both.

changes of n_{eff} already correspond to a large number of such mathematically equivalent feedback phase periods. φ therefore will be a key parameter in the following discussion. The coefficient κ will used to characterize the feedback strength. P in equations (3.1) is equal to $P = \frac{(I_d - I_{\text{th}})}{2(I_{\text{th}} - I_t)}$, see page 12. I_d is the laser pump current $I_d = IV$, which is rescaled with respect to threshold current $I_{\text{th}} \approx 42.5$ mA and transparency current [66] $I_t \approx 5$ mA of the solitary laser. $P = 0$ marks the lasing threshold without feedback. As introduced in equation (2.2) on page 12, the material parameter α describes the nonlinear amplitude-phase coupling of the light passing through the semiconductor material. T is the ratio of the average time an electron-hole pair exists (some nanoseconds) to how long a photon spends on average in the cavity (some picoseconds). At $T \approx 10^{-3}$, there is a clear separation of the internal timescales; and the smallness of T has to be carefully considered when taking various limits.

The L-K equations obviously do not include any spatially resolved details of the laser and cavity; only one longitudinal optical mode is considered. Few parameters enter the equations: α, T and P characterize the laser, while κ and φ characterize the optical feedback. We will apply the extended bifurcation analysis presented in [91, 75, 74] to the L-K equations, using realistic parameters for our experimental device. The predictions made will be validated by direct comparison with experimental data.

3.3.2 Stationary States

For the further analysis, real and imaginary part of the complex valued $E(t)$ are separated by setting $E(t) = R(t)e^{i\Phi(t)}$, with the optical phase Φ. The L-K equations are invariant under changes of Φ. We end up with the following equation system:

$$\frac{d}{dt}R(t) = N(t)R(t) + \kappa R(t-\tau)\cos\left(\varphi - \Phi(t-\tau) + \Phi(t)\right) \tag{3.3a}$$

$$\frac{d}{dt}\Phi(t) = \alpha N(t) + \kappa\frac{R(t-\tau)}{R(t)}\sin\left(\Phi(t-\tau) - \Phi(t) - \varphi\right) \tag{3.3b}$$

$$T\frac{dN}{dt} = P - N(t) - (1 + 2N(t))R(t)^2. \tag{3.3c}$$

In our experiments, the laser output is continuous wave besides small regions with mode-beating pulsations just before a mode jump. Therefore we now look for solutions with constant carrier inversion $N(t) = N_s$ and intensity R_s. To achieve this in equations (3.3), the term $\cos\left(\varphi - \Phi(t-\tau) + \Phi(t)\right)$ in (3.3a) has to be a constant. Therefore both the difference $\Phi(t-\tau) - \Phi(t)$ and the sin in (3.3b) are also constant. Equation (3.3b) then reduces to $\frac{d}{dt}\Phi(t) = \text{const} = \omega$, leading to the ansatz $E(t) := R_s e^{i\omega t}$. Inserting this ansatz back into equations (3.3), we get

$$0 = N_s R_s + \kappa R_s \cos\left(\omega\tau + \varphi\right) \tag{3.4a}$$

$$N_s = \frac{1}{\alpha}(\omega + \kappa\sin\left(\omega\tau + \varphi\right)) \tag{3.4b}$$

$$0 = P - N_s - (1 + 2N_s)R_s^2. \tag{3.4c}$$

A solution of these equations is in fact a periodic orbit in (E, N). If we were to use a rotating reference frame, they would indeed correspond to a fixed point in phase space. We will refer to these as *stationary states*, because they have a constant field amplitude and fixed optical frequency. These stationary states are the simplest possible solutions of the L-K equations. In physical terms, the laser emits at one fixed optical frequency with constant intensity.

We additionally demand that $R_s > 0$, which is the physical condition for the laser to be "on". Substituting N_s in (3.4b) using (3.4a), and assuming that $N_s \neq -\frac{1}{2}$ in (3.4c) leads to:

$$N_s = -\kappa \cos(\omega\tau + \varphi) \tag{3.5a}$$

$$\omega = -\kappa(\alpha \cos(\omega\tau + \varphi) + \sin(\omega\tau + \varphi)) \tag{3.5b}$$

$$R_s^2 = \frac{P - N_s}{1 + 2N_s}. \tag{3.5c}$$

$R_s^2 > 0$ should be larger than zero, therefore the carrier density N_s is restricted to values within $-\frac{1}{2} < N_s \leq P$ for $P > -\frac{1}{2}$. Finally, we rewrite equation (3.5b) as

$$\omega\tau = -C \sin(\omega\tau + \varphi + \arctan\alpha). \tag{3.6}$$

We have used that a linear combination of sin and cos with the same argument can be expressed as a sin with an appropriately changed phase. We also introduced an "effective feedback strength" $C := \kappa\tau\sqrt{\alpha^2 + 1}$. C is related to device parameters by an additional scale factor, which depends on laser properties and is explicitly given for Fabry-Perot (FP) and distributed feedback (DFB) lasers in references [57] and [92], respectively. The choice of C is motivated by the fact that above $C = 1$, multiple solutions to the transcendental equations (3.4a) and (3.4b) are possible. This is often used to distinguish between "low" and "high" feedback regimes, and will be discussed in the following.

3.3.3 External Cavity Modes

Solutions to the transcendental equations (3.4a) and (3.4b) correspond to the external cavity modes (ECMs) of the laser. Specifying the parameters $\{\kappa, \tau, \alpha, \varphi\}$, they can be graphically or numerically determined. In the following, we set $\alpha = 6$ and $\tau = 20$. These are the approximate experimental parameters for the linewidth enhancement factor (see Fig. 3.16 on page 50) and τ rescaled by a photon lifetime of $\tau_p = 1$ps, respectively.

Fig. 3.8 shows the possible solutions of equations (3.4a) and (3.4b) for two combinations of C and φ in the (N_s, ω) plane. The intersections of the graphs of both equations lie on an ellipse drawn orange, given in parametric form by $N_s^2 + (\omega - \alpha N_s)^2 = \kappa^2$ [75]. A stability analysis shows that ECMs above the dashed saddle-node (SN) line, given by $S = \frac{1+\tau\alpha\omega}{\tau(\alpha^2+1)}$, are unstable [75]. They are called antimodes and are marked by orange hollow points. Red dots belonging to stable ECMs lie below this diagonal line. These stable solutions can be destabilized by various types of bifurcations [56, 75]. For $C = 4$ and $\varphi = \pi$ we have a total of three modes of which at most 2 are stable, see Fig. 3.8 (b).

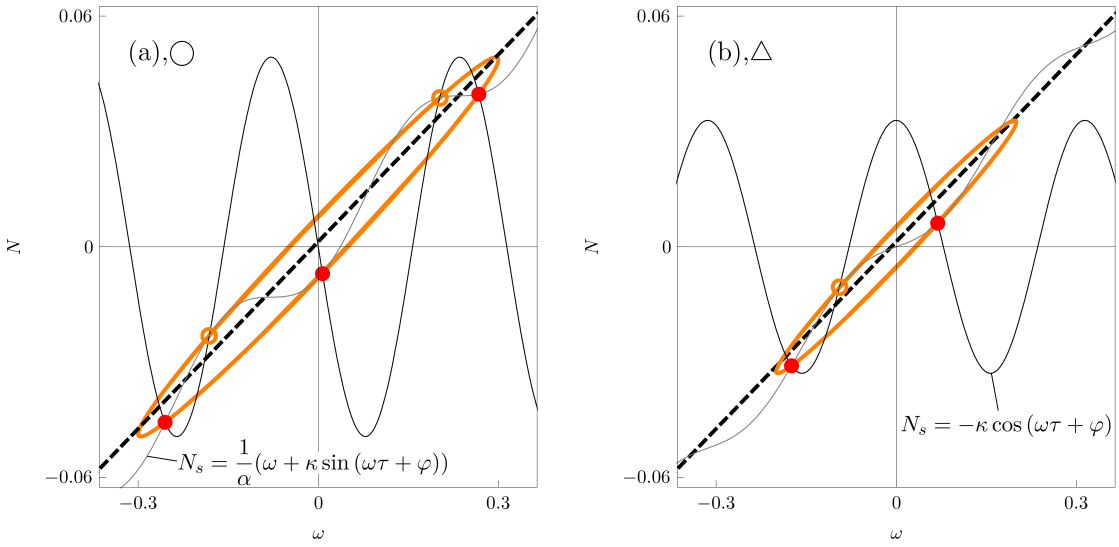

Figure 3.8: Lang-Kobayashi model, $\alpha = 6$ and $\tau = 20$. Graphical solution of equations (3.4b), thin gray line, and (3.5a), thin black line. The mode of the solitary laser would be at (ω=0, N=0). Solutions lie on an ellipse drawn orange. Diagonal dashed line, SN line. ECMs above SN line: antimodes, orange hollow dots. Below: modes, red dots. Note that neither (a) nor (b) depend on the distance from threshold P. The number of physically relevant modes may be lower than the number of stable modes, see Fig. 3.11. (a) $\varphi = -\frac{\pi}{2}$, $C = 6$ ($\kappa = 0.049$). 3 modes, 2 antimodes. (b) $\varphi = \pi$, $C = 4$ ($\kappa = 0.033$). 2 modes, 1 antimode.

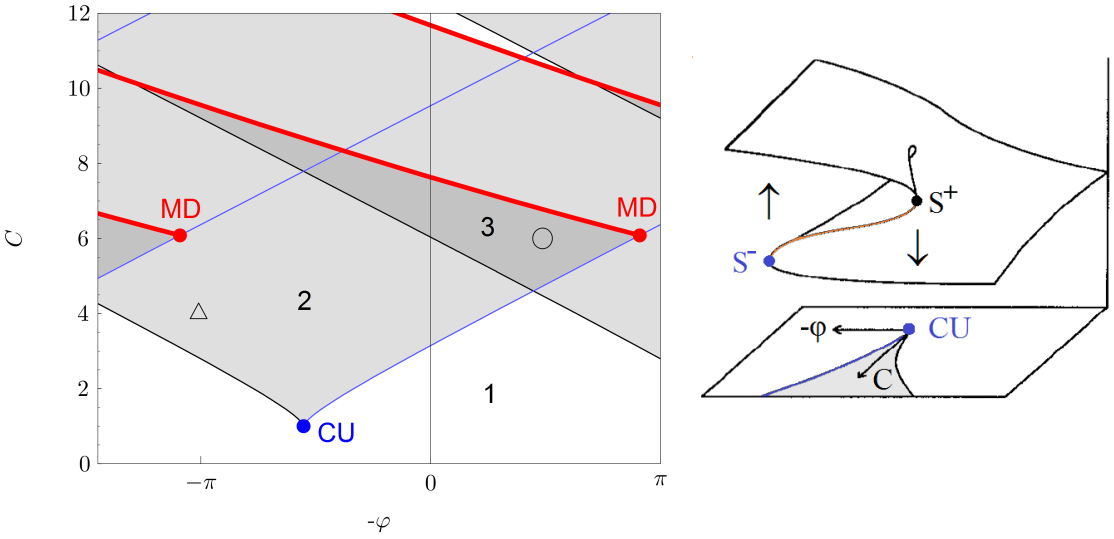

Figure 3.9: Lang-Kobayashi model, $\alpha = 6$ and $\tau = 20$. Bifurcation diagram in the plane of feedback phase $-\varphi$ and feedback strength $C = \kappa\tau\sqrt{\alpha^2+1}$, 2π-periodic in φ. Blue (black) line, SN line S^- (S^+), equation (3.7). Crossing this line in the direction of increasing (decreasing) $-\varphi$, two ECMs are created in a saddle-node (SN) bifurcation. Numbers, number of experimentally observable stable lasing solutions, additionally indicated by different shades of gray. See also text. Red thick line, Tager-Petermann (T-P) line, equation (3.8). MD, mode degeneracy point on S^-. CU, cusp formed by $S^\pm$ at $C = 1$. ◯, see Fig. 3.8 (a). △, see Fig. 3.8 (b). Sketch on the right: Formation of a fold, figure adapted from Ref. [54]. See Fig. 3.5 for corresponding experimental data.

Increasing the feedback strength to $C = 6$ and changing the feedback phase to $\varphi = -\frac{\pi}{2}$, there are three stable modes and two antimodes, as indicated in Fig. 3.8 (a).

When increasing the feedback phase φ for a fixed C in Fig. 3.8 (a,b), a pair of a mode and an antimode is born in a saddle-node bifurcation where SN line and ellipse intersect. Further increasing φ, both then wander upwards on the ellipse, corresponding to an increasing carrier inversion N and ω. At the second intersection of ellipse and SN line, a mode and an antimode annihilate each other in a second saddle-node bifurcation. The laser then jumps to the stable mode with the highest phase stability [93].

3.3.4 Folding of Modes

The bifurcation diagram in the plane of the parameters (φ, C) is shown in Fig. 3.9. The location of the solutions shown in Fig. 3.8 is indicated by ◯ for Fig. 3.8(a) and △ for Fig. 3.8(b). In the experiments, the feedback phase φ decreases with increasing phase current I_p. Therefore, we plot negative phases $-\varphi$ to facilitate the comparison with

experimental data. While the phase diagram is 2π-periodic in φ, for clarity more than one period is shown.

For $C < 1$, only one mode is possible for all values of φ. At $C = 1$, a cusp marked as CU is formed by the saddle-node curves $S^{\pm}$. These curves mark where a mode-antimode pair is created or annihilated in a saddle-node bifurcation, as discussed above. They are given by the equations

$$S^{\pm}(C) = \pm(\sqrt{C^2 - 1} + \arccos(-\frac{1}{C})) - \arctan(\alpha) + 2n\pi, \tag{3.7}$$

for integer n [75]. Increasing the feedback strength so that $C > 1$, a fold is formed and hysteresis effects occur when tuning the feedback phase $-\varphi$ forward and backward in Fig. 3.9. If no other restrictions apply, crossing S^{-} (blue line) in the direction of decreasing $-\varphi$ or passing S^{+} (black line) in the direction of increasing $-\varphi$, one unstable and one possibly stable mode are created. The experimental data showing the formation of a fold was discussed in Fig. 3.5 on page 31. There, the discontinuous jumps reveal the position of a saddle-node bifurcation. An unstable state exists e.g. in the yellow hysteresis region, connecting the low and the high power branches. For $C > 1$, the bifurcation diagram Fig. 3.9 represents the projection of a complicated folded structure onto the parameter plane spanned by φ and C. The right panel of Fig. 3.9 shows a three-dimensional sketch of this fold structure.

This folding of modes is the mechanism leading to multistability in the L-K model. Increasing the feedback strength, the overlap of the fold and the number of coexisting states within a feedback phase period grows. However, there are two oscillatory instabilities in our device which potentially limit the maximum number of coexisting modes. Transitions between modes due to both RO and MB instabilities are observed at higher laser currents, reducing the size of the regions with hysteresis, see e.g. Fig. 4.3 on page 58 for the experimental situation at another point of operation. Near threshold, as discussed here, relaxation oscillations are strongly damped. Mode-beating oscillations, however, are observed in experiment. In our ultrashort-cavity case with the laser biased only slightly above threshold, a mode becomes unstable only by a Hopf bifurcation due to the existence of an antimode with the same threshold gain [91, 65, 18].

3.3.5 Mode Beating Phenomena

The limitation of the maximum degree of multistability associated with MB is captured by the L-K model. As can be deduced from Fig. 3.8 (a), a mode and an antimode may have the same carrier inversion $N = N_1 = N_2$. The red thick Tager-Petermann (T-P) line [91] marks where the conditions $N_1 = N_2$ and $\omega_1 \neq \omega_2$ are fulfilled for two ECMs on the (φ, C) plane in Fig. 3.9. It is given in parametric form, depending on ω, by the coordinates [91]

$$(\varphi, C) = (\pi - \alpha\omega\cot\omega, \frac{\omega\sqrt{1+\alpha^2}}{\sin\omega}). \tag{3.8}$$

The location of the T-P line with respect to the $S^{\pm}$ lines sensitively depends on α. When approaching T-P, beating phenomena of the two ECM can be expected to be observed [29] and the stable mode is increasingly destabilized. Following the T-P line towards the mode degeneracy point MD on the S^{-} line, the beat frequency $\omega_2 - \omega_1$ and therefore the difference between both ECM solutions themselves goes to zero. In the experimental phase diagram in Fig. 3.4 this instability is labeled MB, because it is accompanied by a characteristic intensity pulsation visible in the power spectrum. Mode-beating phenomena are observed only close before the mode jump when close to the lasing threshold. This is in contrast to the case of high laser currents, where they span almost all of a feedback phase period. The experimental differences corresponding to passing the $S^{\pm}$ and T-P lines of the L-K model can be seen in the optical spectra of Fig. 3.6 (a) and (b) on page 32.

The instability associated with the mode-beating limits the degree of multistability which ultimately can be reached in experiment by an increase of the feedback strength C. Above the T-P line, additionally to the mode with highest gain and lowest power now also the corresponding antimode is fully undamped [64]. This situation is unstable and the laser returns to another stable mode with lower carrier density and same relative feedback phase. The point of mode degeneracy MD lies at $C = \sqrt{1+\alpha^2}$ [91], and latter value of C realizes the biggest possible domain of tristability. The value of C at MD also marks the transition between the two possible ECM instabilities of relaxation oscillation and mode-beating type, observed in the L-K model for higher laser currents near MD [91]. Increasing the value of α, the instability marked by the T-P line moves to higher values of C and the domain of tristability is limited by SN bifurcations only. The number of possible stable ECMs is indicated in Fig. 3.9, areas with the same number of experimentally observable coexisting ECMs also have the same gray shading.

3.3.6 Physically Relevant Modes near Threshold

In the experiment, multistability occurs for laser currents closely above the threshold value. As is well known, threshold lowering can be the result of constructive interference of the optical field due to the coherent feedback. Destructive feedback may have the opposite effect: the laser may be off, even when it is pumped above the threshold of the solitary laser. In our experiment, the laser is almost off in the lowest branches of the tristable regions in Fig. 3.15, indicating that the distance from threshold is a relevant parameter. I will therefore now detail the theoretical dependence of the multistability in the L-K model on the distance from the lasing threshold.

The condition $R_s > 0$ for the amplitude of the cw emission implies a limitation for the number of modes we can observe in experiment. Some solutions of the L-K model, while mathematically permitted, do not correspond to parameters of physically possible ECMs. For example, one of the stable lasing states might be replaced by the stable "off" state.

This situation is illustrated by figure 3.10 (a) and (b). Panel (a) shows the (C,φ) plane for $P = 0.001$ just above, (b) for $P = -0.001$ just below threshold. When including the distance from threshold P as a parameter, a new bifurcation appears [75]. Orange curves

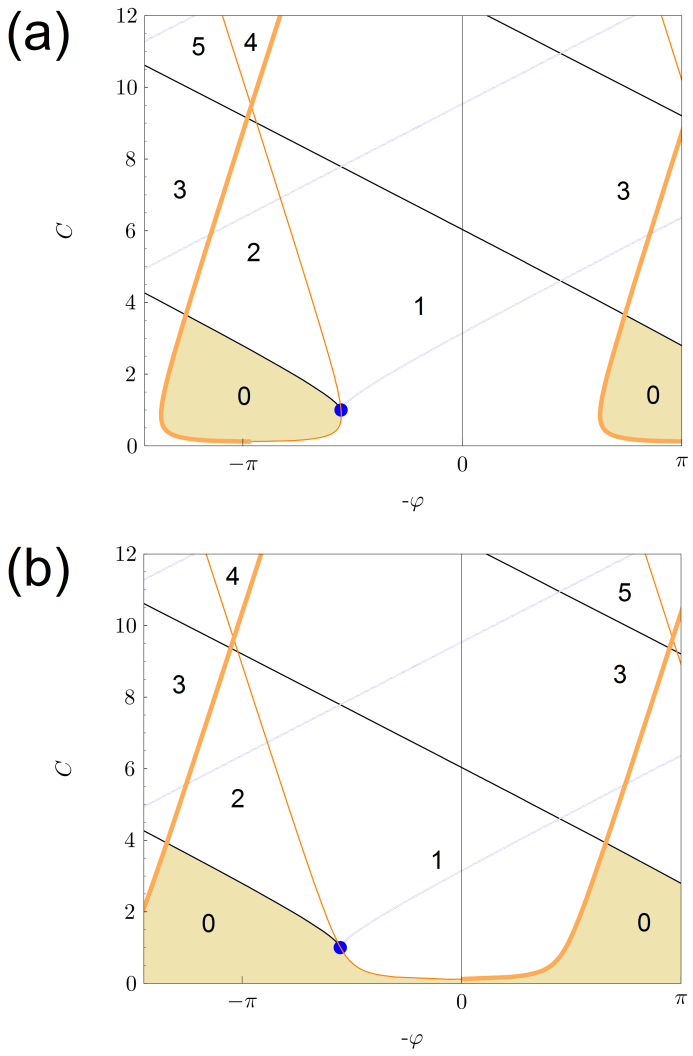

Figure 3.10: Bifurcation diagram of the Lang-Kobayashi model very close above and below the lasing threshold, $\alpha = 6$ and $\tau = 20$. Numbers, number of coexisting stable *and* unstable lasing solutions. In regions shaded dark yellow and marked "0", the laser is switched off. Black line, SN line S^+, equation (3.7). The mode pairs created when crossing S^- (only outline shown) are not physical, see text for details. $S^\pm$ do not depend on P. Thin (thick) orange curve, Hopf curve H^- (H^+), equation (3.9). (a) $P = 0.001$. (b) $P = -0.001$. Minimal anti-phase feedback may turn the laser off just above threshold, constructive in-phase feedback may switch the laser on just below the lasing threshold.

mark where the basic solution $(E, N) = (0, P)$, which exists for all choices of the other parameters, changes its stability in a Hopf bifurcation. This solution is stable when the laser is "off" and unstable when the laser is "on". The curves therefore correspond to the laser threshold of a mode when the laser is subject to feedback. $H^{\pm}$ are given in parametric form by

$$(\varphi, C) = \Big(\pm \arccos(-\frac{P\tau\sqrt{\alpha^2+1}}{C}) \pm \sqrt{\frac{C^2}{(\alpha^2+1)} + P^2\tau^2} - \alpha\tau P + 2n\pi, C\Big), \qquad (3.9)$$

for integer n [75]. $H^{\pm}$ depend on the distance from threshold P. For $P = 0.001$ close above threshold, minimal destructive anti-phase feedback ($\varphi \approx n\pi$) may lead to no available lasing mode in Fig. 3.10 (a). Conversely, constructive feedback around multiples of $2\pi\varphi$ can induce lasing just below threshold. This can be seen in Fig. 3.10 (b) for $P = -0.001$. Depending on where the loop formed by $H^{\pm}$ is crossed, the specific solution which is exchanged in favor of the "off" state, either a stable/unstable mode or an unstable antimode, is different [75]. The Hopf curve is tangent to the saddle-node curve S^- at one point. Above this point on S^-, i.e. increasing C, the two lowest-in-power ECMs which are created when crossing S^- are not physically relevant. For both of them $N_s > P$ holds, and the carrier inversion would have to be higher than the pump current can provide [75]. As this tangency coincides with the cusp point in Fig. 3.10, the whole S^- bifurcation is unphysical and the corresponding line only sketched.

I will now detail how a change of P, using parameters comparable with the experiment, influences the phase diagram in Fig. 3.9. In Fig. 3.11 P is varied from 0.03 (a) to 0.06 (d). This corresponds to laser currents just above threshold similar to the ones used in experiment. For (a) and (b), the relation $0 < P < \frac{1}{\tau}$ holds. The off-state is stable in a small region enclosed by a loop formed by the Hopf curves (3.9) for $C > 0$. The number of coexisting ECMs is reduced by one in this region. Depending on where $H^{\pm}$ is crossed, the number of stable lasing solutions which can be accessed in experiments may be reduced by one. Above the point where the loop of $H^{\pm}$ is tangent to S^-, the ECM pair created by S^- is not physical. S^- is plotted in a lighter shade of blue from there on. The self-intersection of $H^{\pm}$ for $P < \frac{1}{\tau}$ lies on the T-P curve. The Hopf bifurcations associated with the T-P line and $H^{\pm}$ are degenerate and form a codimension-two point[5]. The two ECMs which change in stability in this point have identical carrier inversions N, but distinct optical frequencies $\omega_1 \neq \omega_2$. Increasing the pump current towards $P = 0.05$, Fig. 3.11 (c), this codimension-two point wanders along the T-P line, until it finally coincides with the mode degeneracy point MD. At $P = \frac{1}{\tau} = 0.05$, the Hopf curves $H^{\pm}$ form a cusp and both stability exchanges happen exactly at MD. Here at the mode degeneracy point, for the two involved modes now also $\omega_1 = \omega_2 = \omega$ holds - they are identical. The MD point can be identified as a codimension three bifurcation point in the bifurcation diagram, i.e., the three parameters P, φ and C have to be set to the correct values to observe it. The value of C associated with MD is the maximum value for which

[5] Higher codimension bifurcations and bifurcation points are difficult to observe in experiments, as several parameters have to be controlled sufficiently well at the same time.

a stable off-state can exist. Increasing P further, the T-P line with the associated MB instability already limits the number of coexisting stable ECMs. In (d), the off state enclosed by the Hopf-curves is unstable.

To illustrate the results which the complex bifurcation diagrams in the $\{\varphi, C\}$-plane represent, we will vary φ along two exemplary cuts along the green lines in Fig. 3.11 (a) and (c). For both we fix the feedback strength to $C = 6.08$, crossing MD in (c). We will follow the stable states which can be traversed in experiment. We choose to characterize the stable steady states by the average output power emitted by the laser. Every observable ECM is unambiguously associated with a certain average output power in experiment, see Fig. 3.3 discussed previously, showing the output power and center wavelength variation when tuning I_p. The theoretical results will now be directly compared to experimental data.

3.4 Comparing Experiment and L-K Model

3.4.1 Threshold Dependence of the Multistability

In Fig. 3.12 (a) and (c), the schematic output power variation along the green lines in Fig. 3.11 (a) and (c), respectively, is shown. To unfold the 2π-periodic phase diagram, both panels show more than two and a half complete 2π cycles of φ. For the chosen value of $C = 6.08$, the individual branches span more than two full periods of the feedback phase φ. Three tristable regions, shaded dark gray, can be observed. By including the distance from threshold P we keep track, whether the carrier inversion necessary for a theoretically possible lasing mode can actually be provided by the pump, or not. We also explicitly determine where the output power of a lasing mode is zero in Fig. 3.12 (a,c). When approaching the region enclosed by the Hopf curves $H^{\pm}$ in the phase diagram of Fig. 3.11 (a), the power in the lowest stable branch of Fig. 3.12 (a) has to go to zero, as it is exchanging its stability with the off-state on H^{+}. After passing H^{+}, the laser is in the stable off-state, represented by an orange line at zero emission power. We now have tristability of two cw states and the off-state. In the hatched regions of Fig. 3.12 (a) and (c), the condition $R_s < 0$ holds. While the lowest power branch regains the stability after leaving the loop formed by $H^{\pm}$ in Fig. 3.11 (a), the associated output power is negative and the stable continuation of the lowest branch is therefore not physical. This can also be seen in Fig. 3.11 (a), where the bifurcation S^{-} is not creating physically relevant ECMs anymore for the chosen value of C. When further increasing $-\varphi$, the off-state is exchanged with an unstable lasing mode and from there the laser immediately jumps to another available stable lasing branch. In experiments, this typically is the middle one.

The size of the tristable regions is significantly larger in Fig. 3.12 (c). Increasing the distance from threshold to $P \approx 0.05$ in (c), the line of zero emission power moves down relative to the ECM branches. In the φ, C plane shown in Fig. 3.11, the loop formed by $H^{\pm}$ shrinks and moves upward, until a cusp is formed at the MD point. C is chosen so that the crossing of the zero power line with the ECM branches happens exactly at MD in Fig. 3.12 (c). The whole lowest branch is stable and physical, extending the region of tristability to maximal width. When moving further away from threshold by increasing

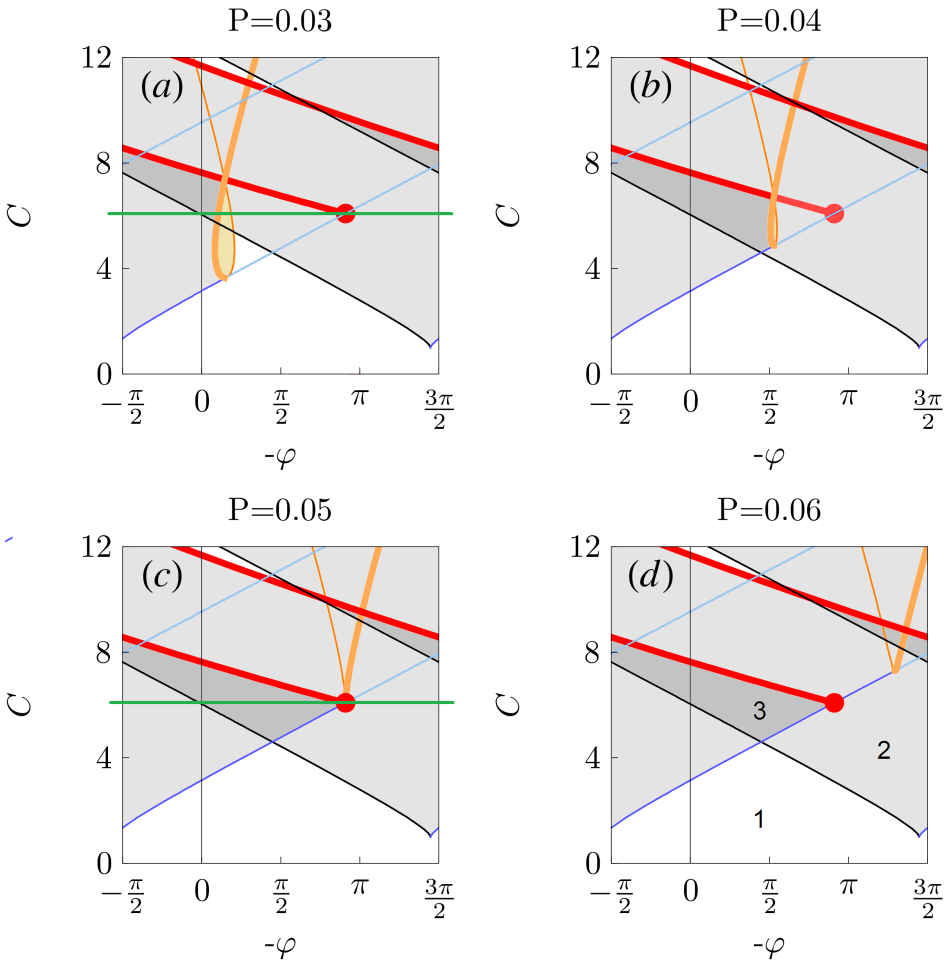

Figure 3.11: Bifurcation diagram for $\alpha = 6$ and $\tau = 20$, see also Fig. (3.9). The distance from threshold P is varied from 0.03 (a) to 0.06 (d) to cover a range similar to the experimental conditions, where $P \approx 0.03$ for $I_d = 45$ mA. Thin (thick) orange curve, Hopf-curve H^- (H^+), equation (3.9). Blue/light blue (black) lines, saddle node (SN) line S^- (S^+), equation (3.7). Red thick line, Tager-Petermann (T-P) line, given by (3.8). Red dot, mode degeneracy point MD. Shades of gray and numbers in (d), number of coexisting stable lasing states. (a,b) $P < \frac{1}{\tau}$. The self-intersection of $H^\pm$ is on the T-P curve, forming a codimension-two point. Within the loop formed by $H^\pm$, one of the possible lasing modes is not physically relevant and the off-state of the laser is stable instead. In other regions enclosed by $H^\pm$, an unstable lasing state is replaced by the unstable off state. (c) $H^\pm$ change qualitatively at $P = \frac{1}{\tau}$, for $\tau = 20$ at $P = 0.05$. MD, T-P and a cusp formed by $H^\pm$ coincide in a codimension three bifurcation point. (d) For $P > 0.05$, $H^\pm$ enclose an unstable off-state. The green line in (a) and (c) indicates the location of the cut expanded in Fig. 3.12 (a) and (c), respectively.

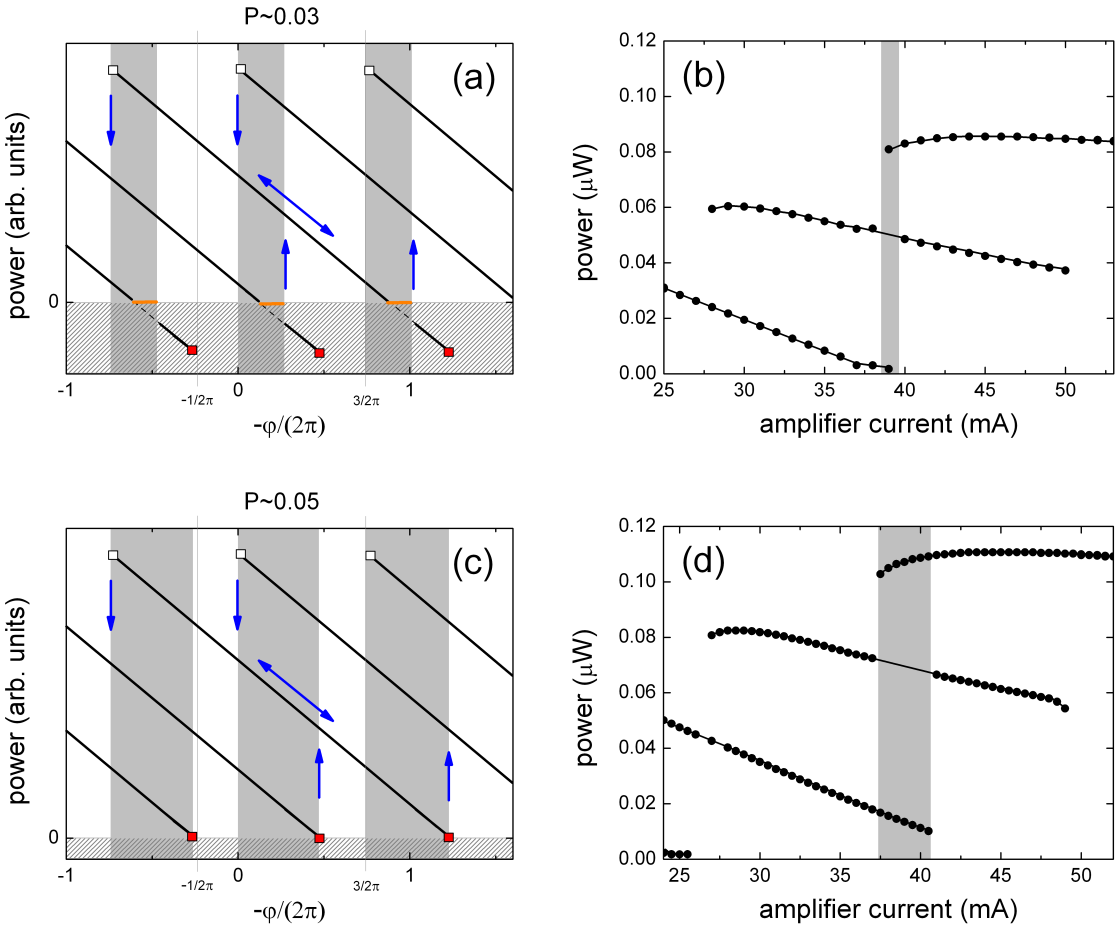

Figure 3.12: Schematic sketch of the output power variation of stable states along the green cut lines in Fig. 3.11 and comparison with experimental data. Regions of tristability are shaded gray. (a),(c): Schematic of the theoretical output power variation. Hatched region, output power smaller than zero. Stable ECMs in this region are not physical. Blue arrows, power jumps during a typical hysteresis cycle. Squares, SN bifurcation points. Squares filled red, MD point. (a), $P \approx 0.03$. Orange line, stable off-state. Two different types of tristability are observed, either 3 cw states, or 2 cw states and the stable off state. (c), $P \approx 0.05$. The off state is stable only in the MD point, the width of the tristable region is maximal. (b),(d): Average power of AFL emission when increasing and decreasing the amplifier current. $I_p = 76$ mA. (b), $I_d = 43$ mA. The laser is effectively off in a part of the lowest branch. (d), $I_d = 45$ mA.

P, the maximum width of the tristable region will be unaffected by $H^{\pm}$. This can be seen when comparing (c) to (a) and (d), or alternatively when looking at the systematic movement of $H^{\pm}$ to higher values of C in Fig. 3.11(a-d).

Experimental data for two different laser currents is shown in panels (b) and (d) of Fig. 3.12. For (b), the laser current is set to $I_d = 43$ mA, just above the threshold of the solitary laser ($I_d = 42.5$ mA), the phase current to $I_p = 76$ mA. The amplifier current is increased from zero to 100 mA and decreased back to zero mA, while the average output power is recorded. As the feedback phase is changed by changing the refractive index of the amplifier section here, the increasing amplification leads to an upward shift of successive branches. The traversal mode leaves a characteristic gap on the middle branch, directly indicating the width of the tristable regions. Like in Fig. 3.3, the middle branch extends over more than two periods of the feedback phase. As discussed previously in the context of Fig. 3.3, the different periods of the feedback phase are not equivalent in experiment. Only one region of tristability is passed. In the lowest branch of Fig. 3.12 (b), the laser is effectively off just below $I_a = 40$ mA. Increasing the amplifier current, a jump to the middle branch is observed. Increasing the laser current to $I_d = 45$ mA in Fig. 3.12 (d), all branches are shifted upwards in power and to slightly lower amplifier currents. The starting value of the x-axis (d) has been shifted to compensate for this offset. The length of the middle branch is the same in both (c) and (d). The width of the tristable region in (d) is significantly increased and the lowest power branch does not reach zero.

The data in Fig. 3.12 demonstrates two effects the proximity of the laser threshold may have on the multistability in the L-K model, which can indeed be observed experimentally. First, the regions of tristability are diminished because some solutions are not physical. Second, the tristability of three cw lasing states can be replaced by tristability of two stable lasing states and the stable *off*-state for appropriate feedback parameters. If we were to decrease the laser current even more, we would eventually expect only bistable behavior. Increasing P further, the T-P line with the associated mode-beating instability limits the number of coexisting stable ECMs. As detailed in the experimental part and e.g. visible in Fig. 4.3 on page 58, the tristable region shrinks again, because the MB instability develops increasingly early when increasing the laser current.

3.4.2 Comparing Experimental and Theoretical Phase Diagram

We are now able to compare the experimental phase diagram discussed earlier, shown again in Fig. 3.13(a), with the predictions of the L-K model in Fig. 3.13(b). Domains with multiple stable ECMs in the $(-\varphi, C)$ plane are drawn in panel (b) for $\alpha = 6$. Two ECMs are stable in the dotted (yellow) area. Three ECMs coexist in the blue domains where areas of neighboring phase periods overlap. Fig. 3.13(b) agrees well with the experimental findings of (a) when taking into consideration that the mapping between (I_p, I_a) and $(-\varphi, C)$ is not simply linear. The mapping causes some shearing and stretching of the picture but keeps the topological relations intact, in particular between the regions of tristability and the kinks where MB and SN lines touch each other. The bifurcations leading to the mode jumps with increasing and decreasing currents following

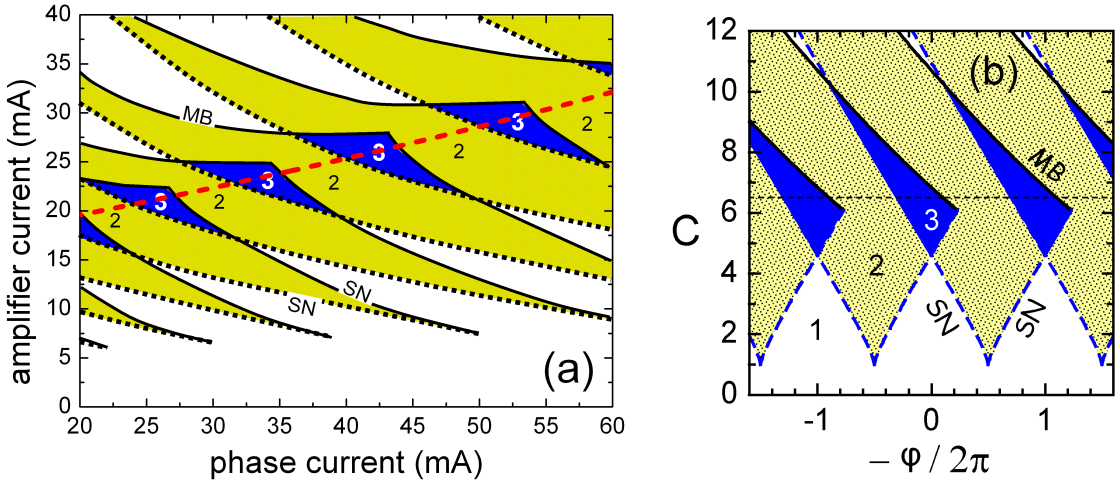

Figure 3.13: Comparison of experiment and Lang-Kobayashi model. (a) Domains of multistability in the (I_p,I_a) plane for $I_d = 45$ mA, see Fig. 3.3 (a). Dashed red line, cut shown in Fig. 3.14 (a). (b) Stationary states in the $(-\varphi, C)$ plane for $\alpha = 6$. Dashed (blue), SN bifurcation (of stable modes only). Solid, MB instability. Dotted (yellow) and dark gray (blue) regions: bistable and tristable domains, respectively. Thin dashed (black) line, cut shown in Fig. 3.14 (b).

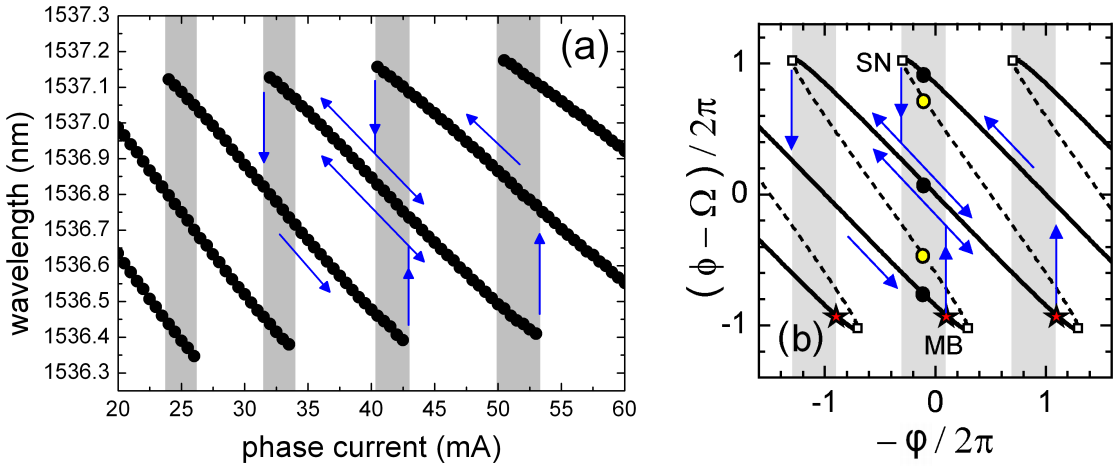

Figure 3.14: Comparison of experiment and Lang-Kobayashi model. Blue arrows, central hysteresis loops. Shaded grey, regions of tristability. (a) Possible lasing wavelengths along the dashed red line in Fig. 3.13 (a), black circles. See Fig. 3.15 (b) for the corresponding variation of optical power. (b) Cut along $C = 6.5$ in Fig. 3.13 (b), crossing SN and MB lines. Vertical and horizontal axes correspond to scaled wavelength shift and phase current, respectively. Squares, SN bifurcations. Circles, modes (full) and antimodes (empty). Asterisks, MB instability ($\alpha = 6$).

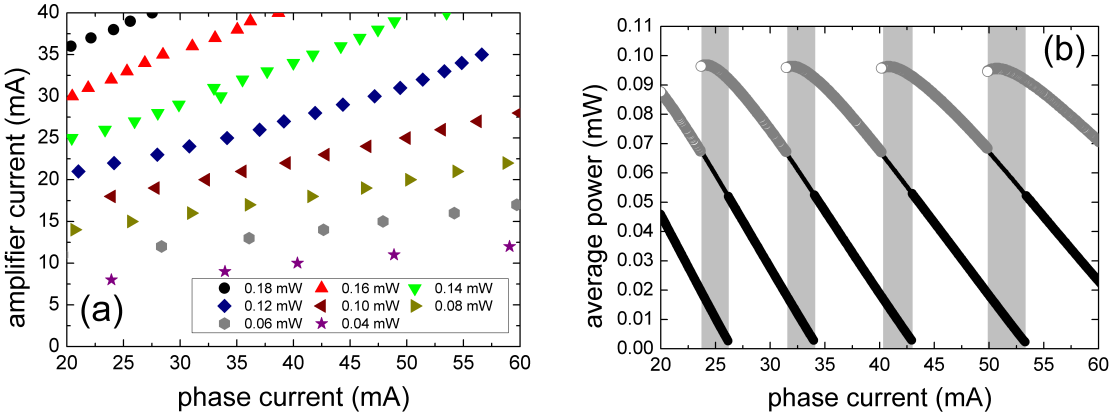

Figure 3.15: (a) Maximum output power when tuning the phase current for $I_d = 45$ mA, see also Fig. 3.4. (b) Variation of the output power when tuning (I_p, I_a) to follow a line with ≈0.1 mW maximum average power, marked by blue diamonds in (a) and the dashed red line in Fig. 3.13 (a). Shaded gray, regions of tristability. Big black (hollow gray) dots, increasing (decreasing) amplifier and phase currents. Small black dots, decreasing currents, starting in the middle branch. Note that the average power of the lowest branch is almost zero. For corresponding lasing wavelengths, see Fig.3.14 (a).

the L-K model have been experimentally verified earlier.

Fig. 3.14 (a) shows the corresponding variation of the center wavelength along the dashed red line of Fig. 3.13 (a). The three coexisting external cavity modes in the gray shaded regions of (a) have a wavelength separation of around 0.4 nm. Fig. 3.13 (b) shows the theoretical emission wavelengths when varying the feedback phase φ. One typical full hysteresis cycle is indicated for both experiment and theory in (a) and (b). In Fig. 3.14 (b), the jump from the lowest branch to the middle branch occurs already before the saddle-node bifurcation marked by the squares due to the MB instability (asterisks). The unstable branches connecting the stable branches are not visible in experiment. The difference between crossing the lines marked SN and MB in the experiment has been shown earlier for two selected examples, see Fig. 3.6 (b) and (c). Their location in the (I_a, I_p) plane is indicated by the markers in Fig. 3.4. The path of Fig. 3.14 (a) has been chosen to cross SN lines only, see Fig. 3.14 (b).

Fig. 3.15 investigates the shift of the tristable islands to higher values of I_a when increasing I_p in detail. In Fig. 3.15 (a), points with same maximum output power in the individual branches for tuning the phase current are plotted. The increased losses have to be compensated by increased amplification to achieve the same feedback strength. Lines connecting these points therefore correspond to lines of constant feedback strength. In Fig. 3.15 (b), the output power variation is measured along such a line of constant feedback strength. The currents of the feedback section are varied along the dashed red line in Fig. 3.4 which crosses the regions of tristability (shaded gray). The average power in the lowest branch is almost zero just before the jump to the next branch. All feedback

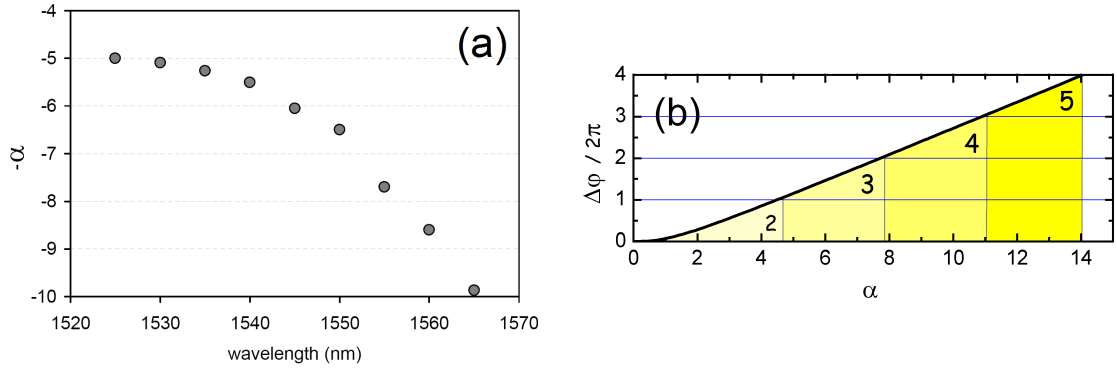

Figure 3.16: (a) Henry-factor α as determined by sub-threshold amplified spontaneous emission spectra, taken from [34]. A center wavelength of around 1537 nm corresponds to $\alpha \approx 5.5$.
(b) Maximum fold width $\Delta\varphi$ at $C = \sqrt{1+\alpha^2}$ versus α. Labels indicate the resulting maximum number of coexisting stable ECMs.

phase periods shown are now almost equivalent, as would be expected. The increasing width of a 2π variation in φ is a result of the non-monotonous refractive index change of the semiconductor material with increasing applied current.

3.4.3 Maximum Degree of Multistability

As I have shown, the maximum degree of multistability in the L-K model is determined by α and P. If we are sufficiently far above threshold, it is given by the number of modes at the MB-SN kink in Fig. 3.13(b). Using the coordinates of the mode degeneracy point given in Ref. [91], the maximum number of coexisting stable ECMs is

$$M = 2 + \mathrm{int}\left(\frac{\Delta\varphi}{2\pi}\right) \text{ , where } \Delta\varphi = 2[\alpha - \arctan\alpha]. \tag{3.10}$$

Fig. 3.16 (b) displays the maximal fold width $\Delta\varphi$ and the resulting M in dependence on α. We can expect tristability in the L-K model when α exceeds a value of 5. This is the case for our experimental device, see Fig. 3.16 (a). Multistability of a larger degree can be expected for devices with higher α. Very close to threshold, the distance from the lasing threshold P determines how many of the lasing modes in the L-K model are physical. In experiment, a stable lasing mode can be replaced by the stable off state, when the laser current is set very close to threshold. As a result, multistability of two continuous wave states and the off state can be observed.

3.5 Summary

In this chapter, I presented a study of multistability of a single-mode DFB laser, which is subject to ultrashort delayed optical feedback. Just above threshold, a regime of

tristability is found for multiple ranges of amplifier and phase currents. Sufficiently close to threshold, a lasing state might be replaced by the stable off-state and vice-versa. Either three continuous-wave (cw) states, or two cw states and the stable off state may coexist. The main features of the experimental data are captured quantitatively very well by the Lang-Kobayashi model. The intrinsic nonlinearity of the semiconductor material, described by the linewidth-enhancement factor α, can be identified as the key parameter determining the maximum degree of multistability. An analytic formula expressing the maximum number of coexisting stable states as function of the material parameter α was established. This shows a possible way to systematically increase the number of coexisting states. The separation between the tristable wavelengths agrees with the channel spacing of dense wavelength multiplexing used in optical communication. This makes the device interesting for all-optical switching applications.

4 Synchronization of Quasiperiodic Oscillations

Synchronization is the mutual frequency adjustment of self-sustained oscillators, which interact through a weak coupling. Oscillatory behavior and synchronization processes are ubiquitous in nature and technology [3, 2]. Surprisingly, it was found that even chaotic oscillators can synchronize to each other, although their individual time evolution is fundamentally unpredictable. For the limiting cases of nearly identical oscillators as well as chaotic oscillators, synchronization is well understood and sophisticated mathematical methods exist for its description, see e.g. [94, 95, 16]. Quasiperiodic oscillations are of intermediate complexity. They have two or more fundamental frequencies, which in general are the result of independent physical mechanisms. Examples for quasiperiodic oscillatory processes are numerous. They include our own cardio-respiratory system, modulated electromagnetic waves as used for radio broadcasts, or planetary motion in astronomy [96]. Surprisingly, the synchronization of quasiperiodic oscillations is less well explored [97, 98, 99]. A simplified scheme of such a quasiperiodic oscillation, subject to a periodic external forcing, can be found in the right panels of Fig. 4.1. The example chosen is the simplest extension to the classical case of synchronization, shown in the left panel for comparison. The question I will address in the following is of a fundamental nature: What happens, when an external frequency f_{ext} synchronizes to one of the frequencies of a quasiperiodic oscillation?

In this chapter, I study synchronization in a system of two coupled multisection semiconductor lasers. The simplest possible scenario for synchronization of quasiperiodic oscillations, shown in Fig. 4.1, is realized. Periodic self-pulsations of laser 1 are injected into laser 2, which is operating in a regime with two-frequency quasiperiodic self-pulsations, see Fig. 4.2 (b) for a simplified experimental scheme. Concerning possible synchronization between the three frequencies, the experiment confirms the new regimes which have been theoretically predicted recently in Ref. [98]. An important complication is that the fundamental frequencies of a quasiperiodic oscillations can lock to each other, e.g., heartbeat and breathing rhythm show epochs of synchronicity [100]. The results demonstrate in particular that synchronization of a resonant limit cycle on a torus, which is formed by two mutually locked frequencies, is fundamentally different from classical synchronization of periodic motions. In the classical case, all frequency peaks in the power spectrum can be observed to shift. This happens regardless whether the fundamental frequency is synchronized directly to the external signal, or at a higher harmonic. A resonant quasiperiodic oscillation has the same comb of equidistantly spaced peaks in the power spectrum. However, it will exhibit a drastically different behavior when either of the two fundamental frequencies is synchronized. This is because the

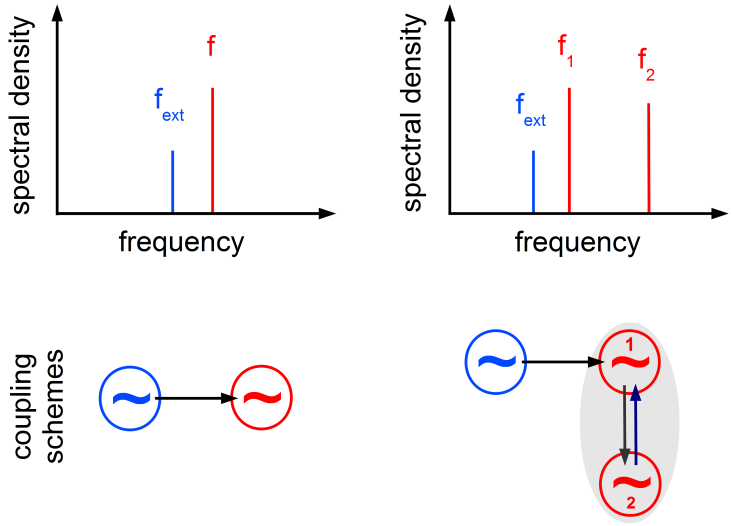

Figure 4.1: Synchronization of a periodic and a quasiperiodic oscillation by a periodic external forcing. f_{ext}, external frequency. f, frequency of a periodic oscillatory process. f_1 and f_2, frequencies of two mutually coupled oscillatory processes forming a quasiperiodic oscillation. Upper panels, power spectra. Lower panels, coupling schemes of the oscillatory units.

oscillatory processes involved each have a distinct physical origin. In any case, the external force first destroys the regime of initial mutual synchronization. Their mutual coupling strength in relation to the coupling strength of the external frequency then determines the synchronization properties. Moreover, carefully determining the coherence of the noisy oscillations, interesting processes of coherence transfer to non-synchronized oscillations are revealed, which are theoretically unexplored so far.

4.1 Experimental Setup

Two different multisection lasers, fabricated by the Fraunhofer Heinrich-Hertz Institut, are used in the experiment. As has been demonstrated previously [101, 102], well-defined dynamical regimes of operation can be prepared in such lasers by adjusting the injection currents appropriately. Here, the emergence of intensity self-pulsations is of relevance. As described in the previous chapters, mode-beating pulsations of frequency f_{MB} result from the beating of two cavity modes and are born in a Hopf bifurcation. Undamping of the relaxation oscillations in a torus bifurcation leads to a second pulsation of frequency $f_{\mathrm{RO}} < f_{\mathrm{MB}}$. The superposition of these two oscillations of different physical origin provides the quasiperiodic dynamics for the following experiments. An essential feature in this study is that f_{RO} and f_{MB} can be tuned in a sufficiently wide range by the pump currents, which allows to arrange certain resonance conditions.

The scheme of the experimental setup is shown in Fig. 4.2 (a). Panel (b) provides

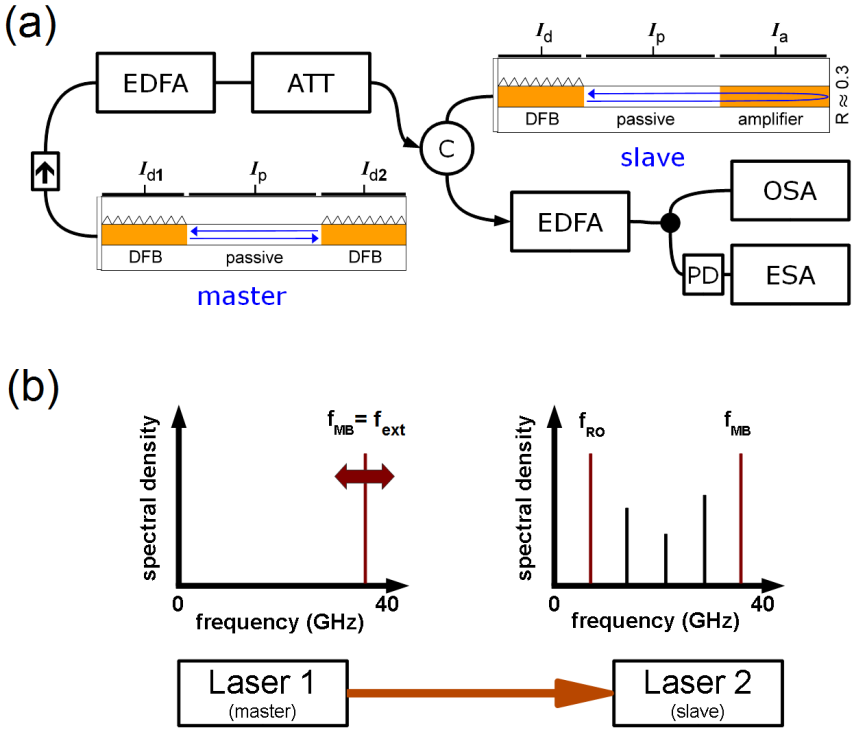

Figure 4.2: (a) Sketch of the experimental setup and schematic side view of the multisection devices, for device technical details see e.g. [101]. Distributed feedback (DFB) laser current I_d, phase current I_p, and amplifier current I_a are supplied with an accuracy of ± 0.05 mA. The temperature is stabilized at 20.01 ± 0.01 °C in both lasers. Light emitted from the anti-reflection coated DFB facet is coupled into a single mode fiber. Arrow, optical isolator. C, optical circulator. ATT, attenuator and power meter (Eigenlight 420 WDM). EDFA, erbium doped fiber amplifier (Alcatel). OSA, optical spectrum analyzer (HP 71451-B). PD, ultrafast photo diode (u2t). ESA, electrical spectrum analyzer (Rohde & Schwarz FSP 9).
(b) Experimental scheme with simplified power spectra of master and slave laser. f_{ext} of the master is injected into the slave in order to synchronize f_{MB}. In this example the quasiperiodic oscillation in the slave is locked, i.e., f_{RO} and f_{MB} are mutually synchronized at an integer ratio. Additional peaks are higher harmonics and mirror peaks, see text.

a simplified schematic of the dynamics in both devices. The slave laser is running in the quasiperiodic regime with both types of pulsations, marked by f_{RO} and f_{MB}. This device is almost identical to one used to investigate the multistable regime in the previous chapter. It has been grown on the same wafer, with a by 200 μm longer phase tuning section being the only difference. An integrated tandem device (ITL) is the master laser, serving as external force and adjusted so as to exhibit mode-beating pulsations only. For distinction with the slave laser, their frequency is denoted here by f_{ext}. As shown in (a), the output of the master is first amplified by an Alcatel erbium doped fiber amplifier (EDFA). The external coupling strength can be fine tuned by a combined Eigenlight 420 WDM power meter/attenuator element (ATT), controlling the master intensity that is coupled into the slave via an optical circulator (C). The output of the slave laser is routed by the circulator to a second EDFA and amplified. The signal then is analyzed by a HP 71451-B optical spectrum analyzer (OSA) with a wavelength resolution of 0.1 nm, as well as an ultrafast u2t photodiode (PD) combined with a Rohde&Schwarz rf-spectrum analyzer (ESA) with 40 GHz bandwidth. All operating parameters of the two lasers, as well as the data acquisition by ESA and OSA, can be controlled by a computer program which I developed for our experiments.

Time series resolving oscillations exceeding 30 GHz are not yet experimentally accessible by most state-of-the-art equipment. As the frequencies of the intensity variations in our experiments can significantly exceed this limit, the relevant information has to be extracted from the measured power spectra. In this context, the coherence of the intensity pulsations will be characterized by an inverse coherence time τ_c^{-1} [103], which is related to the intensity variations P(t) as follows: The intensity variation $P(t)$ is detected by the ultrafast photodiode and truncated to a finite time interval $\Delta_t = (-\frac{T}{2}, \frac{T}{2})$ when analyzed by the ESA. Let $F_T(\omega)$ designate the Fourier transform of $P(t)$, where $\omega = 2\pi f$ as usual. Assuming that the power spectrum can be approximated as well as needed by $F(t)$, i.e. the identity $S(\omega) = \lim\limits_{T\to\infty} \frac{|F_T(\omega)|^2}{T}$ holds for the power spectral density $S(\omega)$, the inverse Fourier transform of $S(\omega)$ is the non-normalized autocorrelation function $C(\tau)$ of the power transient $P(t)$ [104],

$$\begin{aligned}\mathcal{F}^{-1}\{S(\omega)\} &= \frac{1}{2\pi}\int_{-\infty}^{\infty} \lim_{T\to\infty} \frac{|F_T(\omega)|^2}{T} e^{i\omega\tau} d\omega \\ &= \lim_{T\to\infty} \frac{1}{T}\int_{-T/2}^{T/2} P(t)P(t-\tau)dt = C(\tau).\end{aligned}$$

$C(\tau)$ can therefore be determined from the measured power spectra. The limit $T \to \infty$ is approximated by averaging over 10 sweeps over the selected frequency range. Each full sweep takes a few milliseconds, which is six orders of magnitude slower than the intensity pulsations. An appropriate frequency window of the power spectra, containing only the peak under consideration[1], is evaluated. τ_c is obtained by calculating $\tau_c = \int_0^\infty C^2(t)dt$ and will be used to quantify the coherence of the noisy peaks of f_{RO} and f_{MB}.

[1] This not possible in small regions on both borders of a synchronization region. There, broad peaks with contributions of e.g. both f_{MB} and f_{ext} overlap and cannot be separated.

4.2 Experimental Results

4.2.1 Free-Running Slave Laser

First, I characterize the quasiperiodic motion in the free running slave laser in detail. Fig. 4.3 shows an overview of the points of operation used in the following. I_d and I_p are fixed, and the current applied to the amplifier section is changed. Average power, power spectra and optical spectra are recorded while traversing a full hysteresis loop, which includes more than one full period of the feedback phase φ. As in the last chapter, discrete branches of average emission power can be observed in Fig. 4.3 (c). They have a considerably smaller overlap when compared to the multistable regime in the previous chapter. Only regions with bistability can be found, marked by the blue and yellow shading in Fig. 4.3. The arrows indicate a typical hysteresis loop. Optical spectra and power spectra show that single-mode cw emission constitutes only a small part of the dynamics. Mode-beating oscillations are observed for almost all of a feedback phase period. In panel (d), a peak at $f_{\mathrm{MB}}/2$, characteristic for a period-doubling bifurcation and marked by PD, appears in a small range of I_a. Additionally, relaxation oscillations are not strongly damped anymore.

For appropriately chosen feedback parameters, controlled by amplifier and phase current, both f_{RO} and f_{MB} may coexist and various additional peaks are visible. Just before the jump to the next mode with increasing I_a, RO get undamped and a two-frequency oscillation of MB and RO forms in the power spectra shown in panel (d). The laser emits such a quasiperiodically varying intensity only in a small part of a feedback phase period. The quasiperiodic regime lies fully within the bistable region, i.e., it is observed only for increasing I_a in panel (d), but not in (a). Decreasing I_a again, after the jump to the output power branch belonging to the next optical mode pair, only MB pulsations are observed. Changing the feedback parameters, the two types of intensity pulsations may synchronize to each other at integer ratios. With all other currents and the temperature fixed, internal synchronization of f_{RO} and f_{MB} is now studied as a function of the amplifier current.

Fig. 4.4 shows the formation of the 1:5 resonance between f_{RO} and f_{MB} in a very small parameter interval of Fig. 4.3 in detail. Setting $I_d = 89.97$ mA and $I_p = 42.95$ mA, I_a is increased from 68.48 to 70.00 mA. Figs. 4.4 (a-d) show the power spectrum in the vicinity of each peak that can be detected up to 40 GHz. Intensities are encoded in logarithmic gray scale. In addition to the two fundamental frequencies f_{RO} (a) and f_{MB} (e), the nonlinear amplitude-phase coupling in the laser gives rise to various extra features such as higher harmonics ($2f_{\mathrm{RO}}$ (b), $3f_{\mathrm{RO}}$ (c), ...) and mirror peaks ($f_{\mathrm{MB-RO}}$ (d), $f_{\mathrm{MB-2RO}}$ (c), ...). The latter directly evidence an internal interaction between the two fundamental oscillations. Increasing the control parameter I_a, RO (a) slow down and while MB (b) accelerate. Both frequencies lock to each other at an integer ratio of 5 within a finite interval. Within this interval, the width of all peaks is significantly reduced and all higher harmonics and mirror peaks increase in amplitude. This change is most pronounced in (c), where now $3f_{\mathrm{RO}}$ and $f_{\mathrm{MB-2RO}}$ coincide. Control parameter variations do not change the resonant conditions. The red solid line from (a) to (e) within this locking

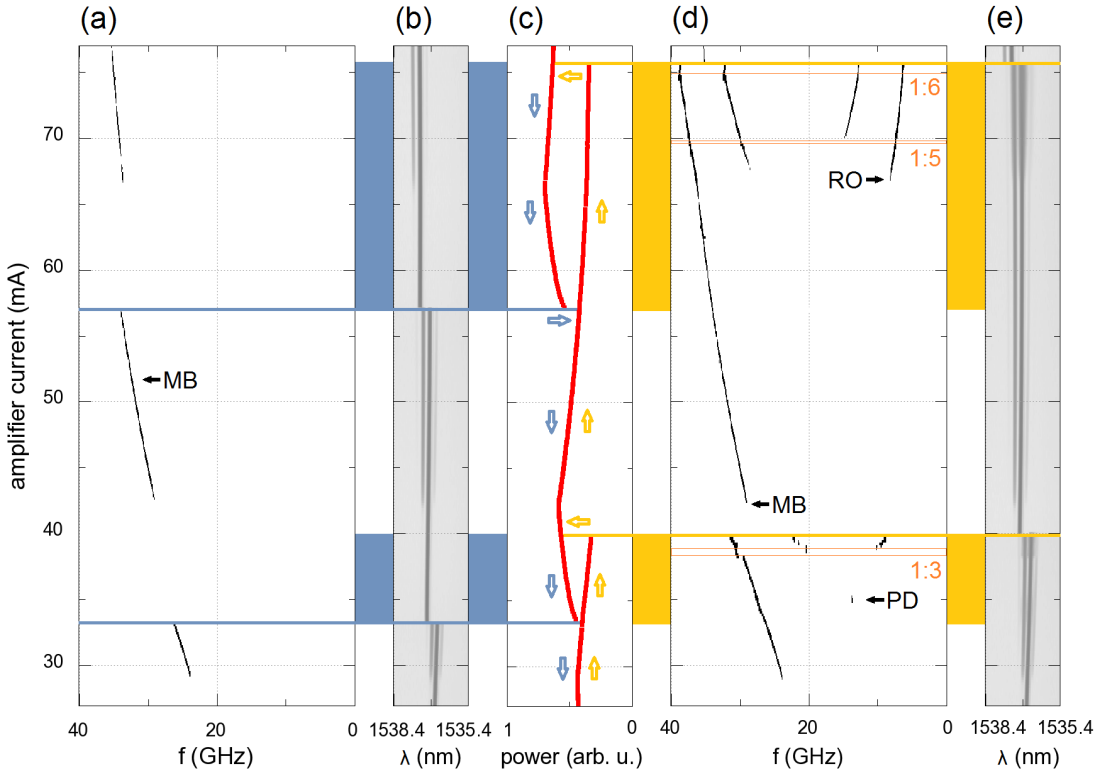

Figure 4.3: Free running slave, overview measurements including different quasiperiodic intensity pulsation regimes. $I_d = 89.97$ mA, $I_p = 42.95$ mA. The amplifier current I_a is changed between 27 and 77 mA, changing feedback phase and feedback strength. Bistable regions, marked blue and orange, span a huge part of a feedback phase period. (a),(d): power spectra recorded while decreasing (a) and increasing I_a (d). The spectral density is encoded in a logarithmic gray scale. Arrows mark the location of MB and RO oscillations. A period doubling of MB is observed in a short interval of (d), marked PD. Increasing I_a in (d), RO get undamped in a torus bifurcation. Resonances of orders 1:3, 1:5 and 1:6 are observed. See Fig. 4.4 for high resolution power spectra at the 1:5 resonance. Decreasing I_a, only MB is observed. (b),(e): optical spectra recorded while decreasing (b) and increasing I_a (e). Spectral density is encoded in a logarithmic gray scale. (c): variation of the average output power when changing I_a. Note the change in slope whenever MB set in. Blue and yellow arrows mark a typical hysteresis loop. Two discrete jumps in wavelength and power are observed for each increasing and decreasing I_a, marking the beginning or end of a feedback phase period, see also the previous chapter.

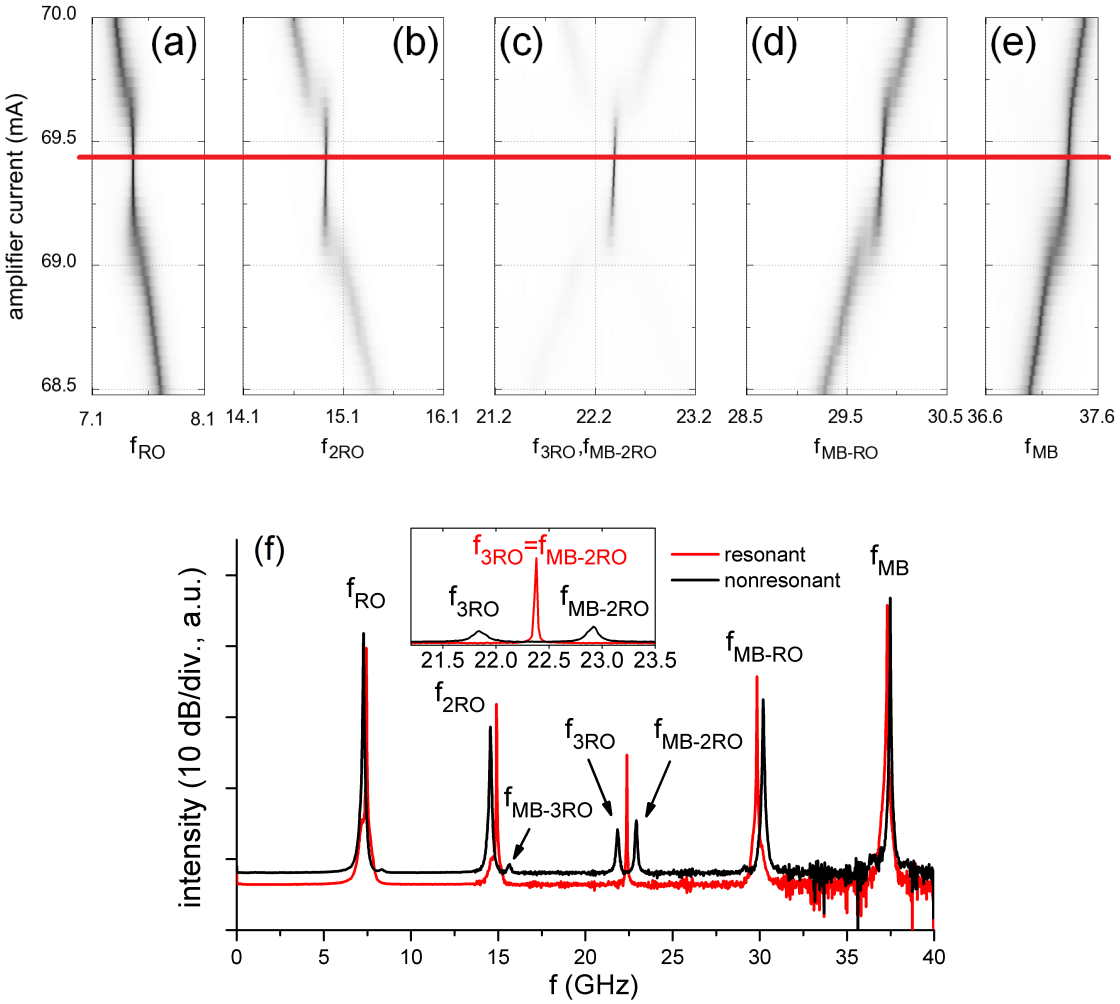

Figure 4.4: Quasiperiodic oscillation in the free running slave. $I_d = 89.97$ mA, $I_p = 42.95$ mA. I_a is increased from 68.48 to 70.00 mA. (a-e) Power spectra around the individual peaks. Intensity is encoded in gray scale (log-scale). In a finite region, f_{RO} and f_{MB} lock to each other at a 1:5 resonance, see also Fig. 4.5. Red (gray) line, parameter of (f), resonant case. (f) Exemplary power spectra, full span. Red (gray) line: internally synchronized, $I_a = 69.43$ mA. Black line: no internal synchronization, $I_a = 70.20$ mA. Inset: details at mid frequency. Note the increased peak amplitude and decreased peak width for internal synchronization.

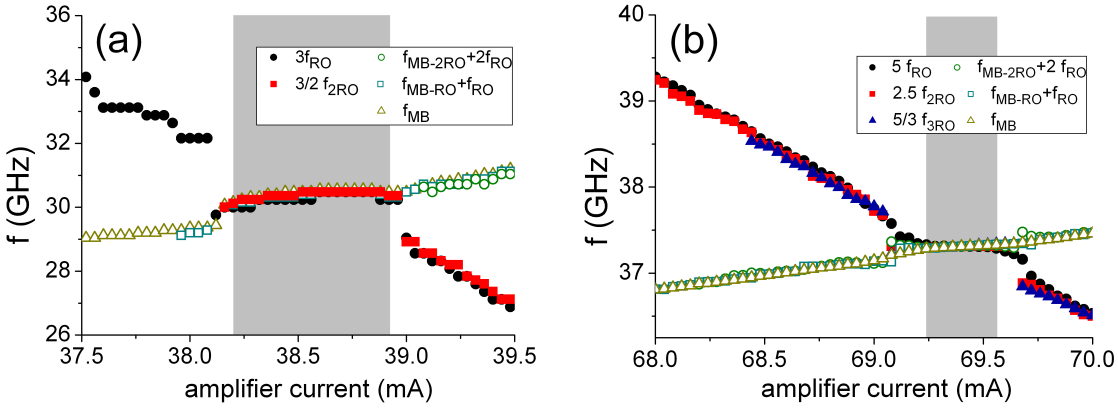

Figure 4.5: Variation of the rescaled peak frequencies with I_a. f_{RO} and its harmonics decrease with I_a, whereas f_{MB} and mirrors of RO at MB increase slightly. Within $I_a = 38.20 - 38.92$ (a) and $69.24 - 69.56$ mA (b), shaded gray, f_{RO} and f_{MB} are mutually synchronized at a ratio of 1:3 (a) and 1:5 (b).

region marks the value of I_a for the full spectrum in Fig. 4.4 (f), red solid line. The second spectrum in (f), black solid line, represents a typical non-resonant case. The same measurements have been repeated for a 1:3 resonance. For this purpose, I_d and I_p were kept at the same values. I_a was reduced to reach the previous feedback phase period, and then increased again towards the region of quasiperiodic emission, as detailed in Fig. 4.3. The mode-beating oscillation is now due to a different mode pair, see Fig. 4.3 (e). The slightly changed feedback parameters predominantly result in a slower f_{MB}, and a 1:3 resonance with f_{RO} can be observed.

When properly rescaled, all peaks follow either RO or MB when changing I_a, see Fig. 4.5. In a certain amplifier current range, shaded gray, both oscillations lock to each other at winding numbers $\theta = f_{\mathrm{MB}}/f_{\mathrm{RO}} = 3$, Fig. 4.5 (a), and $\theta = 5$, Fig. 4.5 (b). The MB frequency at $\theta \approx 3$ is around 30 GHz and at $\theta \approx 5$ around 37 GHz. Obviously, the $\theta = 3$ resonance is stronger, as indicated by the substantially larger locking range in frequency. When comparing the locking ranges as function of the amplifier current, one has to keep in mind that the two neighboring feedback phase periods are not equivalent. The phase tuning is increasingly efficient for smaller I_p and I_a, e.g., see Fig. 3.15 on page 49. Therefore, in our scenario the increase in coupling strength is actually underestimated when characterizing the locking range by the parameter I_a.

After elaboration of the internal synchronization scenario, the response to the external periodic forcing can be studied selectively, in the presence or absence of internal locking, and for the two different internal coupling strengths associated with the winding numbers $\theta = 3$ and $\theta = 5$. In Ref. [34] was shown that a solitary mode-beating pulsation generated by our multisection laser can be synchronized to an external optical signal. Like in the following experiments non-coherent injection was used, i.e., the wavelength of the external signal was detuned with respect to the slave laser. The injected optical power had to be in the mW range to observe synchronization and the observed locking range was

found to increase linearly with increasing injected power. When coupling the slave to the external frequency, the general scenario for changing the amplifier current presented in the overview measurements of Fig. 4.3 will remain essentially unchanged. In particular, because the external coupling is weak, the synchronization experiments can be done without inducing a jump to the coexisting stable state.

4.2.2 Lasers Coupled in a Master-Slave Configuration

Now, master and slave are coupled. The optical emission of the master with frequency f_{ext} is injected into the DFB laser section of the slave to synchronize f_{MB}, see the simplified experimental scheme in Fig. 4.2 (b). The optical injection leads to several new lines in the high-resolution power spectrum due to the presence of nonlinear mixing within the slave. There are no significant unidentified peaks (5 dB above noise level). Linear tuning of f_{ext} without hysteresis is achieved by tuning one of the direct pump currents of the master. The power in the attenuator element is set to a value of +5 dBm, corresponding to 3.2 mW mean optical power. This mean optical power will be used to characterize the coupling strength from here on. A characteristic value for the losses at the interface between laser and tapered fiber is 6 dB in both directions, equivalent to a coupling coefficient of ≈ 0.25 [34]. Neglecting all losses in e.g. the optical fibers, couplings and isolator, 3.2 mW mean optical power corresponds to a net injection of 0.8 mW into the slave. Given an average optical output power of 2 mW of the slave, measured within the fiber, this corresponds to an estimated injection level of around 10%. Below a coupling strength of zero dBm (1 mW) no synchronization is detected. A linear increase in the injected optical power from around zero dBm on leads to a linear increase of the locking range of f_{MB} to f_{ext}, indicating a regime of weak forcing.

The locking range of f_{ext} to f_{MB} is in the order of a few hundred MHz. The changes visible for the peak of f_{RO} (and therefore its higher harmonics and all mirror frequencies) are of similar magnitude. They are small when compared to the peak frequency separation of the quasiperiodic oscillation, which is a few GHz. As the electrical spectrum analyzer records 2001 data points for a given frequency span, the resolution of the obtained power spectra is not sufficient if this span covers the full available range from 9 kHz to 40 GHz. Therefore, each synchronization experiment is repeated twice in order to record high resolution spectra around each f_{RO} and f_{MB}. No drift in the point of operation was detected by control measurements in the experiment for a timespan of less than two hours. No hysteresis was detected in the locking behavior when increasing and decreasing f_{ext}. Therefore, only results for increasing f_{ext} are presented.

4.2.3 The Case of Strong Internal Synchronization

First, synchronization of f_{MB} to f_{ext} at $\theta = f_{\mathrm{MB}}/f_{\mathrm{RO}} = 3.26$ is investigated. All relevant experimental parameters can be found in table 4.1. Fig. 4.6 (a) shows power spectra of the intensity pulsations in the slave, recorded at f_{MB}, for increasing the laser current of the master. The frequency window including f_{MB} spans one GHz. Intensities are encoded by a logarithmic gray scale. Both f_{MB} and f_{ext} are marked by an arrow. The

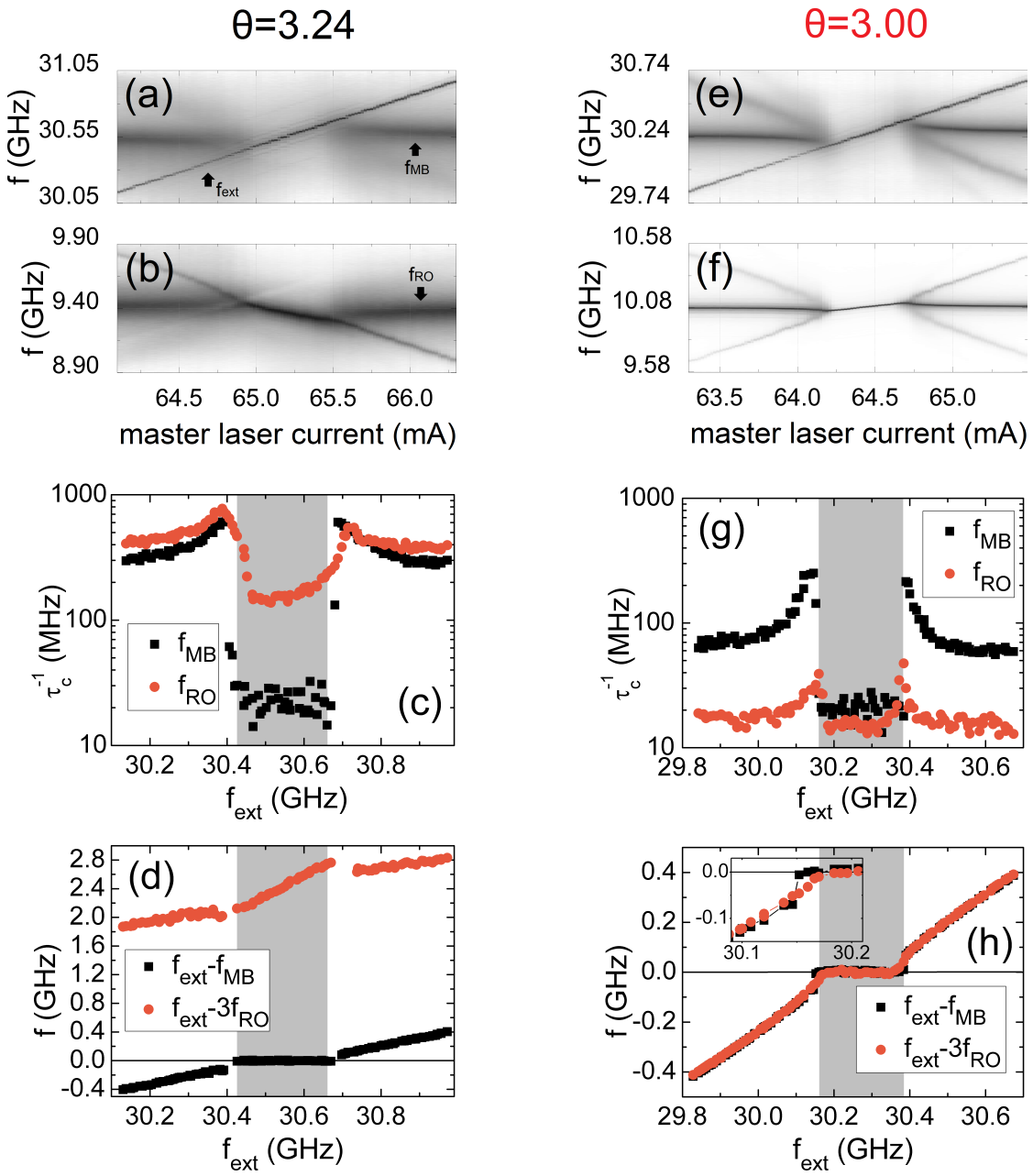

Figure 4.6: Synchronization of f_{MB} to f_{ext} at $\theta = 3.24$, (a)-(d), and $\theta = 3.00$, (e)-(h). (a,e) Power spectra for increasing the master laser current I_{d2}, corresponding to increasing f_{ext}, details around f_{MB}. (b,f) Details around f_{RO}. (c,g) Inverse coherence time τ_c^{-1} of f_{RO}, red (gray) circles, and f_{MB}, black squares. See text for details. (d,h) f_{RO} and f_{MB} rescaled with respect to f_{ext}. Shaded gray: locking range of f_{MB}, only one peak within ±0.5 GHz. Inset of (h): f_{MB} is locked earlier than f_{RO}.

linearly increasing external frequency of the master is clearly visible as a sharp diagonal line. Fig. 4.6 (b) shows corresponding power spectra recorded at f_{RO}; f_{RO} is also marked by an arrow. As mentioned before, additional peaks appear in the power spectrum due to frequency mixing. A peak corresponding to the frequency difference $f_d = |f_{\mathrm{ext}} - f_{\mathrm{MB}}|$ is present when looking at the full spectrum starting at 9 kHz (not shown). Satellite peaks appear on both sides of all peaks already present in the free running slave at a distance equal to $\pm f_d$. This is most clearly visible outside of the locking region in Fig. 4.6 (e,f) - in (a,b), two of them have a very low amplitude. The height of the satellite peaks at $f_{\mathrm{peak}} - f_d$ and $f_{\mathrm{peak}} + f_d$ is not equal, see for example Fig. 4.6 (b), where this inequality is very pronounced. The amplitude is generally larger on the low frequency side of f_{RO} (and its higher harmonics) when $f_{\mathrm{ext}} > f_{\mathrm{MB}}$, and vice versa. This may be related to the peculiarities of the internal coupling between f_{RO} and f_{MB}. As can be expected, the mirror peaks at $(f_{\mathrm{MB-RO}}, f_{\mathrm{MB-2RO}}, ...)$ have the higher-in-amplitude satellite on the opposite side (not shown).

The spectra presented in (a) and (b) are evaluated as follows. First, the peak positions of f_{RO}, f_{MB} and f_{ext} are determined. f_{RO} and f_{MB} are then rescaled with respect to the external frequency, and plotted in (d). The locking range of f_{MB}, corresponding to only one peak within the one GHz range around f_{MB} in (a), is shaded gray. As can be seen in the center of Figs. 4.6(d), only f_{MB} is locked by the injected f_{ext}, within a range of 252±11 MHz. In a further step, the coherence of both f_{RO} and f_{MB} is determined as described previously. To this purpose, the part of the spectrum containing the individual peak is isolated. Then, the inverse coherence time is determined following equations (4.1). The inverse coherence time τ_c^{-1} is plotted in (c) as function of tuning f_{ext}. In a very small region at both locking borders, the peak in question cannot be clearly separated from f_{ext} anymore, and the determined (inverse) coherence time is slightly too low (high). For f_{RO} a significant increase in coherence by a factor of more than two is visible, although it is non-resonant to both f_{MB} and f_{ext}. Additionally, the relaxation oscillations slow down while f_{MB}, which is locked to f_{ext}, increases. While a direct interaction of f_{ext} with f_{RO} cannot be excluded, non-resonant conditions indicate that the internal coupling between the mode-beating and relaxation oscillations is responsible for this transfer of coherence, and change in frequency.

The winding number is now adjusted to $\theta = 3$, see Fig. 4.6 (e)-(h). This corresponds to internal synchronization of f_{RO} and f_{MB} in the gray shaded center of Fig. 4.5 (a). f_{MB} synchronizes to f_{ext} within 217 ± 7 MHz. Three regimes can be identified in Figs. 4.6 (g,h) and the inset of Fig. 4.6 (h). On the right and left side of Figs. 4.6 (g,h), f_{RO} and f_{MB} are internally synchronized. In the gray shaded center, both RO and MB are locked to f_{ext}. In a small parameter interval on both borders of this center region no internal resonance between f_{RO} and f_{MB} exists, while f_{MB} is locked to f_{ext}. See the inset of Fig. 4.6 (h) for details. The internal locking is first broken, before the regime of synchronization of all three frequencies is established. The synchronization mechanism is clearly different from synchronization of a classical limit cycle at a higher harmonic, where all peaks synchronize to the external frequency at the same time. As can be seen in Fig. 4.6 (g), the coherence of the RO is higher than the coherence of the MB. In the locking range shaded gray, the coherence of the RO nearly reaches the coherence

master (ITL)	I_d^m (mA)	I_p^m (mA)	I_a^m (mA)	f_{ext} (GHz)
nonresonant	47.49	10.59	64.10-66.30	30.13-30.97
resonant	47.49	10.59	63.30-65.50	29.83-30.67
slave (AFL)	I_d^s (mA)	I_p^s (mA)	I_a^s (mA)	θ
nonresonant	90.07	43.03	39.40	3.26
resonant	90.07	43.03	38.80	3.00

Table 4.1: Experimental parameters for synchronization to f_{MB}^s at $\theta \approx 3$. Tuning of f_{ext} is linear and without hysteresis. The temperature is stabilized at 20.01±0.01 °C in both lasers.

separately measured for f_{ext}, while f_{MB} is less coherent than both f_{ext} and f_{RO}. This implies that the lower coherence of the MB is not a limiting factor for the transfer of coherence from f_{ext} to f_{RO}.

4.2.4 The Case of Weak Internal Synchronization

The point of operation of the slave is now adjusted to $\theta \approx 5$, all relevant experimental parameters can be found in table 4.2. The internal coupling strength of the torus is decreased compared to $\theta \approx 3$, while the coupling strength of the external frequency f_{ext} remains the same. The results for $\theta = 4.91$, Figs. 4.7 (c,d), are qualitatively equivalent to the case $\theta = 3.26$ in Fig. 4.6 (c,d). The locking range of f_{MB} to f_{ext} is smaller at 196 ± 17 MHz and the MB frequency now is faster at ≈ 37 GHz instead of ≈ 30 GHz. Again, for all peaks the coherence increases significantly in the center of the synchronization region of f_{MB} to f_{ext}.

Now I_a is adjusted for internal resonance at $\theta = 5$, Fig. 4.7 (e)-(h). Synchronization differs markedly from the case of $\theta = 3$ in Fig. 4.6 (e)-(h). f_{MB} locks to f_{ext} within a considerably reduced range of 106 ± 13 MHz and shows an increase in coherence. f_{RO} however remains almost stationary when f_{MB} is synchronized to f_{ext}, see Figs. 4.7 (f,h). At the given internal coupling strength, synchronization of both RO and MB to f_{ext} as for $\theta = 3$ is not achieved. In contrast to synchronization of a classical limit cycle, where all frequency peaks would be expected to shift, only f_{MB} locks to the external signal. If f_{RO} is near stationary, a small interval has to exist where f_{RO} is again resonant to the quasiperiodic oscillation now formed by the mutually locked f_{MB} and f_{ext}. This explains the increase in coherence of f_{RO} within the locking range of f_{MB} to f_{ext}.

4.2.5 Experimental Summary and Discussion

Though only a few selected values of θ have been examined above, the results are representative in the following sense. First, the similarity between $\theta = 3.24$ and $\theta = 4.91$ demonstrates that the scenario does not qualitatively depend on the exact value of θ in the nonresonant case. Second, $\theta = 3$ and 5 define the two fundamental synchronization regimes of weak and strong internal resonances, respectively [98]. The external synchronization of the intermediate resonance $\theta = 4$ was not successful, although numerous

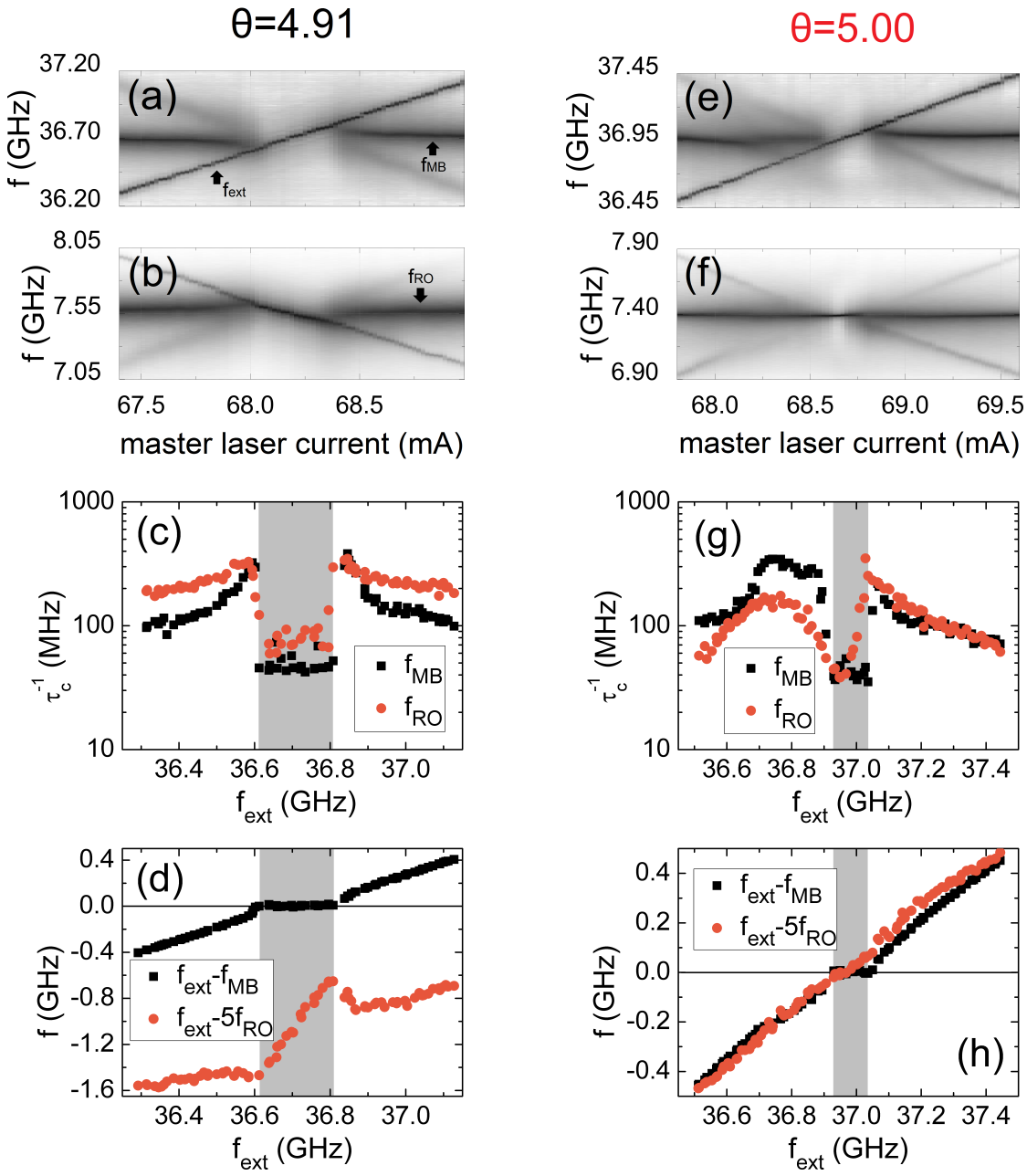

Figure 4.7: Synchronization of f_{MB} to f_{ext} at $\theta = 4.91$, (a)-(d), and $\theta = 5.00$, (e)-(h). (a,e) Power spectra for increasing the master laser current I_{d2}, corresponding to increasing f_{ext}, details around f_{MB}. (b,f) Details around f_{RO}. (c,g) Inverse coherence time τ_c^{-1} of f_{RO}, red (gray) circles, and f_{MB}, black squares. See text for details. (d,h) f_{RO} and f_{MB} rescaled with respect to f_{ext}. Shaded gray: locking range of f_{MB}, only one peak within ± 0.5 GHz. Note the significant reduction for $\theta = 5$.

master (ITL)	I_d^m (mA)	I_p^m (mA)	I_a^m (mA)	f_{ext} (GHz)
nonresonant	39.07	0.00	67.40-69.00	36.29-37.13
resonant	39.07	0.00	67.80-69.60	36.51-37.44
slave (AFL)	I_d^s (mA)	I_p^s (mA)	I_a^s (mA)	θ
nonresonant	90.02	43.24	68.50	4.91
resonant	90.02	43.24	69.20	5.00

Table 4.2: Experimental parameters for synchronization to f_{MB}^s at $\theta \approx 5$. Tuning of f_{ext} is linear and without hysteresis. The temperature is stabilized at 20.01±0.01 °C in both lasers.

attempts have been made. The locking range between RO and MB at $\theta = 4$ in the solitary slave laser is larger than for $\theta = 5$, therefore the technical difficulty of the experiment is not increased. It is interesting to note that this behavior also seems to reflect the classification of quasiperiodic resonances in the mathematical literature: ($\theta \geq 5$) and ($\theta \leq 4$) are weak and strong resonances, respectively, with $\theta = 4$ as a peculiar case regarding its stability [105, 106, 107]. The resonances $\theta = 2$ and $\theta \geq 6$ are not accessible with the experimental setup. $\theta = 2$ is a peculiar case, as the mode-beating peak forms within the strong second harmonic of f_{RO}, i.e., f_{MB} is visible separately only after the resonance breaks up. For $\theta > 5$, the locking ranges of the internal resonances are not sufficiently large anymore. Additionally f_{MB} is near to, or exceeds, the upper limit of the frequency range that can be detected with our ESA.

Two experimental conditions remain to be addressed. First, the intensity pulsations used in the experiment are modulated waves with an optical carrier frequency which is orders of magnitude faster. Synchronization is nontrivial already for periodic intensity self-pulsations, as both locking of the intensity modulation and locking in the optical domain may appear, if the respective frequencies are close [108]. When coupling the light of the master into the slave, interactions in the optical domain have to be avoided. Even when the wavelength detuning $\Delta\lambda$ of master and slave is large enough to exclude synchronization in the optical domain, it might affect the locking cones of the intensity pulsations [109]. It was found that possible intensity beating of optical modes and synchronization in the optical domain only play a role below 1 nm separation between the two emission wavelengths. To this purpose, the locking cones of a solitary relaxation oscillation pulsation to an injected frequency have been determined, while systematically detuning the wavelength of the master by changing its temperature. For large $\Delta\lambda$, no changes in the synchronization scenario could be found. When the wavelength detuning becomes small enough an additional beat frequency f_b, corresponding to $\Delta f = -c\Delta\lambda/\lambda^2$, can be observed in the power spectrum. f_b does not influence the synchronization scenario, even though additional peaks due to mixing effects appear when $\Delta\lambda$ is reduced further. At $\Delta\lambda \approx 0.15$ nm synchronization in the optical domain is observed, leading to a drastic change both optical and power spectrum of the slave. In our experiments investigating the synchronization of quasiperiodic intensity pulsations, the emission wavelength of master and slave are detuned by about 15 nm, far exceeding

$\Delta\lambda \approx 1$ nm. The results of control measurements with an optical separation of $\Delta\lambda \approx 1$ nm, achieved by using an AFL instead of the ITL as master laser, agree with the data obtained for $\Delta\lambda \approx 15$ nm.

The second experimental peculiarity is that the mean power in the slave is modified by the injected light, even for weak coupling. All intensity pulsation frequencies are decreased by a small amount, locking cones therefore are tilted to lower frequencies with increasing strength of external coupling [110]. The operating parameters of the slave have to be readjusted slightly for the locked torus, as the mutual locking region of both torus frequencies is shifted. The change in the point of operation does not seem to influence the scenario described e.g. in Fig. 4.5, besides the small shift in frequency.

4.3 Comparison with Theory

A few experimental findings presented can be understood from synchronization of periodic oscillations. I will therefore first give a short recapitulation.

A self-sustained damped oscillator with a fundamental frequency f is associated with a classical limit cycle in phase space. As an example, in Fig. 4.8 (a) the stable limit cycle of a van der Pol oscillator has been plotted. Trajectories starting from two different initial conditions are shown, which both eventually converge towards the limit cycle. Panel (b) shows the limit cycle associated with an exemplary mode-beating intensity pulsation in our experimental device, obtained by device-realistic simulations. On and near such a classical limit cycle the phase of the oscillation, a variable which increases by 2π for each completed revolution can be defined. For an arbitrary limit cycle this phase grows linearly, but in general not uniformly, with time. A change in oscillation amplitude by a sudden external force is quickly restored due to the transversal stability of the limit cycle. Motion on the limit cycle itself corresponds to motion along a neutral direction, the phase can therefore be changed by infinitesimally small perturbations. We now introduce an external frequency f_{ext}. A sufficiently small frequency mismatch between f and f_{ext} leads to synchronization of the oscillator phase to the phase of the external perturbation, while the amplitude variation may remain unsynchronized. Such phase synchronization has been the subject of investigation in this chapter.

Higher order synchronization is possible, e.g. using $f_{\text{ext}} = 2f$, but the larger accumulated phase difference between the external forcing and the oscillation has to be compensated by a stronger coupling. If the coupling strength is kept constant, therefore the locking cone will be narrower. Locking ranges for super- and subharmonic synchronization at rational frequency ratios m/n are increasingly narrow the larger n and m. Noise and limited control of parameters make it complicated to observe these Arnol'd tongues in experiments[2]. Fig. 4.9(a) shows the locking cones for an experimental example, a laser subject to external periodic forcing. The synchronization at a frequency ratio of 1:1 has the widest locking range. All higher order locking cones besides 1:2 are too narrow to be experimentally resolved and appear as lines.

[2] As rational and irrational numbers can only be approximated by floating point numbers, the numerical computation of such locking cones for mathematical models is also tricky [111].

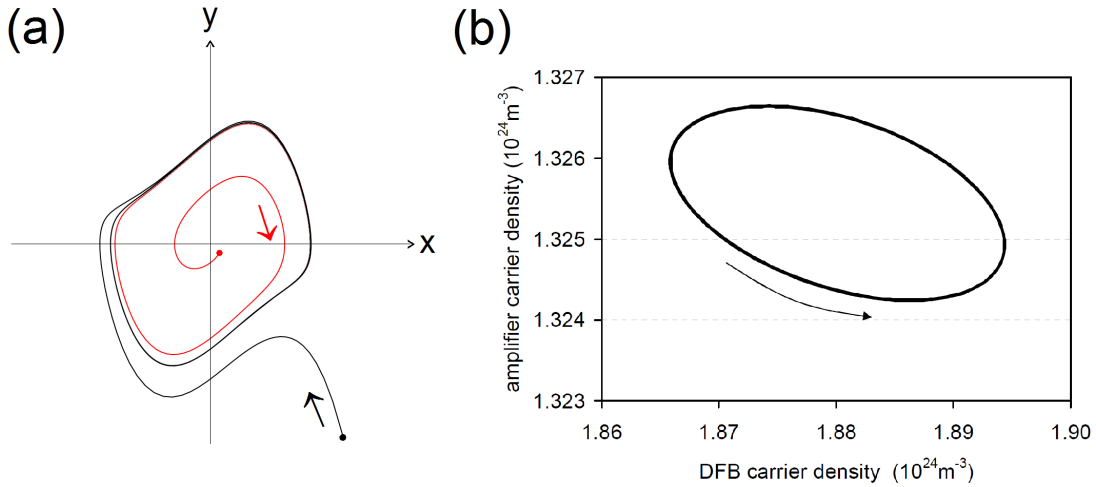

Figure 4.8: Examples for classical limit cycles. (a) Limit cycle of a van der Pol oscillator. Trajectories belonging to two different initial conditions are plotted as red (gray) and black lines. (b) The results of device-realistic simulations of a mode-beating intensity pulsation, using LDSL-tool [32]. The trajectory of the limit cycle in phase space has been projected on the plane of the carrier densities in DFB laser and amplifier section. Figure taken from Ref. [101].

Even though it is not of relevance for unidirectional coupling, the external periodic forcing may of course be generated by a second autonomous oscillator, as is the case in our experiments. In this sense, synchronization to an external forcing can be interpreted as a limiting case of the more general mutual synchronization with bidirectional coupling. Changing from unidirectional to mutual coupling, the self-sustained nature of the former external drive becomes relevant, because synchronization requires autonomous oscillatory processes. These two now *mutually* adjust their frequencies when they are near a rational frequency ratio. Additionally, the coupling delay becomes relevant. It may lead to e.g. amplitude death or multistable synchronization [113, 26]. However, the synchronization scenario described earlier generally remains valid. Fig. 4.9 (b) shows the frequency locking cones of two mutually coupled van der Pol oscillators as determined by simulations. Besides 1:1, the 1:2 and 1:3 resonances as are the strongest. If the coupling strength is too high, the amplitude of one of both oscillations goes to zero for this example system.

In the experiments presented earlier, two mutually coupled oscillatory processes are present in the slave laser. Both intensity pulsations are the result of distinct physical processes. Mathematically, this is reflected in the fact that their trajectory in phase space lies on a two-dimensional torus, similar as sketched in Fig. 4.10 (a,d). The trajectory of a resonant quasiperiodic oscillation on a torus looks similar to a classical limit cycle. Choosing again the carrier densities in amplifier and laser section as parameters, Fig. 4.10 (c) shows a simulated trajectory for a 1:5 locked RO-MB oscillation. Both this trajectory and the one presented in Fig. 4.8 (b) form a closed curve. Self-intersections can be

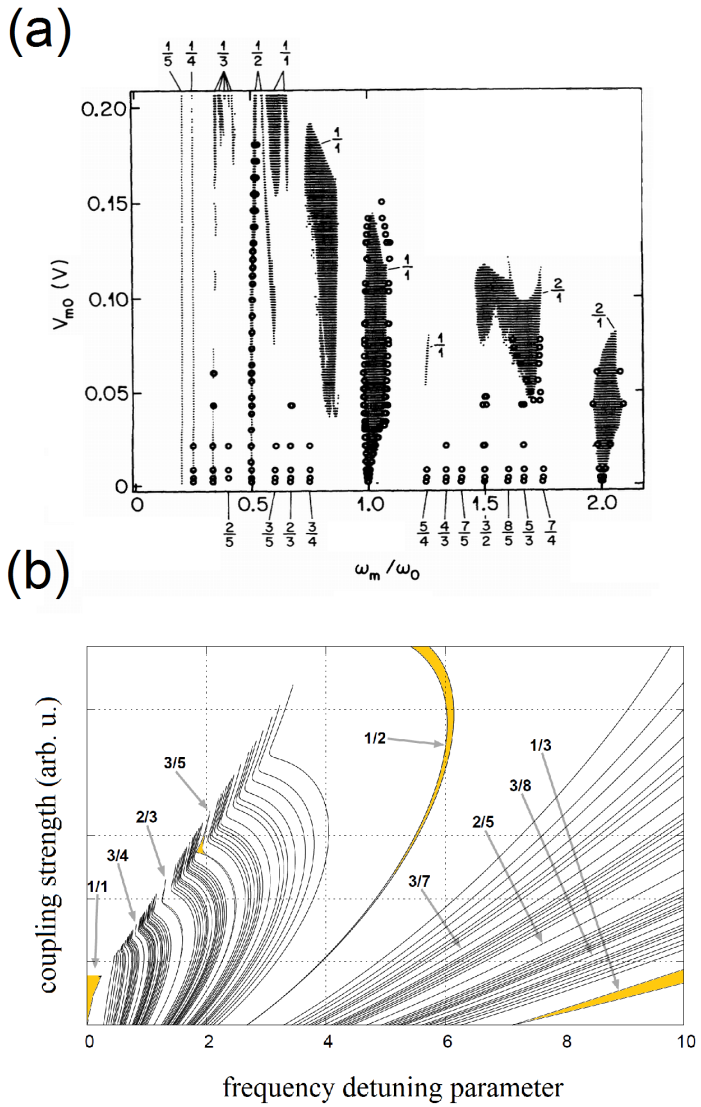

Figure 4.9: Synchronization of nonlinear oscillators at rational frequency ratios in experiment and theory. Each locking cone corresponds to phase locked solutions. (a) Unidirectional coupling, experiment: locking cones of a nuclear magnetic resonance laser with delayed feedback to an external periodic forcing. V_{m0}, modulation amplitude. ω_m, modulation frequency. Circles correspond to measured values, the shading to simulation results. Higher order cones are too narrow to be experimentally resolved and appear as lines. Figure taken from Ref. [112]. (b) Mutual coupling, theory: Locking cones calculated for a system of two linearly coupled van der Pol oscillators. Figure taken from Ref. [111].

removed and introduced by changing the two-dimensional surface in parameter space. The trajectory of a nonresonant limit cycle densely covers the torus surface in Figs. 4.10 (d,e). Similarly, the trajectory in Fig. 4.10 (f) now densely covers parts of the plane.

When adding an external f_{ext} in the experiment, one might predict correctly that f_{ext} will not lock RO when it is not resonant. However, due to the internal RO-MB coupling, f_{RO} does change in frequency, and furthermore a significant increase of coherence can be observed, when f_{MB} synchronizes to f_{MB}. If f_{RO} and f_{MB} are resonant, the analogy to synchronization of a classical limit cycle breaks down. Applying it would lead to the wrong assumption that both f_{MB} and f_{RO} should synchronize to f_{ext} at the same time, and do so regardless of the relation between internal and external coupling strength. As has been demonstrated in the experimental part, this is not the case. There is a coupling and frequency detuning between f_{RO} and f_{MB}, as well as between the two coupled pulsations and f_{ext}, which all have to be taken into account.

After initial investigations in Ref. [115], the bifurcation scenario for synchronization of a resonant quasiperiodic oscillation has been explored by Anishchenko *et al.* with a generic oscillator model [98]. Two self-sustained van der Pol oscillators, with a mismatch between their frequencies f_1 and f_2 and a symmetrical coupling, are used to generate a quasiperiodic oscillation. First, the mutual locking of both oscillators is characterized. Then, a periodic perturbation is added to the equations of motion of one of the oscillators. The complete model shows all essential features of our experimental setup. It has the advantage that the internal coupling strength of the quasiperiodic oscillation can be changed directly. In our experiment, a change in internal coupling strength can be achieved only indirectly by changing the winding number θ. No additional noise is introduced to the model; the coherence of the oscillations is not characterized in the numerical experiments.

Fig. 4.11 presents the numerical results for synchronization of a resonant 1:3 torus, formed by f_1 and f_2, to the external perturbation with frequency f_e. f_1 is the analogue for f_{RO} in our experiment, f_2 the one for f_{MB}. The internal coupling strength can be changed without changing θ, so that both weak and strong internal coupling can be studied at the same 1:3 resonance. The external coupling strength is kept constant for weak and strong internal coupling, as in our experiments. Similar to our experimental part, the frequencies f_1 and f_2 are rescaled with respect to f_e. Fig. 4.11 (a-c) detail synchronization of f_2 to f_e for weak coupling between f_1 and f_2, (d-f) for strong coupling. Fig. 4.11 (c) and (f) show the variation of the winding number $\theta = f_2/f_1$ when changing f_e. Four different regimes are separated by dashed borders and marked by the letters A, B, C and D. In region A, f_e is detuned sufficiently from f_2, so that f_1 and f_2 are mutually synchronized and $\theta = 3$. Changing f_e towards f_2, the internal resonance is broken when entering region B. In B, all three frequencies coexist independently. Further changing f_e, f_2 now locks to f_e upon entering region C, so that $f_2/f_e = 1$. f_e and f_2 form a quasiperiodic oscillation, while f_1 is not synchronized. Only for strong internal coupling in (d-e), region D is observed within region C. In D, all three frequencies are synchronized. Further tuning f_e starting in C, B and A are encountered again.

Two main effects are shown in Fig. 4.11. First, the internal resonance breaks up before any of the frequencies synchronize to f_e, regardless of internal coupling strength. In our

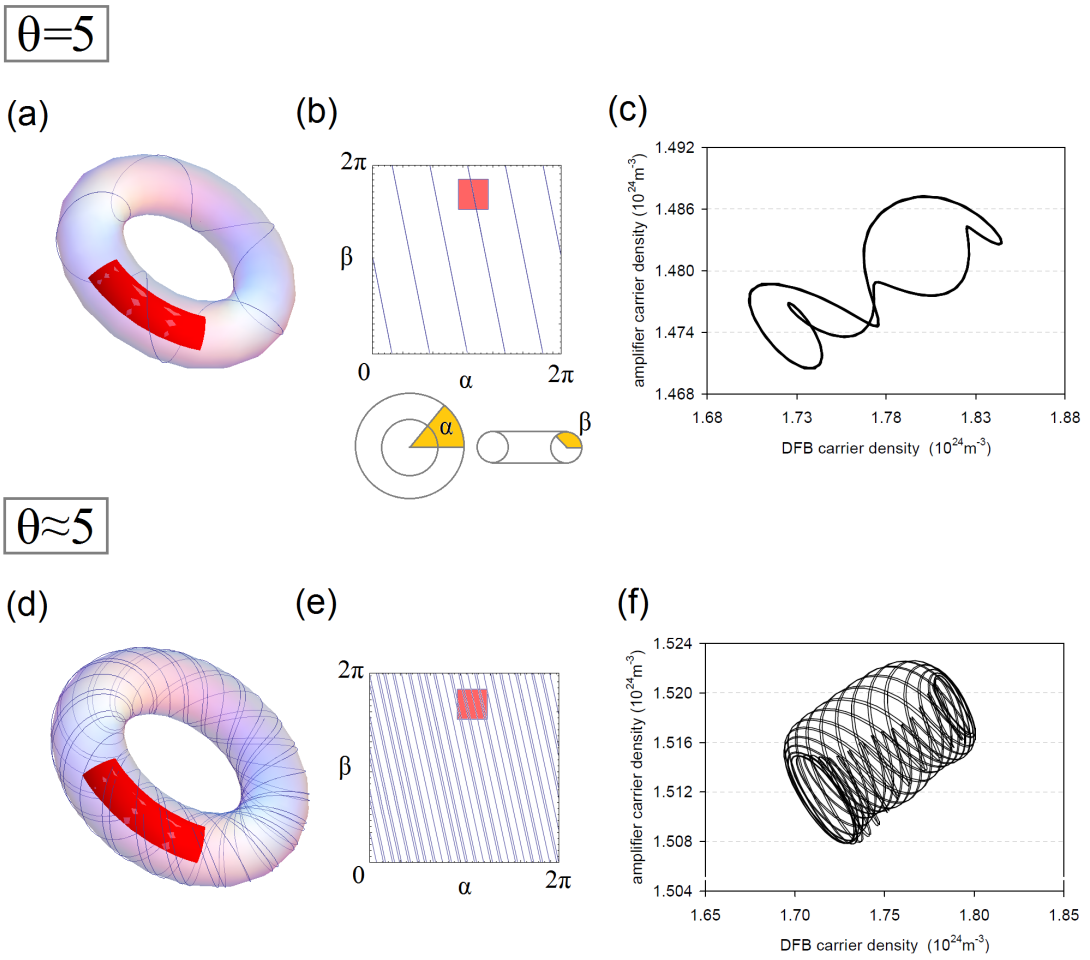

Figure 4.10: The limit cycle of a two-frequency quasiperiodic oscillation near $f_1/f_2 = \theta = 5$. (a-c): $\theta = 5$, resonant case. (d-f): $\theta \approx 5$, nonresonant case. (a): The closed trajectory of a resonant limit cycle on a torus. (b): representation of the two-dimensional torus as a rectangle with periodic boundary conditions. The red area on the torus surface in (a) is equal to the shaded square region. (d,e): non-resonant limit cycle. When θ is irrational, the trajectory is dense on the whole torus surface. (a,b,d) and (e) are drawn using Mathematica and [114]. (c,f): The results of device-realistic simulations of a quasiperiodic intensity pulsation, taken from Ref. [101]. Trajectories in phase space have been projected on the plane of the carrier densities in DFB laser and amplifier section.

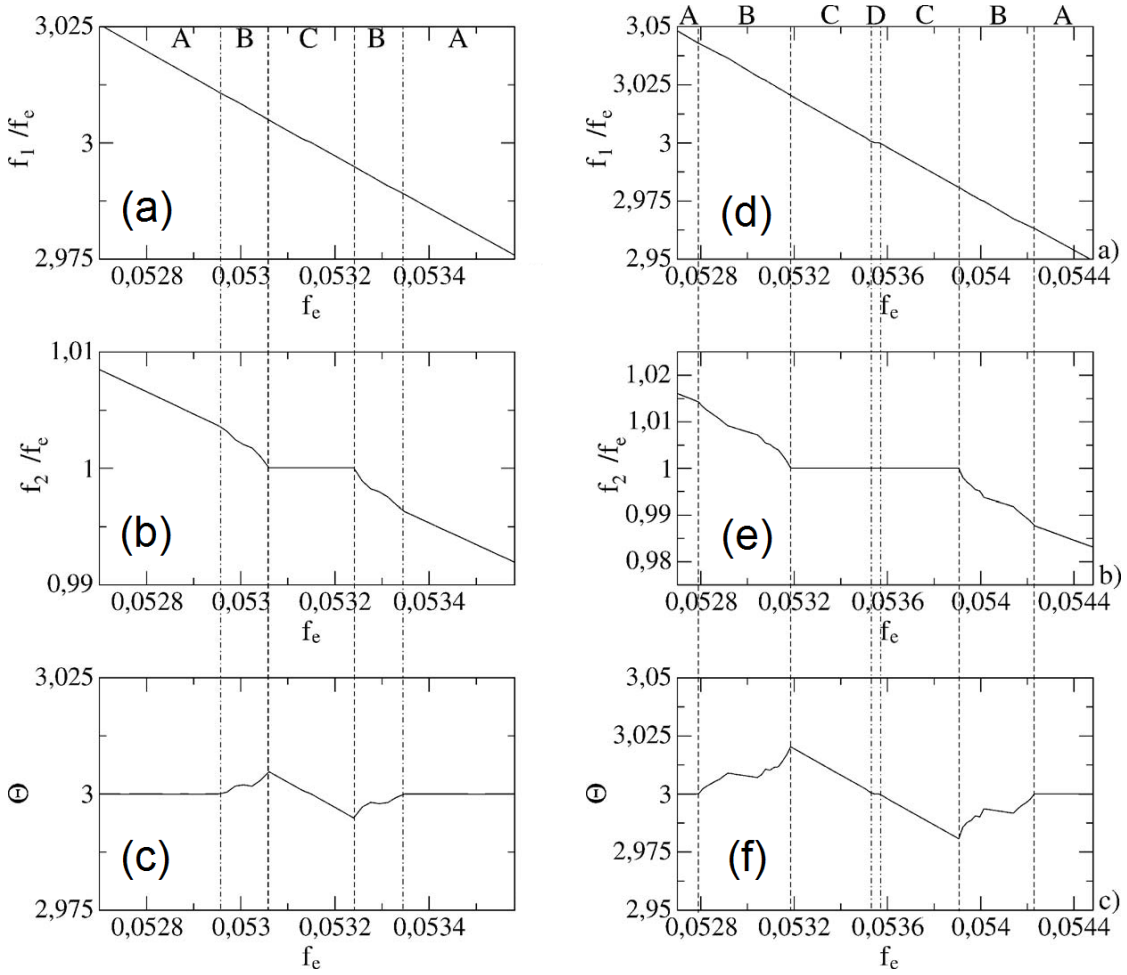

Figure 4.11: Numerical study of synchronization of a resonant quasiperiodic oscillation to a periodic perturbation f_e. The model uses coupled van der Pol oscillators and is described in detail in Ref. [98]. An 1:3 resonance is formed by the two fundamental frequencies f_1 and f_2. (a)-(c): For weak internal coupling between f_1 and f_2, only f_2 can be locked by f_e. (e)-(f): For strong internal coupling, synchronization of both f_1 and f_2 to f_e is possible. Regions marked A, the resonant torus formed by f_1 and f_2 coexists with f_e. Regions marked B, all three frequencies coexist independently. Regions marked C, f_{ext} locked to f_2, f_1 remains non-synchronized. Regions marked D, full synchronization of all three frequencies. Figures taken from Ref. [98].

experiment, no region with three independent frequencies, equivalent to region B in Fig. 4.11, could be observed. It is possible that this region is too small to be resolved. In our experimental data one can indeed observe for $\theta = 3$ that the internal resonance first breaks up, and remains broken in a short interval, before all three frequencies are synchronized. At the same time the internal resonance is broken, f_{MB} synchronizes to f_{ext}. The inset of Fig. 4.6 (h) therefore shows the experimental equivalent to regions marked C in Fig. 4.11. f_{MB} is already locked to f_{ext}, while f_{RO} is not. This small region exists on both sides of the gray shaded area of Fig. 4.6 (h), like region C can be found on both sides of D in Fig. 4.11 (d-f). For weak internal coupling at $\theta = 5$, the locking range shaded gray in Fig. 4.6(h) is the equivalent to region C in Fig. 4.11 (a-c). The breakup of the internal resonance again coincides with the locking of f_{MB} to f_{ext}.

The second effect shown in Fig. 4.11 is that the magnitude of the internal coupling strength determines, whether both f_1 and f_2, or only f_2 can be synchronized by f_e. This was confirmed in our experiment. Given a sufficiently strong internal coupling, both f_{RO} and f_{MB} are entrained by f_{ext}. First the frequency near f_{ext} is locked, then the remaining frequency. For weak internal coupling, f_{RO} cannot be synchronized and the internal resonance remains broken. A marked increase of coherence is seen for f_{RO} in Fig. 4.7(g), as it is resonant to the mutually synchronized f_{MB} and f_{ext} at some point. Even for weak internal coupling, there is also at least one point within region C of Fig. 4.11 (a-c), where all three frequencies are resonant. All together, the qualitative behavior for our complex system is in agreement with the predictions of the model used by Anishchenko *et al.*.

4.4 Summary

In conclusion, quasiperiodic self-pulsations of a semiconductor laser have been synchronized to optically injected periodic pulses emitted by another laser. New regimes due to the interplay between internal and external synchronization processes have been found. Concerning frequency locking, they are in agreement with recent theoretical predictions by Anishchenko *et al.* [98], despite the significant increase of system complexity. This is a strong indication for universality of these phenomena. In particular, they confirm that the route to synchrony of a resonant limit cycle on a torus differs from that of a classical limit cycle. As a consequence, the presence of a resonant torus can be verified by synchronization and distinguished from a nonlinear oscillation with higher harmonics. Completely new and surprising effects have been observed when studying the coherence properties of the oscillations. In particular, external coherence is transferred to both internal oscillations, even if they have very different frequencies and are not synchronous to each other. This feature opens up a novel way to increase the quality of not directly accessible oscillatory subsystems. All together, these results might be highly relevant for multi-scale systems in chemistry, biology and microfluidic technology, as e.g. [116].

5 Outlook

Within the framework of this thesis I investigated two nonlinear phenomena. In the third chapter I described multistability of the emission of a semiconductor laser, which is the result of coherent optical feedback. Synchronization properties of complex oscillatory processes of the light intensity were detailed the fourth chapter.

For the investigated type of optical multistability, I demonstrated that the Lang-Kobayashi model can be used to fully understand the physical mechanisms responsible. The L-K model implies that the degree of multistability can be raised by material and device design. Four or five coexisting states might be achievable by changing α. The advantages of integrated all-optical feedback are that the maximum switching speed is not theoretically limited by electro-optical conversion, and that the device is very robust towards external perturbations. Possible switching between the multiple cw states by an injected short optical pulse has not been investigated yet. It would allow for the use of the experimental device as an all-optical wavelength switch. As the device has originally been developed for telecommunication applications, it is easily integrated into existing optical networks.

In the context of the synchronization experiments a very complex scenario has been revealed. Even for the simple case of a two-frequency intensity pulsation coupled to an external periodic signal, synchronization sensitively depends on the frequencies of, and the coupling between the oscillatory processes. This opens up interesting questions: For our experimental devices, a variety of transitions to chaos in the intensity variation of the laser output is known. Period doubling of mode-beating pulsations is one of the characteristic ways chaos develops, torus breakup of quasiperiodic pulsations another. In the first case, can the period-doubled mode beating pulsations be stabilized against the transition to chaos by synchronizing to them? In the second case, may one synchronize to the remnants of RO or MB which are still visible in the chaotic power spectrum? Does the chaos vanish in this case; are there differences between the synchronization properties of RO and MB? Furthermore, intriguing processes of coherence transfer have been observed. It would be interesting to extend the van der Pol oscillator models used in Ref. [98] to include noise and to compare the simulation results to our experiment.

In general, active feedback lasers are very versatile experimental devices. A huge variety of bifurcations can be accessed in a very controlled way. This allows to realize quite involved experiments like constructing a generator to investigate uniformly hyperbolic chaotic attractors [117]. In hyperbolic attractors all orbits are of saddle type. The dynamics on such attractors have strong chaotic properties, while they are very robust against parameter variations. They additionally allow for a precise mathematical analysis - an experimental validation of the mathematical theory of chaos can be attempted. This is in contrast to all experimental realizations of chaos known so far. There, high-

order periodic windows are always present within the parameter region where chaos occurs, although they may be masked by intrinsic noise. Initial measurements at a setup similar to the one described in Ref. [118] show that such a generator indeed might be feasible using an active feedback laser.

Publications and Conference Contributions related to This Thesis

Publications

- A. Loose, H.-J. Wünsche, and F. Henneberger
  "Synchronization of quasiperiodic oscillations to a periodic force studied with semiconductor lasers"
  Phys. Rev. E 82, 035201(R) (2010)

- A. Loose, B. K. Goswami, H.-J. Wünsche, and F. Henneberger
  "Tristability of a semiconductor laser due to time-delayed optical feedback"
  Phys. Rev. E 79, 134509 (2009)

Conference Contributions

- A. Loose, H.-J. Wünsche, and F. Henneberger
  "Synchronization of quasiperiodic oscillations to an harmonic force studied on semiconductor lasers"
  Talk, SPIE Photonics Europe 2010, April 12th-16th 2010, Brussels, Belgium

- A. Loose, B. K. Goswami, H.-J. Wünsche, and F. Henneberger
  "Multistability of semiconductor lasers with integrated delayed optical feedback"
  Talk, PHYSCON 2009, September 1st-4th 2009, Catania, Italy, invited

- A. Loose, S. Schikora, H.-J. Wünsche, and F. Henneberger
  "Synchronization between semiconductor lasers with internal delayed feedback"
  Talk, PHYSCON 2009, September 1st-4th 2009, Catania, Italy, invited

- A. Loose, H.-J. Wünsche, and F. Henneberger
  "Synchronization of quasiperiodic oscillations in semiconductor lasers"
  Talk, CLEO/Europe-EQEC 2009, June 14th-19th 2009, Munich, Germany

- A. Loose, B. K. Goswami, H.-J. Wünsche, and F. Henneberger
  "Multistability of a semiconductor laser with integrated delayed optical feedback"
  Talk, CLEO/Europe-EQEC 2009, June 14th-19th 2009, Munich, Germany

- A. Loose, H.-J. Wünsche, and F. Henneberger
  "Multisection semiconductor lasers: A lab for complex nonlinear photon dynamics and transport"

Talk, Workshop "Dynamical and Transport Phenomena in Complex Networks" February 16th-18th 2009, São José dos Campos, Brazil

- A. Loose, H.-J. Wünsche, and F. Henneberger
  "Synchronization of a Two-frequency Oscillation in a Semiconductor Laser"
  Poster, WIAS Workshop "Complex Dynamics in Large Coupled Systems", November 17th-19th 2008, Berlin, Germany

- A. Loose, H.-J. Wünsche, and F. Henneberger
  "Synchronization of Resonant Tori in Multisection Semiconductor Lasers"
  Talk, Dynamics Days Berlin-Brandenburg 2008, October 8th-10th 2008, Potsdam, Germany

- A. Loose, B. K. Goswami, H.-J. Wünsche, and F. Henneberger
  "Multistability of a Semiconductor Laser with Integrated Delayed Optical Feedback"
  Talk, Dynamics Days Europe 2008, August 25th-29th 2008, Delft, Netherlands

Acknowledgments

This work would not have been possible without the contributions of many persons. I would like to thank in particular: Prof. Fritz Henneberger for the opportunity to work in his group and his support for new experimental ideas; my direct supervisor Ede Wünsche for his kind guidance, vast knowledge and helpful discussions; Beatrix Matthes for managing all administrative things; Ingo Dudeck for building many of the devices used in experiments and technical support; Dagmar Fahnauer for building mechanical parts and bits; and the other group members, especially Sylvia Schikora, Oleg Ushakov, Simon Halm, Sascha Kalusniak, Jungtaek Kim, Joachim Puls and Sylke Blumstengel for creating a nice atmosphere and all the discussions at the coffee-table. Furthermore, I would like to thank Bernd Sartorius for providing the multisection lasers used in this work and Binoy Goswami for the idea to investigate multistability. The laser seminar at the WIAS and the subsequent discussions in the Spitteleck with Uwe Bandelow, Serhiy Yanchuk, Lutz Recke, Mindaugas Radziunas, Mark Lichtner and Olaf Brox have been a pleasure. I always looked forward to meeting and discussing with Val Moliere and Ingo Fischer when going to conferences. This work was financially supported by the German Research Foundation within the framework of Sonderforschungsbereich 555, which I thankfully acknowledge. Last but foremost, I would like to thank my family and my friends for their continuous love, support and patience.

Bibliography

[1] James T. Fulton. *Biological Vision: A 21st Century Tutorial*. Trafford, 2004. ISBN 978-1412019170.

[2] A. T. Winfree. Biological rhythms and the behavior of populations of coupled oscillators. *J. Theor. Biol.*, 16(1):15–42, 1967.

[3] Arkady Pikovsky, Michael Rosenblum, and Jürgen Kurths. *Synchronization : A Universal Concept in Nonlinear Sciences*. Cambridge University Press, April 2003.

[4] OV Ushakov, HJ Wunsche, F Henneberger, IA Khovanov, L Schimansky-Geier, and MA Zaks. Coherence resonance near a hopf bifurcation. *Phys. Rev. Lett.*, 95 (12), SEP 16 2005. doi: 10.1103/PhysRevLett.95.123903. URL `http://dx.doi.org/10.1103/PhysRevLett.95.123903`.

[5] NOAA National Weather Service. Mariners Weather Log, Aug 1993. URL `http://www.photolib.noaa.gov/bigs/wea00800.jpg`.

[6] Gerhard Ertl. Reactions at surfaces: From atoms to complexity (nobel lecture). *Angewandte Chemie International Edition*, 47(19):3524–3535, Mar 2008. doi: 10.1002/anie.200800480. URL `http://dx.doi.org/10.1002/anie.200800480`.

[7] van der Pol B. A theory of the amplitude of free and forced triode vibrations. *Radio Review*, 1:701–710, 1920.

[8] B. van der Pol and J. van der Mark. Frequency demultiplication. *Nature*, 120: 363–364, 1927.

[9] H. J. Wünsche, O. Brox, M. Radziunas, and F. Henneberger. Excitability of a semiconductor laser by a two-mode homoclinic bifurcation. *Phys. Rev. Lett.*, 88 (2):023901, Dec 2001. doi: 10.1103/PhysRevLett.88.023901. URL `http://dx.doi.org/10.1103/PhysRevLett.88.023901`.

[10] H. J. Wünsche, O. Brox, M. Radziunas, and F. Henneberger. Excitability of a semiconductor laser by a two-mode homoclinic bifurcation. *Phys. Rev. Lett.*, 88 (2):023901, Dec 2001. doi: 10.1103/PhysRevLett.88.023901. URL `http://dx.doi.org/10.1103/PhysRevLett.88.023901`.

[11] O. V. Ushakov, N. Korneyev, M. Radziunas, H. J. Wünsche, and F. Henneberger. Excitability of chaotic transients in a semiconductor laser. *EPL (Europhysics Letters)*, 79(3):30004, 2007. URL `http://stacks.iop.org/0295-5075/79/i=3/a=30004`.

[12] Edward N. Lorenz. Deterministic nonperiodic flow. *Journal of the Atmospheric Sciences*, 20(2):130–141, 1963. doi: 10.1175/1520-0469(1963)020<0130:DNF>2.0.CO;2. URL http://dx.doi.org/10.1175/1520-0469(1963)020<0130:DNF>2.0.CO;2.

[13] John C. Sommerer and Edward Ott. A physical system with qualitatively uncertain dynamics. *Nature*, 365(6442):138–140, 1993. doi: 10.1038/365138a0. URL http://dx.doi.org/10.1038/365138a0.

[14] Mitchell J. Feigenbaum. Quantitative universality for a class of nonlinear transformations. *Journal of Statistical Physics*, 19(1):25–52, Jul 1978. doi: 10.1007/BF01020332. URL http://dx.doi.org/10.1007/BF01020332.

[15] P. W. Anderson. More is different. *Science*, 177(4047):393–396, Aug 1972. doi: 10.1126/science.177.4047.393. URL http://dx.doi.org/10.1126/science.177.4047.393.

[16] Yoshiki Kuramoto. *Chemical Oscillations, Waves, and Turbulence*. Courier Dover Publications, 2003.

[17] Istvan Z. Kiss, Yumei Zhai, and John L. Hudson. Emerging Coherence in a Population of Chemical Oscillators. *Science*, 296(5573):1676–1678, 2002. doi: 10.1126/science.1070757. URL http://www.sciencemag.org/cgi/content/abstract/296/5573/1676.

[18] O. Ushakov, S. Bauer, O. Brox, H.-J. Wünsche, and F. Henneberger. Self-organization in semiconductor lasers with ultrashort optical feedback. *Phys. Rev. Lett.*, 92(4):043902, Jan 2004. doi: 10.1103/PhysRevLett.92.043902. URL http://dx.doi.org/10.1103/PhysRevLett.92.043902.

[19] Pawel Romanczuk, Iain D. Couzin, and Lutz Schimansky-Geier. Collective motion due to individual escape and pursuit response. *Phys. Rev. Lett.*, 102(1):010602, Jan 2009. doi: 10.1103/PhysRevLett.102.010602. URL http://dx.doi.org/10.1103/PhysRevLett.102.010602.

[20] C. Punckt, M. Bolscher, H. H. Rotermund, A. S. Mikhailov, L. Organ, N. Budiansky, J. R. Scully, and J. L. Hudson. Sudden Onset of Pitting Corrosion on Stainless Steel as a Critical Phenomenon. *Science*, 305(5687):1133–1136, 2004. doi: 10.1126/science.1101358. URL http://www.sciencemag.org/cgi/content/abstract/305/5687/1133.

[21] Minseok Kim, Matthias Bertram, Michael Pollmann, Alexander von Oertzen, Alexander S. Mikhailov, Harm Hinrich Rotermund, and Gerhard Ertl. Controlling Chemical Turbulence by Global Delayed Feedback: Pattern Formation in Catalytic CO Oxidation on Pt(110). *Science*, 292(5520):1357–1360, 2001. doi: 10.1126/science.1059478. URL http://www.sciencemag.org/cgi/content/abstract/292/5520/1357.

[22] Anatol M. Zhabotinsky. A history of chemical oscillations and waves. *Chaos: An Interdisciplinary Journal of Nonlinear Science*, 1(4):379–386, 1991. doi: 10.1063/1.165848. URL `http://link.aip.org/link/?CHA/1/379/1`.

[23] A. J. Koch and H. Meinhardt. Biological pattern formation: from basic mechanisms to complex structures. *Rev. Mod. Phys.*, 66(4):1481–1507, Oct 1994. doi: 10.1103/RevModPhys.66.1481. URL `http://dx.doi.org/10.1103/RevModPhys.66.1481`.

[24] Philip Hartman. A lemma in the theory of structural stability of differential equations. *Proc. Amer. Math. Soc*, 11:610–620, 1960. doi: 10.1090/S0002-9939-1960-0121542-7. URL `http://dx.doi.org/10.1016/10.1090/S0002-9939-1960-0121542-7`.

[25] S. Bauer, O. Brox, J. Kreissl, B. Sartorius, M. Radziunas, J. Sieber, H.-J. Wünsche, and F. Henneberger. Nonlinear dynamics of semiconductor lasers with active optical feedback. *Phys. Rev. E*, 69(1):016206, Jan 2004. doi: 10.1103/PhysRevE.69.016206. URL `http://dx.doi.org/10.1103/PhysRevE.69.016206`.

[26] H.-J. Wunsche, S. Bauer, J. Kreissl, O. Ushakov, N. Korneyev, F. Henneberger, E. Wille, H. Erzgraber, M. Peil, W. Elsasser, and I. Fischer. Synchronization of delay-coupled oscillators: A study of semiconductor lasers. *Physical Review Letters*, 94(16):163901, 2005. doi: 10.1103/PhysRevLett.94.163901. URL `http://dx.doi.org/10.1103/PhysRevLett.94.163901`.

[27] S. Schikora, P. Hövel, H.-J. Wünsche, E. Schöll, and F. Henneberger. All-optical noninvasive control of unstable steady states in a semiconductor laser. *Phys. Rev. Lett.*, 97(21):213902, Nov 2006. doi: 10.1103/PhysRevLett.97.213902. URL `http://dx.doi.org/10.1103/PhysRevLett.97.213902`.

[28] Istvan Z. Kiss, Yumei Zhai, and John L. Hudson. Neural Excitability, Spiking, and Bursting. *International Journal of Bifurcation and Chaos*, 10(6):1171–1266, 2000. doi: 10.1142/S0218127400000840. URL `http://dx.doi.org/10.1142/S0218127400000840`.

[29] A.A. Tager and K. Petermann. High-frequency oscillations and self-mode locking in short external-cavity laser diodes. *IEEE J. Quantum Electron.*, 30(7):1553–1561, 1994. ISSN 0018-9197. doi: 10.1109/3.299487. URL `http://dx.doi.org/10.1109/3.299487`.

[30] S Bauer, O Brox, J Kreissl, G Sahin, and B Sartorius. Optical microwave source. *Electron. Lett.*, 38(7):334–335, MAR 28 2002. doi: 10.1049/el:20020228.

[31] A. Argyris, M. Hamacher, K. E. Chlouverakis, A. Bogris, and D. Syvridis. Photonic integrated device for chaos applications in communications. *Physical Review Letters*, 100(19):194101, 2008. doi: 10.1103/PhysRevLett.100.194101. URL `http://dx.doi.org/10.1103/PhysRevLett.100.194101`.

[32] Mindaugas Radziunas, Hans-Jurgen Wunsche, Bernd Krauskopf, and Matthias Wolfrum. External cavity modes in lang-kobayashi and traveling wave models. In Daan Lenstra, Markus Pessa, and Ian H. White, editors, *Proc. SPIE*, volume 6184, page 61840X. SPIE, 2006. doi: 10.1117/12.663546. URL `http://link.aip.org/link/?PSI/6184/61840X/1`.

[33] Jan Sieber. Numerical bifurcation analysis for multisection semiconductor lasers. *SIAM Journal on Applied Dynamical Systems*, 1(2):248–270, 2002. doi: 10.1137/S1111111102401746. URL `http://dx.doi.org/10.1137/S1111111102401746`.

[34] Stefan Bauer. *Nonlinear dynamics of semiconductor lasers with active optical feedback*. PhD thesis, Humboldt-Universität zu Berlin, 2004.

[35] John E. l Carrol, James Whiteaway, and R. G. S. Plumb. *Distributed Feedback Semiconductor Lasers*. Institution of Engineering and Technology, 1998. ISBN 978-0852969175.

[36] R. N. Hall, G. E. Fenner, J. D. Kingsley, T. J. Soltys, and R. O. Carlson. Coherent light emission from gaas junctions. *Phys. Rev. Lett.*, 9(9):366–368, Nov 1962. doi: 10.1103/PhysRevLett.9.366. URL `http://dx.doi.org/10.1103/PhysRevLett.9.366`.

[37] Marshall I. Nathan, William P. Dumke, Gerald Burns, Jr. Frederick H. Dill, and Gordon Lasher. Stimulated emission of radiation from gaas p-n junctions. *Applied Physics Letters*, 1(3):62–64, 1962. doi: 10.1063/1.1777371. URL `http://link.aip.org/link/?APL/1/62/1`.

[38] Jr. Nick Holonyak and S. F. Bevacqua. Coherent (visible) light emission from ga(as[sub 1 - x]p[sub x]) junctions. *Applied Physics Letters*, 1(4):82–83, 1962. doi: 10.1063/1.1753706. URL `http://link.aip.org/link/?APL/1/82/1`.

[39] T. M. Quist, R. H. Rediker, R. J. Keyes, W. E. Krag, B. Lax, A. L. McWhorter, and H. J. Zeigler. Semiconductor maser of gaas. *Applied Physics Letters*, 1(4):91–92, 1962. doi: 10.1063/1.1753710. URL `http://link.aip.org/link/?APL/1/91/1`.

[40] S. E. Harris. Lasers without inversion: Interference of lifetime-broadened resonances. *Phys. Rev. Lett.*, 62(9):1033–1036, Feb 1989. doi: 10.1103/PhysRevLett.62.1033. URL `http://dx.doi.org/10.1103/PhysRevLett.62.1033`.

[41] Gordon Gould. Some rough calculations on the feasibility of a laser, 1957.

[42] A. L. Schawlow and C. H. Townes. Infrared and optical masers. *Phys. Rev.*, 112 (6):1940–1949, Dec 1958. doi: 10.1103/PhysRev.112.1940. URL `http://dx.doi.org/10.1103/PhysRev.112.1940`.

[43] Theodore H. Maiman. Stimulated Optical Radiation in Ruby. *Nature*, 187(4736): 493–494, 1960. doi: 10.1038/187493a0. URL `http://dx.doi.org/10.1038/187493a0`.

[44] H. Kogelnik and C. V. Shank. Stimulated emission in a periodic structure. *Applied Physics Letters*, 18(4):152–154, 1971. doi: 10.1063/1.1653605. URL `http://link.aip.org/link/?APL/18/152/1`.

[45] H. Kogelnik and C. V. Shank. Coupled-wave theory of distributed feedback lasers. *Journal of Applied Physics*, 43(5):2327–2335, 1972. doi: 10.1063/1.1661499. URL `http://link.aip.org/link/?JAP/43/2327/1`.

[46] James Moran. Astronomy: Masers in the nuclei of galaxies. *Nature*, 310(5975):270–271, 1984. doi: 10.1038/310270a0. URL `http://dx.doi.org/10.1038/310270a0`.

[47] H. Cao, Y. G. Zhao, S. T. Ho, E. W. Seelig, Q. H. Wang, and R. P. H. Chang. Random laser action in semiconductor powder. *Phys. Rev. Lett.*, 82(11):2278–2281, Mar 1999. doi: 10.1103/PhysRevLett.82.2278. URL `http://dx.doi.org/10.1103/PhysRevLett.82.2278`.

[48] S. Kalusniak, H. J. Wünsche, and F. Henneberger. Random semiconductor lasers: Scattered versus fabry-perot feedback. *Phys. Rev. Lett.*, 106(1):013901, Jan 2011. doi: 10.1103/PhysRevLett.106.013901. URL `http://dx.doi.org/10.1103/PhysRevLett.106.013901`.

[49] K.C. Kao and G.A. Hockham. Dielectric-fibre surface waveguides for optical frequencies. *Proceedings of the Institution of Electrical Engineers*, 113(7):1151–1158, 1966. doi: 10.1049/piee.1966.0189. URL `http://link.aip.org/link/?PIE/113/1151/1`.

[50] Albert Einstein. Quantentheorie der Strahlung. (German) [Quantum Theory of Radiation]. *Physikalische Zeitschrift*, 18(??):121–128, 1917.

[51] Roy J. Glauber. Nobel lecture: One hundred years of light quanta. *Rev. Mod. Phys.*, 78(4):1267–1278, Nov 2006. doi: 10.1103/RevModPhys.78.1267. URL `http://dx.doi.org/10.1103/RevModPhys.78.1267`.

[52] J. Kim, O. Benson, H. Kan, and Y. Yamamoto. A single-photon turnstile device. *Nature*, 397(6719):500–503, 1999. doi: 10.1038/17295. URL `http://dx.doi.org/10.1038/17295`.

[53] M. Osinski and J. Buus. Linewidth broadening factor in semiconductor lasers - an overview. *Quantum Electronics, IEEE Journal of*, 23(1):9 – 29, Jan 1992. URL `http://ieeexplore.ieee.org/xpls/abs_all.jsp?arnumber=1073204`.

[54] Steven H. Strogatz. *Nonlinear Dynamics and Chaos*. Addison-Wesley, Reading, MA, 1994.

[55] Sebastian Wieczorek, Bernd Krauskopf, and Daan Lenstra. A unifying view of bifurcations in a semiconductor laser subject to optical injection. *Optics Communications*, 172(1-6):279 – 295, 1999. ISSN 0030-4018. doi: DOI:10.1016/S0030-4018(99)00603-3. URL `http://www.sciencedirect.com/science/article/B6TVF-418XNP0-13/2/a7831312f5ae3168bb943f53b16acbaf`.

[56] Guido H. M. van Tartwijk and Govind P Agrawal. Laser instabilities: a modern perspective. *Progress in Quantum Electronics*, 22(2):43 – 122, 1998. ISSN 0079-6727. doi: 10.1016/S0079-6727(98)00008-1. URL `http://dx.doi.org/10.1016/S0079-6727(98)00008-1`.

[57] R. Lang and K. Kobayashi. External optical feedback effects on semiconductor injection laser properties. *IEEE J. Quantum Electron.*, 16(3):347–355, 1980. ISSN 0018-9197.

[58] J. Osmundsen and N. Gade. Influence of optical feedback on laser frequency spectrum and threshold conditions. *Quantum Electronics, IEEE Journal of*, 19 (3):465 – 469, 1960. doi: 10.1109/JQE.1983.1071857. URL `http://dx.doi.org/10.1109/JQE.1983.1071857`.

[59] T. Morikawa, Y. Mitsuhashi, J. Shimada, and Y. Kojima. Return-beam-induced oscillations in self-coupled semiconductor lasers. *Electronics Letters*, 12(17):435 – 436, Aug 1976. doi: 10.1049/el:19760331. URL `http://dx.doi.org/10.1049/el:19760331`.

[60] Ch. Risch and C. Voumard. Self-pulsation in the output intensity and spectrum of gaas-algaas cw diode lasers coupled to a frequency-selective external optical cavity. *Journal of Applied Physics*, 48(5):2083–2085, 1977. doi: 10.1063/1.323922. URL `http://link.aip.org/link/?JAP/48/2083/1`.

[61] D. Lenstra, B. Verbeek, and A. Den Boef. Coherence collapse in single-mode semiconductor lasers due to optical feedback. *Quantum Electronics, IEEE Journal of*, 21(6):674 – 679, Jun 1985.

[62] T. Heil, I. Fischer, W. Elsäßer, B. Krauskopf, K. Green, and A. Gavrielides. Delay dynamics of semiconductor lasers with short external cavities: Bifurcation scenarios and mechanisms. *Phys. Rev. E*, 67(6):066214, Jun 2003. doi: 10.1103/PhysRevE.67.066214. URL `http://dx.doi.org/10.1103/PhysRevE.67.066214`.

[63] H. Erzgräber, D. Lenstra, B. Krauskopf, A. P. A. Fischer, and G. Vemuri. Feedback phase sensitivity of a semiconductor laser subject to filtered optical feedback: Experiment and theory. *Phys. Rev. E*, 76(2):026212, Aug 2007. doi: 10.1103/PhysRevE.76.026212. URL `http://dx.doi.org/10.1103/PhysRevE.76.026212`.

[64] O. Ushakov, S. Bauer, O. Brox, H.-J. Wünsche, and F. Henneberger. Self-organization in semiconductor lasers with ultrashort optical feedback. *Phys. Rev. Lett.*, 92(4):043902, 2004. doi: 10.1103/PhysRevLett.92.043902. URL `http://dx.doi.org/10.1103/PhysRevLett.92.043902`.

[65] A.A. Tager and B.B. Elenkrig. Stability regimes and high-frequency modulation of laser diodes with short external cavity. *IEEE J. Quantum Electron.*, 29(12): 2886–2890, 1993. ISSN 0018-9197. doi: 10.1109/3.259402. URL `http://dx.doi.org/10.1109/3.259402`.

[66] Olaf Brox. *DFB-Laser mit integriert optischer Rückkopplung für die optische Signalverarbeitung*. PhD thesis, Technische Universität Berlin, 2005.

[67] H.-J. Wünsche, S. Bauer, J. Kreissl, O. Ushakov, N. Korneyev, F. Henneberger, E. Wille, H. Erzgräber, M. Peil, W. Elsäßer, and I. Fischer. Synchronization of delay-coupled oscillators: A study of semiconductor lasers. *Phys. Rev. Lett.*, 94 (16):163901, 2005. doi: 10.1103/PhysRevLett.94.163901. URL `http://dx.doi.org/10.1103/PhysRevLett.94.163901`.

[68] Oleg Ushakov. *Self-organization in semiconductor lasers with ultra-short optical feedback*. PhD thesis, Humboldt-Universität zu Berlin, 2007.

[69] H. M. Gibbs. *Optical bistability: Controlling light with light*. Academic Press, 1985.

[70] L. Gelens, S. Beri, G. Van der Sande, G. Mezosi, M. Sorel, J. Danckaert, and G. Verschaffelt. Exploring multistability in semiconductor ring lasers: Theory and experiment. *Phys. Rev. Lett.*, 102(19):193904, May 2009. doi: 10.1103/PhysRevLett.102.193904. URL `http://dx.doi.org/PhysRevLett.102.193904`.

[71] JH Kim, M Yoneya, and H Yokoyama. Tristable nematic liquid-crystal device using micropatterned surface alignment. *Nature*, 420(6912):159–162, NOV 14 2002.

[72] Koen Huybrechts, Bjorn Maes, Geert Morthier, and Roel Baets. Tristable all-optical flip-flop using coupled nonlinear cavities. *Winter Topical Meeting Series, IEEE/LEOS*, pages 16–17, Jan. 2008. doi: 10.1109/LEOSWT.2008.4444377. URL `http://dx.doi.org/10.1109/LEOSWT.2008.4444377`.

[73] A. Loose, B. K. Goswami, H.-J. Wünsche, and F. Henneberger. Tristability of a semiconductor laser due to time-delayed optical feedback. *Phys. Rev. E*, 79(3): 036211, Mar 2009. doi: 10.1103/PhysRevE.79.036211. URL `http://dx.doi.org/10.1103/PhysRevE.79.036211`.

[74] Kirk Green. Stability near threshold in a semiconductor laser subject to optical feedback: A bifurcation analysis of the lang-kobayashi equations. *Phys. Rev. E*, 79 (3):036210, Mar 2009. doi: 10.1103/PhysRevE.79.036210. URL `http://dx.doi.org/10.1103/PhysRevE.79.036210`.

[75] V. Rottschäfer and B. Krauskopf. The ecm-backbone of the lang-kobayashi equations: a geometric picture. *International Journal of Bifurcation and Chaos*, 17(5):1575–1588, 2007. doi: 10.1142/S0218127407017914. URL `http://www.worldscinet.com/ijbc/17/1705/S0218127407017914.html`.

[76] Guang-Qiong Xia, Sze-Chun Chan, and Jia-Ming Liu. Multistability in a semiconductor laser with optoelectronic feedback. *Opt. Express*, 15(2):572–576, 2007.

[77] S. Cecchi, G. Giusfredi, E. Petriella, and P. Salieri. Observation of optical tristability in sodium vapors. *Phys. Rev. Lett.*, 49(26):1928–1931, Dec 1982. doi: 10.

1103/PhysRevLett.49.1928. URL http://dx.doi.org/10.1103/PhysRevLett.49.1928.

[78] VN Chizhevsky. Coexisting attractors in a co2 laser with modulated losses. *J. Opt. B-Quantum Semicl. Opt.*, 2(6):711–717, DEC 2000. ISSN 1464-4266.

[79] A. N. Pisarchik, Yu. O. Barmenkov, and A. V. Kiryanov. Experimental demonstration of attractor annihilation in a multistable fiber laser. *Phys. Rev. E*, 68(6): 066211, Dec 2003. doi: 10.1103/PhysRevE.68.066211. URL http://dx.doi.org/10.1103/PhysRevE.68.066211.

[80] BK Goswami. Multiple attractors in the self-similar bifurcation-structure. *Riv. Nuovo Cimento*, 28(4-5):1–115, 2005. doi: 10.1393/ncr/i2006-10003-7. URL http://dx.doi.org/10.1393/ncr/i2006-10003-7.

[81] Masanobu Watanabe, Hideo Itoh, Seiji Mukai, and Hiroyoshi Yajima. Optical tristability using a twin-stripe laser diode. *Applied Physics Letters*, 50(8):427–429, 1987. doi: 10.1063/1.98163. URL http://dx.doi.org/10.1063/1.98163.

[82] J P Goedgebuer, A Fischer, and H Porte. Controlled wavelength bistability and multistability of tunable semiconductor lasers. *Quantum Electronics*, 26(3):242–244, 1996.

[83] M. Oriá, B. Farias, T. Sorrentino, and M. Chevrollier. Multistability in the emission frequency of a semiconductor laser. *J. Opt. Soc. Am. B*, 24(8):1867–1873, 2007.

[84] M. Ikeda, S. Oku, and M. Ogasawara. Optical tristability in two-section laser diode. *Electron. Lett.*, 25(25):1701–1702, 7 Dec 1989. ISSN 0013-5194.

[85] R. Meucci, A. Poggi, F.T. Arecchi, and J.R. Tredicce. Dissipativity of an optical chaotic system characterized via generalized multistability. *Optics Communications*, 65(2):151 – 156, 1988. ISSN 0030-4018. doi: DOI:10.1016/0030-4018(88)90288-X. URL http://www.sciencedirect.com/science/article/B6TVF-46JGXVM-299/2/150a0f6279cff0224061c7c6ad544f74.

[86] V N Chizhevsky. Coexisting attractors in a co2 laser with modulated losses. *Journal of Optics B: Quantum and Semiclassical Optics*, 2(6):711–717, 2000. URL http://stacks.iop.org/1464-4266/2/711.

[87] O. Brox, S. Bauer, M. Radziunas, M. Wolfrum, J. Sieber, J. Kreissl, B. Sartorius, and H.-J. Wunsche. High-frequency pulsations in dfb lasers with amplified feedback. *IEEE J. Quantum Electron.*, 39(11):1381–1387, 2003. ISSN 0018-9197. doi: 10.1109/JQE.2003.818313. URL http://dx.doi.org/10.1109/JQE.2003.818313.

[88] J Slovak, C Bornholdt, J Kreissl, S Bauer, M Biletzke, M Schlak, and B Sartorius. Bit rate and wavelength transparent all-optical clock recovery scheme for nrz-coded

prbs signals. *IEEE Photonics Technol. Lett.*, 18(5-8):844–846, MAR-APR 2006. doi: 10.1109/LPT.2006.871834. URL http://dx.doi.org/10.1109/LPT.2006.871834.

[89] B. Fiedler, S. Yanchuk, V. Flunkert, P. Hövel, H.-J. Wünsche, and E. Schöll. Delay stabilization of rotating waves near fold bifurcation and application to all-optical control of a semiconductor laser. *Phys. Rev. E*, 77(6):066207, Jun 2008. doi: 10.1103/PhysRevE.77.066207. URL http://dx.doi.org/10.1103/PhysRevE.77.066207.

[90] M. Radziunas. Numerical bifurcation analysis of the traveling wave model of multisection semiconductor lasers. *Physica D: Nonlinear Phenomena*, 213 (1):98 – 112, 2006. ISSN 0167-2789. doi: DOI:10.1016/j.physd.2005.11.003. URL http://www.sciencedirect.com/science/article/B6TVK-4HRMTT4-1/2/05531494572b76c200c8d6d0b631a8c7.

[91] M Wolfrum and D Turaev. High-frequency oscillations and self-mode locking in short external-cavity laser diodes. *Opt. Commun.*, 212(1-3):127–138, 2002. doi: 10.1016/S0030-4018(02)01824-2. URL http://dx.doi.org/10.1016/S0030-4018(02)01824-2.

[92] F. Favre. Theoretical analysis of external optical feedback on dfb semiconductor lasers. *IEEE J. Quantum Electron.*, 23(1):81–88, 1987.

[93] N. Schunk and K. Petermann. Numerical analysis of the feedback regimes for a single-mode semiconductor laser with external feedback. *Quantum Electronics, IEEE Journal of*, 24(7):1242 –1247, Jul 1988. doi: 10.1109/3.960. URL http://dx.doi.org/10.1109/3.960.

[94] Michael G. Rosenblum, Arkady S. Pikovsky, and Jürgen Kurths. Phase synchronization of chaotic oscillators. *Phys. Rev. Lett.*, 76(11):1804–1807, Mar 1996. doi: 10.1103/PhysRevLett.76.1804. URL http://dx.doi.org/10.1103/PhysRevLett.76.1804.

[95] Louis M. Pecora and Thomas L. Carroll. Master stability functions for synchronized coupled systems. *Phys. Rev. Lett.*, 80(10):2109–2112, Mar 1998. doi: 10.1103/PhysRevLett.80.2109. URL http://dx.doi.org/10.1103/PhysRevLett.80.2109.

[96] D. L. Shepelyansky, A. S. Pikovsky, J. Schmidt, and F. Spahn. Synchronization mechanism of sharp edges in rings of saturn. *Monthly Notices of the Royal Astronomical Society*, 395(4):1934–1940, 2009. doi: DOI:10.1111/j.1365-2966.2009.14719.x. URL http://dx.doi.org/10.1111/j.1365-2966.2009.14719.x.

[97] V. Anishchenko, S. Nikolaev, and J. Kurths. Winding number locking on a two-dimensional torus: Synchronization of quasiperiodic motions. *Phys. Rev. E*, 73(5):056202, 2006. doi: 10.1103/PhysRevE.73.056202. URL http://dx.doi.org/10.1103/PhysRevE.73.056202.

[98] V. Anishchenko, S. Nikolaev, and J. Kurths. Bifurcational mechanisms of synchronization of a resonant limit cycle on a two-dimensional torus. *Chaos*, 18(3):037123, 2008. doi: 10.1063/1.2949929. URL http://dx.doi.org/10.1063/1.2949929.

[99] Zh.T. Zhusubaliyev, E.A. Soukhoterin, and E. Mosekilde. Border-collision bifurcations on a two-dimensional torus. *Chaos, Solitons & Fractals*, 13(9):1889 – 1915, 2002. doi: DOI:10.1016/S0960-0779(01)00205-3. URL http://dx.doi.org/10.1016/S0960-0779(01)00205-3.

[100] Carsten Schafer, Michael G. Rosenblum, Jurgen Kurths, and Hans-Henning Abel. Heartbeat synchronized with ventilation. *Nature*, 392(6673):239–240, 3 1998. doi: 10.1038/32567. URL http://dx.doi.org/10.1038/32567.

[101] S. Bauer, O. Brox, J. Kreissl, B. Sartorius, M. Radziunas, J. Sieber, H.-J. Wünsche, and F. Henneberger. Nonlinear dynamics of semiconductor lasers with active optical feedback. *Phys. Rev. E*, 69(1):016206, Jan 2004. doi: 10.1103/PhysRevE.69.016206. URL http://dx.doi.org/10.1103/PhysRevE.69.016206.

[102] O. V. Ushakov, N. Korneyev, M. Radziunas, H. J. Wunsche, and F. Henneberger. Excitability of chaotic transients in a semiconductor laser. *EPL (Europhysics Letters)*, 79(3):30004 (5pp), 2007.

[103] Arkady S. Pikovsky and Jürgen Kurths. Coherence resonance in a noise-driven excitable system. *Phys. Rev. Lett.*, 78(5):775–778, Feb 1997. doi: 10.1103/PhysRevLett.78.775. URL http://dx.doi.org/10.1103/PhysRevLett.78.775.

[104] A. Khintchine. Korrelationstheorie der stationären stochastischen prozesse. *Mathematische Annalen*, 109(1):604–615, Dec 1933. doi: 10.1007/BF01449156. URL http://dx.doi.org/10.1007/BF01449156.

[105] F. Takens. Forced oscillations and bifurcations. *Applications of Global Analysis I, Communications of the Mathematical Institute Rijksuniversiteit Utrecht*, 3, 1974. doi: 10.1.1.26.3310. URL http://citeseerx.ist.psu.edu/viewdoc/summary?doi=10.1.1.26.3310.

[106] Henk W. Broer, Bernd Krauskopf, and Gert Vegter. Global analysis of dynamical systems festschrift dedicated to floris takens for his 60th birthday, 2001. URL http://dx.doi.org/10.1.1.26.3310.

[107] V. I. Arnol'd. Loss of stability of self-oscillations close to resonance and versal deformations of equivariant vector fields. *Functional Analysis and Its Applications*, 11:85–92, 1977. ISSN 0016-2663. URL http://dx.doi.org/10.1007/BF01081886. 10.1007/BF01081886.

[108] Uwe Bandelow, Lutz Recke, and Björn Sandstede. Frequency regions for forced locking of self-pulsating multi-section dfb lasers. *Optics Communications*, 147 (1-3):212 – 218, 1998. doi: DOI:10.1016/S0030-4018(97)00570-1. URL http://dx.doi.org/10.1016/S0030-4018(97)00570-1.

[109] Lutz Recke, Anatoly Samoilenko, Alexey Teplinsky, Viktor Tkachenko, and Serhiy Yanchuk. Frequency locking of modulated waves, 2010. URL `http://www.matheon.de/research/list_preprints.asp`.

[110] A. Vizzino, M. Gioannini, and I. Montrosset. Dynamic simulation of clock recovery with self-pulsating three-section distributed-feedback lasers. *Quantum Electronics, IEEE Journal of*, 38(12):1580–1586, Dec 2002. doi: 10.1109/JQE.2002.805102. URL `http://dx.doi.org/10.1109/JQE.2002.805102`.

[111] Frank Schilder and Bruce B. Peckham. Computing arnol'd tongue scenarios. *Journal of Computational Physics*, 220(2):932 – 951, 2007. ISSN 0021-9991. doi: 10.1016/j.jcp.2006.05.041. URL `http://www.sciencedirect.com/science/article/B6WHY-4KF1J00-5/2/a1141cd3ce4d4a6ec8dfa7601713cf01`.

[112] J. Simonet, M. Warden, and E. Brun. Locking and arnold tongues in an infinite-dimensional system: The nuclear magnetic resonance laser with delayed feedback. *Phys. Rev. E*, 50(5):3383–3391, Nov 1994. doi: 10.1103/PhysRevE.50.3383. URL `http://dx.doi.org/10.1103/PhysRevE.50.3383`.

[113] H. G. Schuster and P. Wagner. Mutual entrainment of two limit cycle oscillators with time delayed coupling. *Progress of Theoretical Physics*, 81(5):939–945, 1989. doi: 10.1143/PTP.81.939. URL `http://192.168.11.3/link?PTP/81/939/`.

[114] Kevin Sonnanburg and Nicholas Willis. Motion traced on the torus and klein bottle. The Wolfram Demonstrations Project, 2010. URL `http://demonstrations.wolfram.com/MotionTracedOnTheTorusAndKleinBottle/`.

[115] V. Anishchenko, S. Nikolaev, and J. Kurths. Peculiarities of synchronization of a resonant limit cycle on a two-dimensional torus. *Phys. Rev. E*, 76(4):046216, 2007. doi: 10.1103/PhysRevE.76.046216. URL `http://dx.doi.org/10.1103/PhysRevE.76.046216`.

[116] H Willaime, V. Barbier, L. Kloul, S. Maine, and P. Tabeling. Arnold tongues in a microfluidic drop emitter. *Physical Review Letters*, 96(5):054501, 2006. doi: 10.1103/PhysRevLett.96.054501. URL `http://dx.doi.org/10.1103/PhysRevLett.96.054501`.

[117] Sergey P. Kuznetsov. Example of a physical system with a hyperbolic attractor of the smale-williams type. *Phys. Rev. Lett.*, 95(14):144101, Sep 2005. doi: 10.1103/PhysRevLett.95.144101. URL `http://dx.doi.org/10.1103/PhysRevLett.95.144101`.

[118] S. P. Kuznetsov and A. Pikovsky. Hyperbolic chaos in the phase dynamics of a q-switched oscillator with delayed nonlinear feedbacks. *EPL (Europhysics Letters)*, 84(1):10013, 2008. URL `http://stacks.iop.org/0295-5075/84/i=1/a=10013`.

List of Figures

List of Tables

Selbständigkeitserklärung

Ich erkläre, dass ich die vorliegende Arbeit selbständig und nur unter Verwendung der angegebenen Literatur und Hilfsmittel angefertigt habe.

Berlin, den 09.03.2011
André Loose